

Alma Mater Studiorum – Università di Bologna

DOTTORATO DI RICERCA IN

GEOFISICA

Ciclo XXVIII

**Settore Concorsuale di afferenza:** 04/A4 - GEOFISICA

**Settore Scientifico disciplinare:** GEO/10

**INSAR ROLE IN THE STUDY OF EARTH'S SURFACE AND SYNERGIC  
USE WITH OTHER GEODETIC DATA: THE 2014 SOUTH NAPA  
EARTHQUAKE**

**Presentata da:** Marco Polcari

**Coordinatore Dottorato**

Prof.ssa Nadia Pardini

**Relatore**

Prof. Salvatore Stramondo

**Co-Relatore**

Prof.ssa Susanna Zerbini

**Esame finale anno 2016**

# ***Index***

<b><i>Abstract</i></b>	<b>1</b>
<b><i>Chapter 1: General Introduction</i></b>	<b>3</b>
<i>1.1 Observing the Earth from the space</i>	3
<i>1.2 InSAR outline</i>	5
<i>1.3 GPS outline</i>	10
<i>1.4 MAI outline</i>	12
<i>1.5 POT outline</i>	13
<i>References</i>	14
<b><i>Chapter 2: InSAR applied to the study of surface deformations due to natural or anthropic phenomena</i></b>	<b>16</b>
<i>2.1 Introduction</i>	16
<i>2.2 Lunigiana earthquake</i>	17
<i>2.2.1 InSAR outcomes</i>	18
<i>2.2.2 Source modeling</i>	20
<i>2.2.3 The breached relay ramp</i>	22
<i>2.3 Campi Flegrei uplift</i>	23
<i>2.3.1 InSAR and GPS data</i>	24
<i>2.3.2 Source inference</i>	26
<i>2.4 Subsidence in the Cassino plain</i>	29
<i>2.4.1 InSAR observations</i>	31
<i>2.4.2 The joint effect of natural and anthropogenic factors</i>	35
<i>References</i>	37

<b><i>Chapter 3: 3D Displacement field retrieved by integrating Sentinel-1 InSAR and GPS data: the 2014 South Napa earthquake</i></b>	<b>42</b>
3.1 Introduction	42
3.2 InSAR-GPS integration: theory	43
3.3 Geodetic data	46
3.3.1 InSAR data	46
3.3.2 GPS data	46
3.4 Results	48
3.5 Discussion and conclusions	51
References	52
<b><i>Chapter 4: An advanced algorithm to constrain the 3D displacement maps based on data integration: the case study of Napa Valley earthquake</i></b>	<b>54</b>
4.1 Overview on the data integration	54
4.2 Dataset	56
4.3 Method	59
4.3.1 Programming side	61
4.4 Errors	62
4.5 GPS data interpolation	65
4.6 Results for the Napa earthquake	67
4.7 Source modeling	68
4.7.1 Single fault modeling	69
4.7.2 Double fault modeling	71
References	74

<b><i>Chapter 5: General discussion and conclusion</i></b>	<b>77</b>
5.1 <i>Data properties</i>	77
5.2 <i>Strengths of the data integration algorithm</i>	78
5.3 <i>Drawbacks of the data integration algorithm</i>	78
5.4 <i>Future perspectives</i>	79
<i>References</i>	80
<b><i>Appendix A: Computer code</i></b>	<b>81</b>
<b><i>Appendix B: Napa coherence map</i></b>	<b>89</b>
<b><i>Copyright releases</i></b>	<b>90</b>
<b><i>Acknowledgments</i></b>	<b>94</b>

*"Quando io vorrei esprimermi a parole,  
appaiono soltanto immagini davanti ai miei occhi:  
il bellissimo paesaggio, il mare libero,  
le isole scintillanti, la montagna ruggente:  
mi manca la capacità di descrivere tutto ciò.  
Napoli è un Paradiso,  
tutti ci vivono in una specie  
di inebriata dimenticanza di sé;  
ed è per me una strana esperienza quella  
di trovarmi con gente che non pensa ad altro che godere.  
Si dica o racconti o dipinga quel che si vuole,  
ma qui ogni attesa è superata.  
Queste rive, golfi, insenature, il Vesuvio,  
la città coi suoi dintorni, i castelli, le ville!...  
Siano perdonati tutti coloro che a Napoli escono di senno! "*

(Goethe – Viaggio in Italia)

# ABSTRACT

This work focuses on the role of SAR Interferometry (InSAR) in the study of many phenomena characterizing the Earth's surface. In particular, we perform several studies demonstrating how the use of this technique allow to significantly improve the knowledge of the our living planet. Moreover, we propose an advanced integration method in order to merge the InSAR data with other geodetic data, i.e. Multiple Aperture Interferometry (MAI), Pixel Offset Tracking (POT) and Global Positioning System (GPS). We apply the method to constrain the full 3D displacement field produced by the Mw 6.1 2014 South Napa Valley earthquake and then we used the results from the integration to perform the source modeling.

In the following we provide a brief description of every chapter composing this work.

The first Chapter is meant to introduce the topic of the progressive use of Remote Sensing geodetic data to support the activities of monitoring and hazard mitigation related to natural phenomena. The capability to retrieve informative contributions about the movements of the Earth's surface from the space opened interesting scenarios. We show the main methodologies with relative advantages and drawbacks. Each of the presented geodetic techniques, i.e. InSAR, MAI, POT, GPS has its own peculiarities in constraining a surface displacement field thus being suitable to be exploited in synergistic way.

Chapter 2 shows the application of the InSAR technique to reconstruct and model surface displacement fields induced by several phenomena. In particular, in this chapter are presented the case studies of the Mw 5.3 Lunigiana earthquake, occurred in northern Italy, on June 2014, the 2011-2013 Campi Flegrei caldera uplift, southern Italy, and the slow subsidence ( $\sim 20$  years of InSAR data) in the urban area of the Cassino plain, central Italy. In these cases the deformation was mainly vertical thus allowing to be well constrained by InSAR data.

In Chapter 3, the 3D coseismic displacement map due to the 2014 Mw 6.1 South Napa earthquake, occurred close the San Andreas Fault system, California, is estimated by using a method to merge InSAR and GPS data. InSAR data are one of the first acquisitions of the latest satellite of the European Space Agency (ESA), i.e. Sentinel-1, whereas the GPS data were obtained from the Bay Area Regional Deformation Network, the UNAVCO and the Crustal Dynamics Data Information System online archives.

In Chapter 4 we propose an improved method for the data integration and test it on the Napa earthquake. Geodetic data from MAI and POT are added in the processing chain and the GPS data interpolation is modified according to the specific phenomenon. Futhermore, the source modeling

is performed by inversion of the obtained 3D displacement component. The best fit is obtained by simulating a fracture in the fault segment in agreement with previous works.

Finally, in the last chapter we discuss about the advantages and disadvantages of the data integration and the future perspectives.

# CHAPTER1: GENERAL INTRODUCTION

## 1.1 OBSERVING THE EARTH FROM THE SPACE

Nowadays, satellite Earth observation is playing an important role in the knowledge of crustal phenomena characterizing our living planet. Data provided by advanced remote sensing sensors on board of spacecraft and Global Positioning System (GPS) satellite significantly improved and supported the understanding of the dynamic processes of the Earth's surface.

In particular, among the remote sensing sensors, the Synthetic Aperture Radar (SAR) represents one of the most important tool in the Earth Sciences applications being able to acquire data in any atmospheric conditions and sunlight-independently.

SAR technology was developed starting from 1951 by Carl Wiley, engineer at Goodyear Aircraft Corporation. The great technological progress in the following years made it possible mounting a SAR system on the SEASAT satellite, launched by the NASA in 1978. The system worked at 1 Ghz and was the first satellite to provide SAR data for civil use.

Therefore, starting from '90, many space agencies integrated satellites equipped with SAR sensors in their programs.

In 1991 the European Space Agency launched ERS-1 satellite with a SAR sensors operating at C-band followed by ERS-2, Envisat and the recent Sentinel-1 (Fig.1.1), launched on April 2014.

In 1995 the Canadian Space Agency (CSA) put in orbit the C-band Radarsat-1 followed, in 2007, by the second one, Radarsat-2. In 2006 the Japan Aerospace Exploration Agency (JAXA) launched ALOS-1 equipped with an L-band sensor and followed by ALOS-2 in 2014.

In 2007, the first satellite of the Cosmo SkyMed constellation and TerraSAR-X satellite were launched by the Italian Space Agency (ASI) and the German Aerospace Center (DLR), respectively. All these satellite fully exploit this technology to retrieve informations useful in the study of natural phenomena, oceanography, land cartography and archeology.



Figure 1.1: Sentinel-1 satellite

Moreover, in the last decades, several algorithms and methodologies were developed in order to properly use the information carried out by these systems.

Among them, SAR Interferometry (InSAR) [1-3] is probably the most relevant technique exploiting SAR data. In this technique, at least a pair of SAR images is used to extract information about topography or potential surface deformations of the investigated area.

Since 2000, advanced InSAR techniques such as Permanent Scatterers (PS) [4][5], Small Baseline Subsets (SBAS) [6] and Interferometric Point Target Analysis (IPTA) [7] have been developed to deeply exploit the SAR analysis working with many SAR data acquired in different times and with different perpendicular baselines.

The approaches, also named multi-pass InSAR allow following a surface displacement process providing precise measurements (millimeters accuracy) of the deformation trend and the time series. These capabilities made InSAR an important tool for the seismic and volcanic hazard mitigation [8-10][11][12], the landslides monitoring, the management of agricultural activities [13], and the study of the glaciers behavior [14][15].

However, the main drawback of the technique is related to the one-dimensional measurement. Indeed, InSAR estimate is projected onto the satellite Line-of-Sight (LOS) that means to well constrain only the vertical component (UP) of a displacement field, due to the viewing geometry. On the other hand, regarding the horizontal displacement, it is less sensitive to the East-West (EW) component and almost insensitive to the North-South (NS) component.

In order to overcome the problem, other remote sensing techniques were developed and also GPS data can be exploited.

Based on a pair of SAR data, both Multiple Aperture Interferometry (MAI) [16] and Pixel Offset Tracking (POT) [17] are able to constrain the displacement component along the azimuth direction, i.e. along the satellite line of flight. Because of the quasi-polar orbits ( $\sim 10^\circ$ ) traveled by the satellites (Fig.1.2), the satellite line of flight is almost parallel to the geographic north and subsequently, the azimuth displacement is almost corresponding to the NS one.

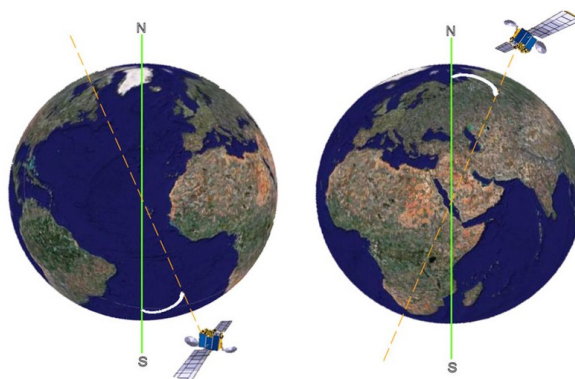


Figure 1.2: Ascending and Descending satellite orbits

In addition, several GPS networks were placed in many areas of the world to support the studies of crustal deformation phenomena.

The GPS system was developed in 1973 by the US Department of Defense and is fully operative since 1995. It consists of a network of 32 dedicated satellites continuously providing to any GPS receiver informations about time and its location in terms of geographic coordinates (NS, EW and UP). Based on the transmission of a radio signal, the system works in all weather conditions, anywhere on or near the Earth according to the availability and the position of the satellites with respect to the receiver and is freely accessible.

Unlike SAR data, GPS data are characterized by good temporal resolution but sparse spatial resolution due to the quite high cost of GPS receivers.

Therefore, in some case studies can be suitable the simultaneous exploitation of GPS and SAR data (treated with InSAR, MAI and POT approaches) in order to constrain all the components of a deformation process.

Indeed, the different capabilities of these data sources make them compatible with a synergic and combined approach aiming at estimating the 3D surface displacement map caused by a natural and/or anthropic phenomenon.

## 1.2 INSAR OUTLINE

In general, a SAR image is a 2-D projection of the 3-D observed area. Indeed, a SAR system is able to estimate only the range and azimuth coordinates of every point target thus generating an ambiguity about their correct location. To better understand this point let us refer to the Figure 1.3 where the azimuth coordinate has been fixed:

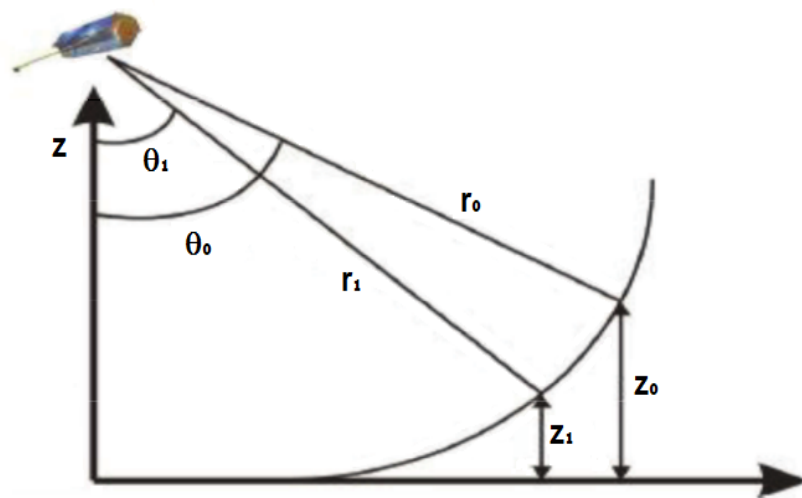


Fig 1.3: SAR geometry with fixed azimuth coordinate

It is evident that the range coordinate is not sufficient for determining the target location since all the point at the same range distance by the radar will be identified by the same pixel in the SAR image. Therefore, in order to solve the ambiguity about the target location, the knowledge of the third target coordinate, i.e. the angle wherewith the target is observed by the radar or equivalently the target height, is needed. This information, the so named incidence angle, can be obtained by considering a second SAR image of the same area acquired by a slightly different position with respect to the first one.

The criterion is very similar to the “eye-system”: a single eye provide a 2D view but the joint use of both eyes allows us to get the distance, and then the 3D view of the observed object.

In a very similar way, the joint use of two SAR image, acquired by slightly different positions allows to determine the target height thus allowing the discrimination of the targets located at the same range distance.

The use of at least a pair of SAR image is the principle of SAR Interferometry technique. In particular, the information carried by the phase difference between two or more complex SAR images is exploited for determining the topography or any surface deformations of the investigated area. The images used in this technique can be acquired at the same time, by two sensors installed on the same platform (Single – Pass Interferometry) or in different time by the same sensor (Repeat – Pass Interferometry).

To understand the InSAR principle let us consider the Figure 1.4.

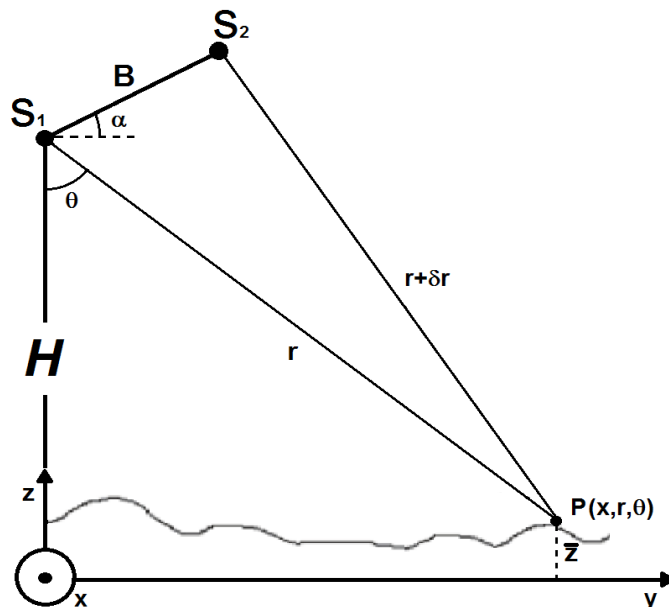


Figure 1.4: InSAR Geometry

By observing the InSAR geometry in Figure 1.3 is already possible to note how the ambiguity about the target location is solved. Indeed, for any fixed height  $\bar{z}$  there is one and only one point target  $P(x, r, \theta)$ , located, at the same time, at distance  $r$  from the position of the first acquisition and  $r+\delta r$  from the position of the second acquisition, respectively.

From the analytical point of view, the two backscattered signals can be expressed as follow:

$$i_1(x', r') = \iint \gamma(x, r) e^{-j\frac{4\pi}{\lambda}r} \text{sinc}(a(x'-x)) \text{sinc}(b(r'-r)) dx dr \quad (1.1)$$

$$i_2(x', r') = \iint \gamma(x, r) e^{-j\frac{4\pi}{\lambda}(r+\delta r)} \text{sinc}(a(x'-x)) \text{sinc}(b(r'-r-\delta r)) dx dr \quad (1.2)$$

For sake of simplicity let us consider the  $\delta r$  constant for any  $x$  and  $r$ , so that:

$$i_2(x', r') = e^{-j\frac{4\pi}{\lambda}\delta r} \iint \gamma(x, r) e^{-j\frac{4\pi}{\lambda}r} \text{sinc}(a(x'-x)) \text{sinc}(b(r'-r-\delta r)) dx dr \quad (1.3)$$

Due to the different geometry of acquisition there is a sort of misalignment between the two images that have to be estimated. This step is named coregistration and consists in the translation of  $\delta r$  an image, the slave, in the grid of the other one, the master.

Therefore, after the coregistration step we have:

$$i_2(x', r'+\hat{\delta r}) = e^{-j\frac{4\pi}{\lambda}\delta r} \iint \gamma(x, r) e^{-j\frac{4\pi}{\lambda}r} \text{sinc}(a(x'-x)) \text{sinc}(b(r'-r-\delta r+\hat{\delta r})) dx dr \quad (1.4)$$

or equivalently:

$$i_2(x', r'+\hat{\delta r}) = i_1(x', r') e^{-j\frac{4\pi}{\lambda}\delta r} \quad (1.5)$$

Then, the interferogram is obtained by multiplying the first image for the complex conjugate of the second one:

$$i_1(x', r') \cdot i_2^*(x', r'+\hat{\delta r}) = |\gamma|^2 e^{-j\frac{4\pi}{\lambda}\delta r} \quad (1.6)$$

where the quantity:

$$\varphi = \frac{4\pi}{\lambda} \delta r \quad (1.7)$$

is called interferometric phase.

Since the phase in 1.7 is defined in the interval  $(-\pi, \pi]$ , another step named phase unwrapping is needed to retrieve the information about the height of the investigated area.

Then, when the unwrapped phase is known, the incidence angle (or equivalently the height) is given by applying the Carnot theorem with reference to the Figure 1.4:

$$(r + \delta r)^2 = r^2 + B^2 - 2rB \sin(\theta - \alpha) \quad (1.8)$$

Since  $(B, \delta r) \ll r$ , we have:

$$\sin(\theta - \alpha) \simeq \frac{-\delta r}{B} \quad (1.9)$$

Then, by 1.7 and 1.9 we obtain the relationship between  $\varphi$  and  $\theta$ :

$$\varphi = \frac{-4\pi B}{\lambda} \sin(\theta - \alpha) \quad (1.10)$$

Finally, the geocoding is used in order to move to another reference system (UTM, WGS-84). For example here we move to the radar coordinate system  $(x, r, \theta)$  to the cartesian one  $(x, y, z)$ :

$$\begin{aligned} x &= x \\ y &= r \sin(\theta) \\ z &= H - r \cos(\theta) \end{aligned} \quad (1.11)$$

SAR Interferometry exploits the information in the phase difference for estimating the  $\delta r$ , being related to the height  $z$  and thus allowing to reconstruct the altitude profile of the investigated area.

However, if the topography is already known and the contribution of interest is related to potential deformations occurred because of seismic or volcanic activities or other phenomena, small variations in the original technique are needed. Indeed, the so-called Differential SAR

Interferometry exploits the information carried out by the phase difference between two or more SAR images acquired in different time from, in theory, the same orbit position. In this way, it is able to measure the ground deformation occurred in between and retrieve displacement maps with millimeter accuracy.

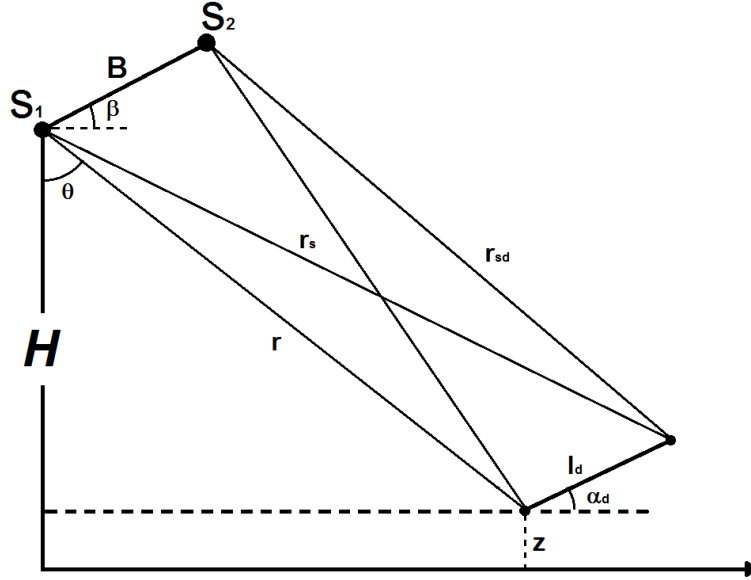


Figure 1.5: Differential InSAR Geometry

Let us consider the figure 1.5 where  $S_1$  and  $S_2$  are the position of the satellite at the time  $t_1$  and  $t_2$  respectively and let us suppose that  $l_d$  is the target displacement between  $t_1$  and  $t_2$ .

Then,  $r_{sd}$  is the range distance between the target and the sensor at the time  $t_2$  after the target displacement  $l_{sd}$  whereas  $r_s$  is the same distance estimated without any deformation.

By 1.7 the interferometric phase given by:

$$\varphi = \frac{4\pi}{\lambda} r_{sd} - \frac{4\pi}{\lambda} r \quad (1.11)$$

It can be rewritten as follows:

$$\frac{\lambda \varphi}{4\pi} = r_{sd} - r_s + r_s - r = \delta r_d + \delta r \quad (1.12)$$

where  $\delta r$  is the path estimated without any deformation.

Assuming ideal conditions, i.e.  $S_1=S_2$  (same positions at  $t_1$  and  $t_2$ ), the topography is zero and the

interferometric phase is only given by the deformation contribution:

$$\varphi = \frac{4\pi}{\lambda} \delta r_d \quad (1.13)$$

Unfortunately, despite of the stability of the orbits a small topographic contribution is always present. In addition, some error contribution, i.e. the atmospheric contribution and the contribution due to the instrumental noise, affect the interferometric phase that can be, then, rewritten as:

$$\varphi = \varphi_{disp} + \varphi_{topo} + \varphi_{atm} + \varphi_{noise} \quad (1.14)$$

Therefore, in order to retrieve information about the surface displacement the others contribution have to be compensated using an external Digital Elevation Model (DEM) and specific filtering techniques.

### 1.3 GPS OUTLINE

The GPS is a satellite navigation system able to provide both location and time information about any target equipped with a GPS receiver. It is based on the trilateration technique (method of spherical positioning) that allows locating a target by measuring the time needed by the signal to cover the GPS satellite – GPS receiver distance.

In particular, a GPS satellite continuously transmits a signal encoding several informations such as its current time, its position and the health of the network. Each GPS satellite is equipped with stable atomic clock, synchronized to each other in order to provide very precise informations about location and time.

On the other hand, a GPS receiver receives the information about the time of transmission and compares it with the time of arrival according to its internal clock. Then, it computes the time of flight which is approximately equivalent to the receiver-satellite distance taking into account for the velocity of propagation of the signal, i.e. the speed of light. Unfortunately, the receivers clocks are less stable and need a further information about the deviation from the satellite time to be properly synchronized.

Therefore, a GPS receiver needs monitoring at least four satellites (Fig.1.6) simultaneously to determine its exact position and the offset from the satellite clock solving a system of four equations

in four unknowns (three position coordinates and clock deviation).

The transmitted message consists of a 500-bit-long frame made up of five subframes, each subframe being 300 bits (6 seconds) long. The first subframe contains the information about the GPS satellite clock, i.e. the number of the week and the time within the week. The second and the third subframes encode the satellite position using precise orbit informations, the so called ephemeris. The last two subframes carry on the almanac containing data related coarse orbits and error correction. The ephemeris is updated every 2 hours and is generally valid for 4 hours, with provisions for updates every 6 hours or longer in non-nominal conditions. The almanac is updated typically every 24 hours.

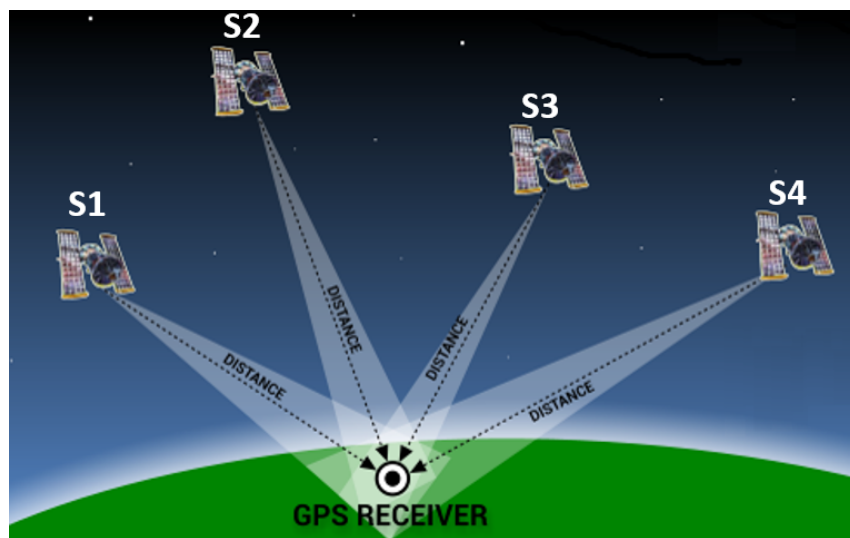


Figure 1.6: GPS geometry

The entire GPS system is composed by three segments: the space segment (SS), the control segment (CS) and the user segment (US).

The space segment includes 32 GPS satellites in Medium Earth Orbit (MEO) and the payload needed to put them into orbit.

The control segment consists in a master control station (MCS), an alternate master control station, and a host of dedicated and shared ground antennas and monitor stations.

Both the space and the control segment were developed and managed by the U.S. Air Force. The user segment is composed by all the users exploiting the capabilities of the system by using a GPS device (antenna, receiver-processor and stable clock). It includes both military users of the secure GPS Precise Positioning Service civil, commercial, and scientific users of the Standard Positioning Service.

## 1.4 MAI OUTLINE

The MAI technique exploits the SAR Interferometry in order to constrain the azimuth displacement that is approximately parallel to the NS deformation component [16]. It is based on the estimation of phase slope between upper and lower azimuth sub-bands. In particular, two interferograms, the forward- and backward-looking interferograms, are constructed in the along-track direction using sub-aperture of the antenna beam and then the shift along the azimuth direction is directly estimated. With reference to figure 1.7, let be  $\theta_{SQ}$  the radar nominal squint angle: the forward looking interferogram is obtained by using a radar squint angle slightly greater than the nominal one,  $\theta_{SQ}+\beta$ . Similarly, the backward interferogram is constructed around a LOS slightly backward to the nominal one.

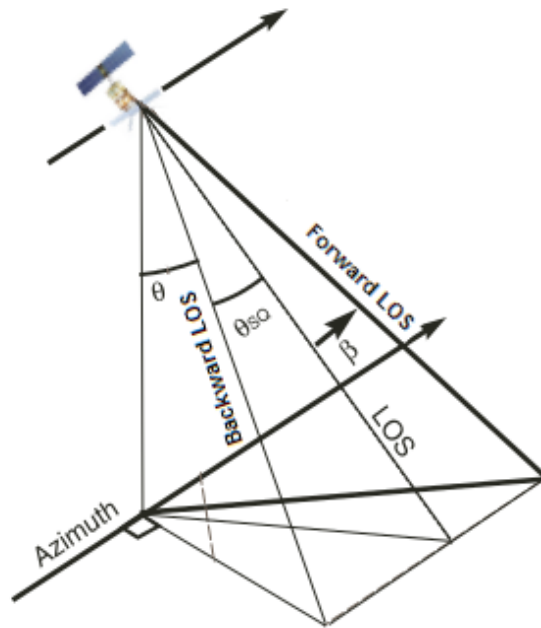


Figure 1.7: MAI Geometry

Assuming no across-track displacement, for any displacement along the azimuth direction,  $\Delta x$ , the interferometric phases are the following:

$$\varphi_{Forward} = \frac{-4\pi\Delta x}{\lambda} \sin(\theta_{SQ} + \beta) + \varphi_{top} + \varphi_{err} \quad (1.15)$$

$$\varphi_{Backward} = \frac{-4\pi\Delta x}{\lambda} \sin(\theta_{SQ} - \beta) + \varphi_{top} + \varphi_{err} \quad (1.16)$$

The azimuth displacement is then directly estimated by subtracting the two phases:

$$\varphi_{MAI} = \varphi_{Forward} - \varphi_{Backward} = \frac{-4\pi\Delta x}{\lambda} 2\sin(\beta)\cos(\theta_{SQ}) \approx \frac{2\pi}{L}\Delta x \quad (1.17)$$

## 1.5 POT OUTLINE

POT is another remote sensing technique [17] able to constrain the along-track movements (i.e. the azimuth displacement). It is less accurate with respect to MAI but provide both along-track and across-track (i.e. along LOS) displacement thus allowing to cross-validate InSAR LOS data. In addition, it is not affected by decorrelation problem working on the intensity of the back-scattered signal and returns unambiguous measurements since there is no need for phase unwrapping, one of the most critical step in InSAR and MAI.

The method is based on the estimation of the slant-range and azimuth offsets between two SAR images by a cross-correlation function.

The cross-correlation function searches for its maximum within a search window and the offsets are estimated by a 2D shift of the cross-correlation peak with respect to the centre of the search window (Fig.1.7). The accuracy of the estimation depends on the presence of nearly identical features in the two images. If the coherence is quite high the cross-correlation peak can be found by searching for the same speckle pattern in the two images (speckle tracking). Otherwise, for incoherent areas, POT requires larger search windows searching for common features in the two images (feature tracking). Obviously, in order to retrieve the azimuth and the LOS displacement the image offsets due to the different orbit configurations needs to be estimated and subtracted.

Usually, the orbital offset is estimated in correspondence of stable reference points where the assumption of “zero displacement” is satisfied. Then, it is extended globally in the SAR images by fitting a bilinear polynomial function. Finally, after the separation of the orbital offsets, the residual shifts in the slant-range and azimuth directions is ascribable to displacements occurred along these two directions in the time between the two SAR acquisitions.

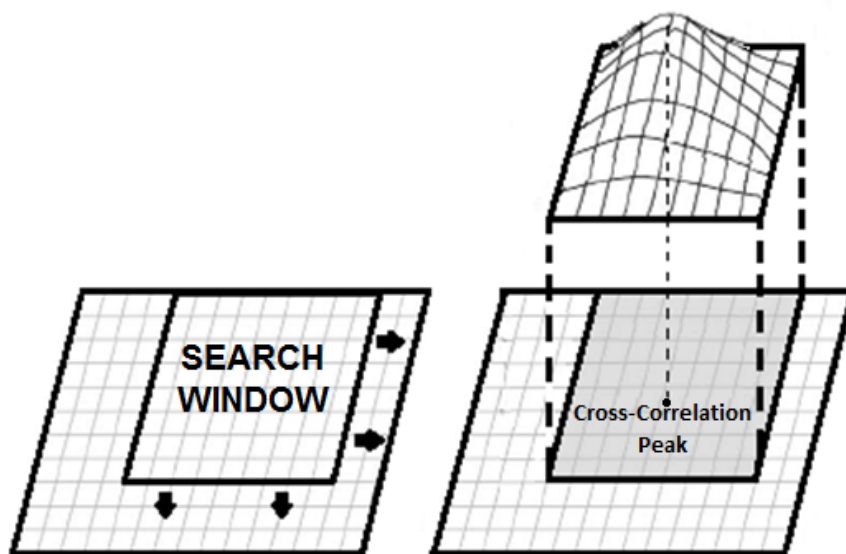


Figure 1.8: POT rationale

## REFERENCES

- [1] Bamler R. and Hartl P., Synthetic aperture radar interferometry, *Inverse Problem*, Vol. 14, No. 4, 1998.
- [2] Bürgmann R., Rosen P.A. and Fielding E.J., Synthetic Aperture Radar Interferometry to Measure Earth's Surface Topography and Its Deformation, *Earth and Planetary Sciences*, Vol. 28, pp. 169-209, 2000.
- [3] Ferretti A., Monti-Guarnieri A., Prati C., Rocca F., Massonnet D., *InSAR Principles: Guidelines for SAR Interferometry Processing and Interpretation*, ESA Publications, TM 19, ISBN: 92-9092-233-8, 2007.
- [4] Ferretti, A.; Prati, C.; Rocca, F. Nonlinear subsidence rate estimation using permanent scatterers in differential SAR interferometry. *IEEE Trans. Geosci. Remote Sens.* 2000, 38, 2202–2212.
- [5] Ferretti, A.; Prati, C.; Rocca, F. Permanent scatterers in SAR interferometry. *IEEE Trans. Geosci. Remote Sens.* 2001, 39, 8–20.
- [6] Berardino, P.; Fornaro, G.; Lanari, R.; Sansosti, E. A new algorithm for surface deformation monitoring based on small baseline differential SAR interferograms. *IEEE Trans. Geosci. Remote Sens.* 2002, 40, 2375–2383.
- [7] Werner, C.; Wegmuller, U.; Strozzi, T.; Wiesmann, A. Interferometric point target analysis for deformation mapping. In *Proceedings of the 2003 IEEE International Geoscience and Remote Sensing Symposium*, Toulouse, France, 21–25 July 2003; pp. 4362–4364.
- [8] Massonnet, D.; Rossi, M.; Carmona, C.; Adragna, F.; Peltzer, G.; Feigl, K.; Rabaute T. The displacement field of the Landers earthquake mapped by radar interferometry. *Nature* 1993, 364, 138–142.
- [9] Peltzer, G.; Rosen, P. Surface displacements of the 17 May 1993 Eureka Valley, California, earthquake observed by SAR interferometry. *Science* 1995, 268, 1333–1336.
- [10] Stramondo, S.; Tesauro, M.; Briole, P.; Sansosti, E.; Salvi, S.; Lanari, R.; Anzidei, M.; Baldi, P.; Fornaro, G.; Avallone, A.; et al. The September 26, 1997 Colfiorito, Italy, earthquakes: Modeled coseismic surface displacement from SAR interferometry and GPS. *Geophys. Res. Lett.* 1999, 26, 883–886.
- [11] Massonnet, D.; Briole, P.; Arnaud, A. Deflation of Mount Etna monitored by spaceborne radar interferometry. *Nature* 1995, 375, 567–570.
- [12] Fomelis, M.; Trasatti, E.; Papageorgiou, E.; Stramondo, S.; Parcharidis, I. Monitoring Santorini volcano (Greece) breathing from space. *Geophys. J. Int.* 2013, 193, 161–170.
- [13] Wegmüller, U.; Werner, C. Retrieval of vegetation parameters with SAR interferometry. *IEEE Trans. Geosci. Remote Sens.* 1997, 35, 18–24.
- [14] Goldstein, R.; Engelhard, R.; Kam, B.; Frolich, R. Satellite radar interferometry for monitoring ice sheet motion: application to an Antarctic ice stream. *Science* 1993, 262, 1525–1530.
- [15] Kenyi, L.W.; Kaufmann, V. Estimation of rock glacier surface deformation using SAR

interferometry data. *IEEE Trans. Geosci. Remote Sens.* 2003, 41, 1512–1515.

[16] Bechor N.B.D. and Zebker H.A., Measuring two-dimensional movements using a single InSAR pair. *Geophys. Res. Lett.*, 33, L16311, 2006.

[17] Joughin I., Ice-sheet velocity mapping: a combined interferometric and speckle-tracking approach., *Ann. Glaciol.*, 34, 195–201, 2002.

# **CHAPTER 2: INSAR APPLIED TO THE STUDY OF SURFACE DEFORMATIONS DUE TO NATURAL OR ANTHROPIC PHENOMENA\***

## **2.1 INTRODUCTION**

A natural phenomenon such as an earthquake, a volcano eruption or a landslide is composed by three steps: the pre-the co- and the post-event phase.

The pre and the post-event phases are characterized by slow deformation processes that can be analyzed by long-time spans InSAR data according to the related hazard level.

On the other hand, the co-event phase, i.e. the phase in which the phenomenon occurs, can be studied by a single pair of InSAR data being concentrated within a short time.

The possibility offered by the satellites launched by the different space agencies such as ALOS 1-2 of the Japan Aerospace Exploration Agency (JAXA), ERS 1-2, Envisat and Sentinel-1 of the European Space Agency (ESA), Radarsat 1-2 of the Canadian Space Agency (CSA), TerraSAR-X of a public-private-partnership between the German Aerospace Center (DLR) and EADS Astrium and Cosmo-SkyMed of the Italian Space Agency (ASI) are various and can be exploited in several case studies.

SAR sensors working at L-band (ALOS 1-2), C-band (ERS 1-2, Envisat, Radarsat, Sentinel-1) and X-band (TerraSAR-X, Cosmo-SkyMed) and with different acquisition modes such as the Stripmap mode, the Spotlight mode and the ScanSAR mode allow acquiring data with different pixel resolution and area coverage. Therefore, according to the investigated scenario and the required application both small and large scale phenomena can be detected.

In this chapter the capabilities of InSAR technique in the study of surface displacement field induced by natural and anthropic phenomena are presented.

In particular, three case studies are shown concerning the study of an earthquake, a volcano and urban subsidence, respectively.

The outcomes from the study of the 2013 Lunigiana earthquake [1], northern Italy, are presented in section 2.2 Two pair of X-band Cosmo-SkyMed and C-band Radarsat-2 InSAR data were used to detect the coseismic displacement produced by the earthquake although its relatively small magnitude.

Section 2.3 is focused on the study of the uplift occurred during 2011-2013 at Campi Flegrei caldera [2], southern Italy. The area is strongly characterized by surface movements because of the underlying volcanic activity and is consistently monitored due to the high volcanic risk.

Finally, section 2.4 highlights the results obtained by InSAR analysis in detecting slow subsidence, in the order of mm/year, in the Cassino plain, central Italy [3]. In this case were applied long time span InSAR data ranging from 1992 and 2010 provided by ERS and Envisat satellite. These studies reveal the usefulness of InSAR analysis, supported by geological surveys and other kind of data and measurements, for improving the knowledge of the crustal phenomena.

## 2.2 LUNIGIANA EARTHQUAKE

On June 21st, 2013 an  $M_w$  5.3 earthquake occurred north of the Apuan Alps in the Northern Apennines (Italy) [4]. In particular, the area affected by the seismic event is in Tuscany region, between the Lunigiana area to NW and the Garfagnana to SE (Fig.2.1). In spite of its magnitude, the mainshock was felt over a broad area although not causing relevant damages in the epicentral area. The whole seismic sequence includes an  $M_w$  3.4 foreshock on June 15th and more than 2450 aftershocks with a maximum magnitude of 4.4.

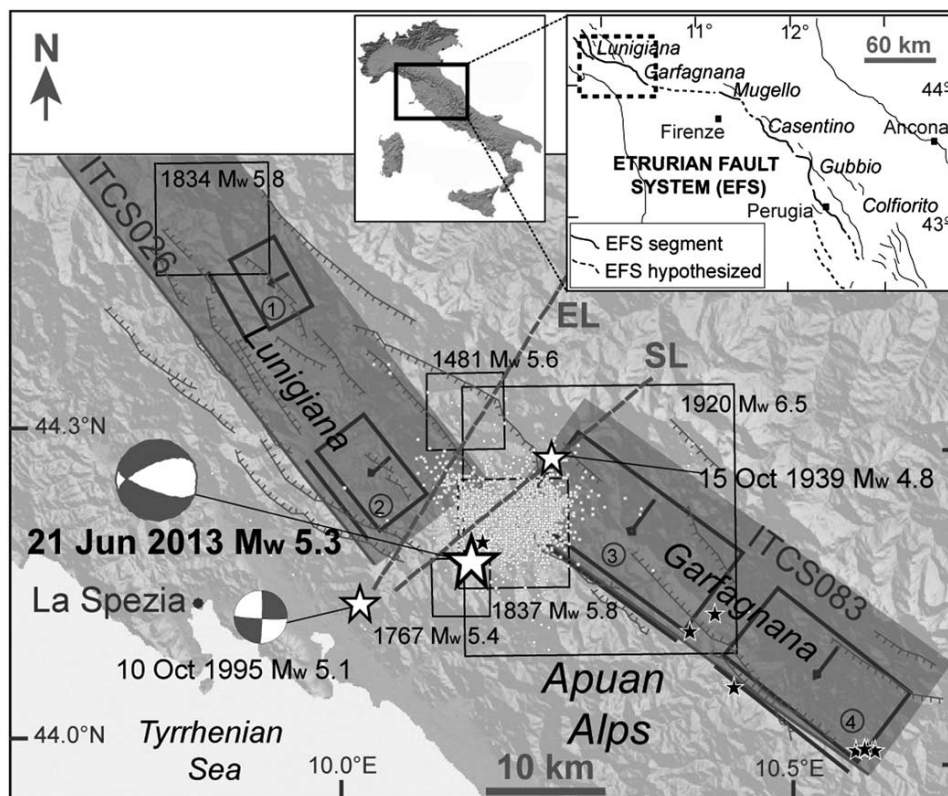


Fig. 2.1 [1]: Structural sketch of the Lunigiana and Garfagnana area with the June 21, 2013 earthquake, its focal mechanism (<http://cnt.rm.ingv.it/tdmt.html>) and the 2013 sequence. Squares: historical earthquakes having magnitude larger than 5.3; hatched lines: normal faults; dark polygon: composite seismogenic sources projection on the ground surface, black boxes: individual seismogenic sources projection onto the ground surface; black lines: up-dip projection of the seismogenic sources onto the surface 1) ITIS085-Pontremoli; 2) ITIS067-Aulla; 3) ITIS050-Garfagnana North; and 4) ITIS051: Garfagnana South

The Lunigiana and Garfagnana area is historically characterized by a dense intermediate to damaging seismicity. On April 11, 1837 an 5.8 earthquake occurred north of the Apuan Alps, causing severe damage in Minucciano village and its surroundings and was felt over a broad region reaching up the Po Plain [5], [6]. The strongest earthquake known in this region occurred on September 7, 1920 (6.5) and reached a very high epicentral intensity, devastating a wide area of Garfagnana and Lunigiana [5], [6]. Moreover, on October 15, 1939, a 4.8 earthquake occurred about 10 km to the northeast of the June 21, 2013 event [6]. More recently, on October 10, 1995, a 5.1 earthquake of with strike-slip kinematics [7]–[9] occurred about 10 km to the southwest of the 2013 seismic sequence.

From a geological point of view, Lunigiana and Garfagnana regions are characterized by a marked complexity being the northwestward termination of the regional, NW-SE trending EFS, marking the northwestern extensional border of the Northern Apennines. The NE dipping, low-angle normal EFS is rather well known in the literature due to field data and seismic reflection profiles [10], [11]. The EFS straddles the northern Apennines for about 350 km and includes the Mugello, Casentino, and Tiber extensional basins. Historical and recent seismicity show that two seismogenic normal faults border the Lunigiana and Garfagnana basins (respectively, ITCS026 and ITCS083 composite seismogenic sources in Figure 2.1; e.g., [12], [13]). The Lunigiana ITCS026 Source extends for about 50 km to the northern side of the Apuan Alps. Two individual sources (IDs 1 and 2 in Figure 2.1) are part of this Composite Source [14], [15], and are believed to be responsible for the 1834 and the 1481 earthquakes, respectively [13]. The Garfagnana ITCS083 source extends for about 40 km to the eastern side of the Apuan Alps, and is left-stepped compared to the Lunigiana. Also, the Garfagnana includes two individual sources [15]: 1) the source responsible for the destructive 1920 earthquake (ID 3; Fig. 2.1); 2) the southeastern source (ID 4; Fig. 2.1) not associated with a known historical or instrumental earthquake, whose existence is based on geological and structural evidence [13]. Between the Lunigiana and Garfagnana sources there is a complex and poorly known shear zone that locally forms the northern boundary of the Apuan Alps.

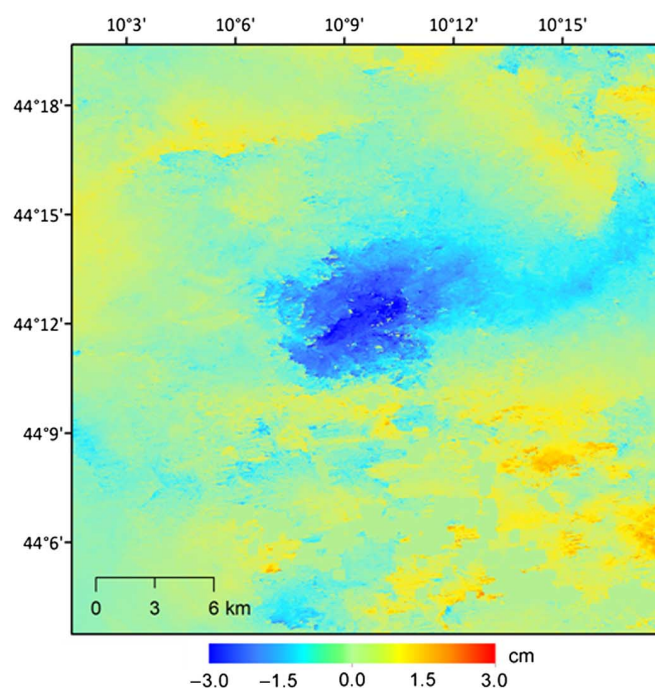
### **2.2.1 INSAR OUTCOMES**

The InSAR analysis was performed with a multiband SAR dataset, coming from X-band COSMO-SkyMed (CSK) and C-band RADARSAT-2 (RDR) SAR satellites, at high spatial resolution (3–10 m pixel). The first image pair was acquired by the CSK constellation, an Earth observation mission developed by the Italian Space Agency (ASI), consisting of a four-satellite system equipped with high-resolution X-band SAR sensors. The second image pair was acquired by the Canadian RDR satellite equipped with high resolution C-band sensor. These satellites image Earth surface in

various acquisition modes, with different ground resolutions, incidence angles and polarizations [16], and provide global coverage independent on weather or lighting conditions.

The X-band CSK sensor imaged the epicentral region on June 21 (before the mainshock) and June 22, 2013 with a spatial baseline of 139 m along the ascending orbit. The 1-day time span is the minimum temporal interval ensured by the CSK constellation. Such a short time span minimizes temporal decorrelation that heavily affects the study region due to steep topography and dense vegetation coverage. The 40x40 km<sup>2</sup> CSK pair observed the surface with 40° incidence angle and was centered on the village of Minucciano. To improve the signal to-noise ratio, the multilook factor was set equal to 20 in order to obtain a square pixel representing an area of about 40x40 m<sup>2</sup>.

The C-band RDR imaged the epicentral region on June 18 and July 12, 2013 with a Standard-3 (S3) beam with 69 m spatial baseline along the ascending orbit. The RDR pair observed a 100x100 Km<sup>2</sup> surface with 34 incidence angle. The interferometric processing was performed with the GAMMA software [17]. The 90 m shuttle radar topographic mission (SRTM) DEM was used to remove topographic component from COSMO-SkyMed interferogram and 30 m ASTER DEM was used to remove the topographic component from RADARSAT-2 interferogram. The Goldstein filtering [18], phase unwrapping with minimum cost flow (MCF) algorithm [19] and orbital refinement were also applied to both interferograms. The results obtained from CSK data show a surface subsidence of about 3 cm in the satellite line-of-sight (LOS). This displacement is mainly due to the mainshock thanks to the short temporal baseline of 1 day. On the other hand, the larger RDR temporal baseline of 24 days results in a more pronounced subsidence of about 5 cm in the satellite LOS probably caused by the cumulated effect of aftershocks following the June 21 event and/or by postseismic deformation (Fig.2.2).



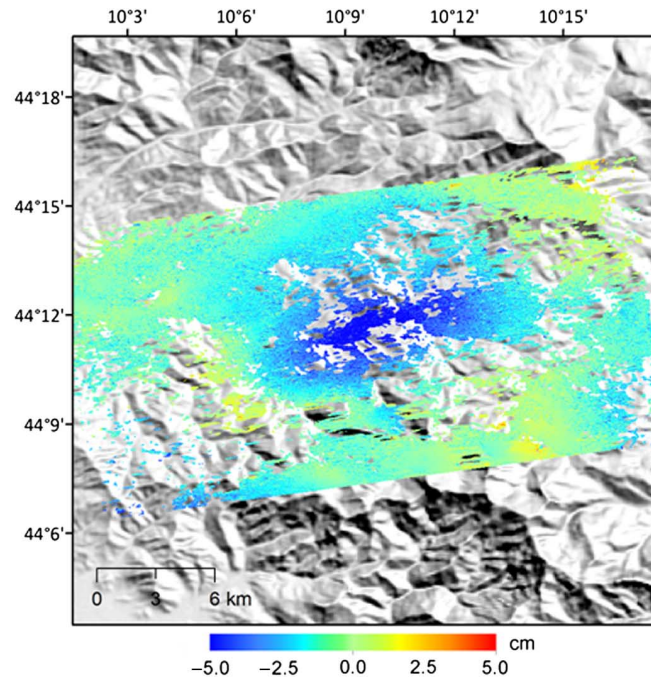


Fig. 2.2 [1]: Surface displacement detected by COSMO-SkyMed (upper) and RADARSAT-2 (bottom) DInSAR. The apparent discrepancy between the results can be ascribed to the different temporal baseline (1-day delay for COSMO-SkyMed, 24 days for RADARSAT-2) that implies additional deformation due to aftershocks and post-seismic slip release.

### 2.2.2 SOURCE MODELING

The coseismic deformation fields imaged by InSAR data was used to infer the seismic source characteristics through an inverse modeling analysis, using analytical expressions from Okada [20]. As discussed in the previous section, while the CSK interferogram is obtained from a pair of images acquired on two consecutive days, RDR interferogram has a much longer temporal baseline (24days). Therefore, it is likely that the deformation field from RDR includes the contribution of the aftershocks in the sequence as well as short-term postseismic effects. For this reason, instead of a joint modeling of the two fields, two independent source models for each deformation field have been performed.

The source geometry is obtained as the result of a two-step inversion process. First, geometry, location, and extents of the fault were estimated with a nonlinear optimization scheme, assuming uniform slip on the fault plane. Once the fault geometry is fixed, the best-fitting slip distribution on the fault plane was obtained by means of a linear inversion.

In the first step, the best-fitting uniform-slip source geometry was found by minimizing the chi-square between the observed field and the projection of the three components of the modeled field on the satellite LOS direction [21]. The fault geometry minimizing the misfit function was obtained as the result of a nonlinear inversion with the Simulated Annealing algorithm [22]. The stability of

each solution was checked by using it as a starting point for a gradient-descent optimization, and verified that the original model was recovered.

The best-fitting source parameters are listed in Table 2.1 for the two datasets, whereas the modeled deformation fields are shown in Figure 2.3.

	CSK	RDR
Center longitude	10.19 E	10.18 E
Center latitude	44.22 N	44.20 N
Top depth (km)	2.9	2.4
Strike (°)	244	247
Dip (°)	52	50
Rake (°)	-84	-87
Slip (m)	0.09	0.16
Length (km)	9.3	6.8
Width (km)	6.5	6.7

Table 2.1[1]: Source model parameters resulting from the uniform-slip inversion

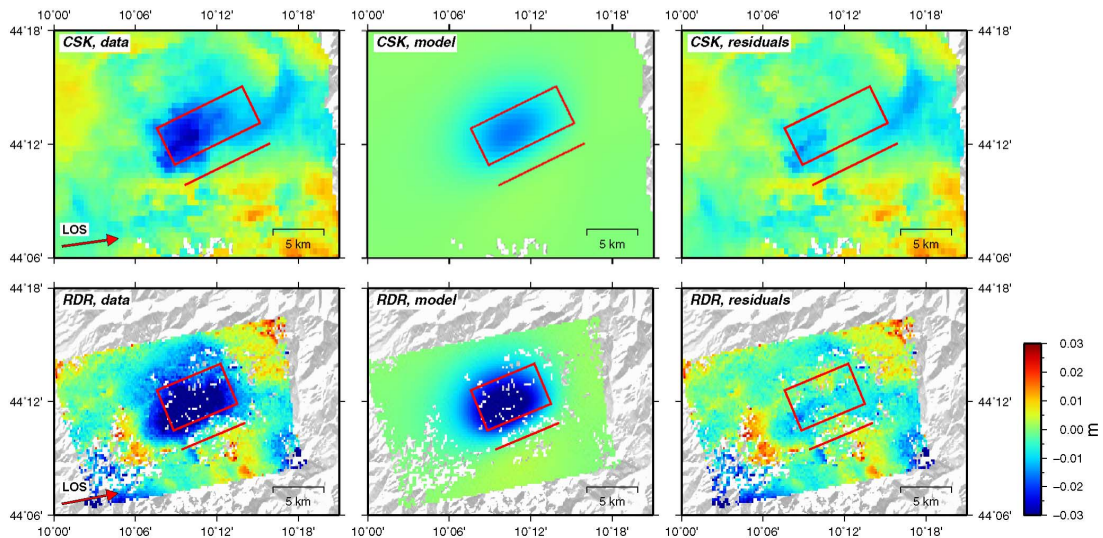


Fig. 2.3 [1]: Unwrapped LOS InSAR deformation (left), modeled deformation field (center) and residuals (right) for the CSK and RDR datasets. The red box marks the position and surface projection of the best-fitting uniform slip model. LOS indicates the satellite view direction (red arrow in left panels).

On the other hand, in order to obtain the slip distribution in the second step of the inversion, the fault geometry was subdivided into square patches of about  $0.5 \times 0.5 \text{ km}^2$ , and composed a Green Function matrix by imposing a unitary slip on each patch, computing the corresponding deformation field according to the Okada analytical expressions [20]. The linear problem is then solved by computing a natural inverse with the singular-value decomposition (SVD) algorithm, applying a damping factor in order to correct singularities in the data kernel. The estimated slip distribution on the two source models is displayed in Figure 2.4.

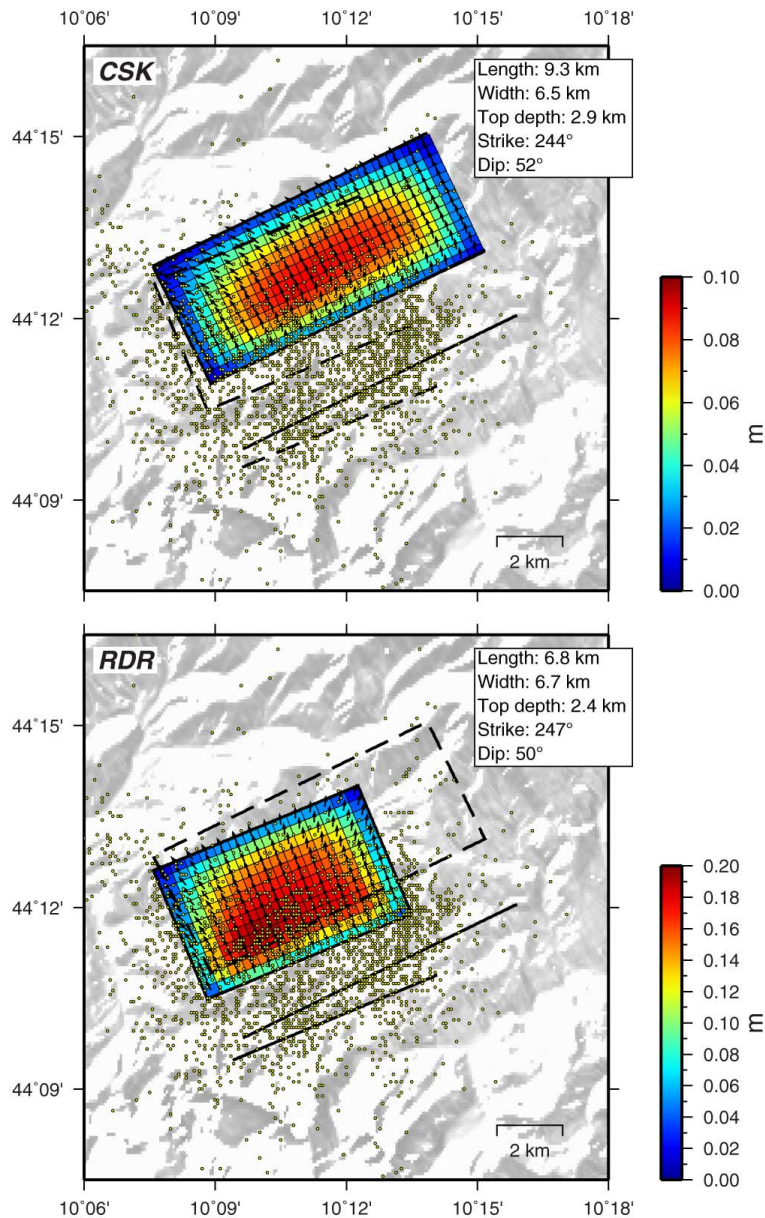


Fig. 2.4 [1]: Slip distribution models obtained with the CSK (top) and RDR (bottom) datasets. The extents and surface projection of the two source models are shown in both panels for comparison. Yellow dots show seismicity from June 21, 2013 to October 23, 2013. Color scale for the two models are different to account for the larger amount of slip in the RDR model, as a consequence of the larger temporal baseline in the RDR deformation field.

### 2.2.3 THE BREACHED RELAY RAMP

The strike, dip, and rake angles turn out to be very similar for the two inversions and indicate that rupture occurred on an NE-SW trending, NW dipping (about 50), normal fault. This geometry is consistent with RCMT and TDMT solutions, which give an extensional rupture with dip in the range 41–47. Depth extension is 2.4–7.5 km for the RDR model and 2.9–8.0 km for the CSK model. The fault models have comparable along-dip width, whereas length of the CSK model is about 50% larger than RDR model. Peak slip for the CSK model (8.8 cm) occurs at 5.1 km depth,

whereas in the RDR model peak slip (19.4 cm) is at 3.8 km depth. Geodetic magnitude for the CSK and RDR sources are M 5.24 and M 5.40, respectively, if a crustal rigidity of 26 GPa is assumed. The geodetic magnitude of the CSK model is in excellent agreement with seismological magnitudes, whereas the RDR model overestimates the magnitude. Such discrepancy can be ascribable, as already mentioned, to the larger temporal baseline (24 days) of the RDR pair, with the result that the measured deformation includes short-timescale postseismic motions as well as the cumulated effect of minor shocks occurred during the time window [23].

One of the outcomes of the model is the positioning of the source responsible for the June 21 earthquake within the transfer zone. Furthermore, the study has pointed out the structural style of linkage between the Lunigiana and Garfagnana fault segments thus suggesting toward identifying a breached synthetic relay ramp [24] (Fig. 2.5).

It can be noted how the integrated analysis of different data sources (DInSAR, geological data), together with the historical seismicity (1767 5.4 and 1837 5.8 earthquakes), suggests that the relay ramp between Lunigiana and Garfagnana is a seismogenic structure potentially responsible for earthquakes larger than 5.3.

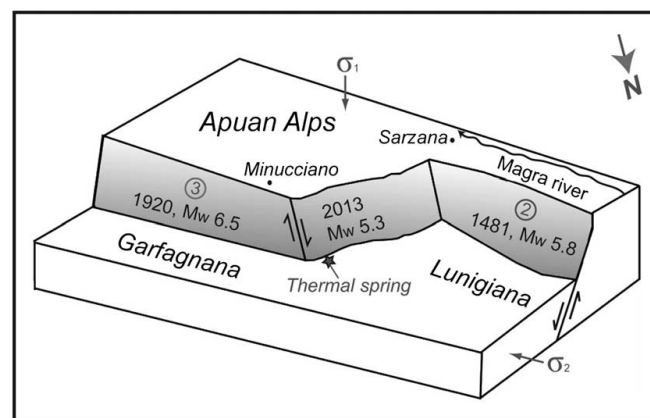


Fig. 2.5 [1]: Block diagram with the simplified fault geometry of the Lunigiana and Garfagnana areas. The source responsible for the 1920 earthquake (ID 3—Garfagnana North Source, see also Fig. 1) is schematically linked to the source responsible for the 1481 earthquake (ID 2—Aulla Source) by the relay ramp hosting the June 21, 2013 fault. Notice the presence of the Equi Terme thermally anomalous spring.

## 2.3 CAMPI FLEGREI UPLIFT

Campi Flegrei (CF) caldera is a volcanic district in southern Italy, nearby the city of Naples. Two main eruptions, dated 35 ka and 15 ka ago, have been predominantly responsible for its formation [25]. The area is characterized by one of the highest volcanic risk worldwide, due to the density of inhabitants (1800/km<sup>2</sup>) and the persistent activity of the system. Spectacular ground level variations,

known as bradyseism phenomenon, are reported at CF across the centuries. Recently, a large unrest episode took place during 1982–1984, with up to 1.8 m vertical uplift in the caldera center in Pozzuoli. A slow deflation phase began in 1985, interrupted by minor uplift episodes of few centimeters, seismic swarms and degassing episodes in 1989, 2000, and 2004–2006, recovering only about half of the 1982–1984 uplift. Since 2005, CF has been uplifting again, with a rate of 1 cm/yr until 2011.

An increase of the ground velocity took place in the following years, showing up to 9 cm/yr in 2012 in Pozzuoli, as registered by the Neapolitan Volcanoes Continuous GPS (NeVoCGPS) network operating in the Neapolitan volcanic districts [26]. Moreover, the CF caldera hosts a large hydrothermal system that daily discharges thousands of tons of volcanic gases at the Solfatara fumarolic field (fig. 2.6), 1 km from Pozzuoli [27]. Episodic pulsed inflations of the caldera floor have led to gas injections into the hydrothermal system, accompanied by seismic swarms shallower than 2–3 km depth. Since 2000, a continuous increase of CO<sub>2</sub> concentration has been measured in the emissions at Solfatara, due to the increment of the relative amount of magmatic CO<sub>2</sub> rich fluids in the shallow hydrothermal system [27].



Fig. 2.6: Fumarolic activity at the Solfatara, Campi Flegrei caldera

### 2.3.1 INSAR AND GPS DATA

InSAR data consists in two datasets of X-band Cosmo-SkyMed images acquired along ascending and descending orbits. The descending dataset has an incidence angle of 27° and is composed by 46 images, from February 2011 to December 2013. On the other hand, the ascending dataset has an incidence angle of 50° and shows a much denser temporal sampling of 168 images, more than one image per week, from January 2011 to September 2013.

In the data processing the multibaseline approach of GAMMA Interferometric Point Target Analysis (IPTA) software package [28] was exploited, setting the thresholds for the maximum perpendicular

and temporal baselines according to the different temporal sampling of the descending (500 m, 15–170 days) and ascending (50 m, 30–50 days) datasets. Moreover, data were smoothed by applying multilook factors in order to obtain pixels of about  $20 \text{ m} \times 20 \text{ m}$ . The topographic InSAR phase component was removed with the Shuttle Radar Topography Mission (SRTM) 90 m digital elevation model. The interferograms showing strong atmospheric disturbance, unwrapping problems, and large decorrelated areas were discarded, collecting 77 ascending and 33 descending interferograms.

Figure 2.7 shows cumulative displacement maps from 31 May 2011 to 5 May 2013. The reference point, i.e the point at zero displacement, was fixed in the stable area north of Quarto.

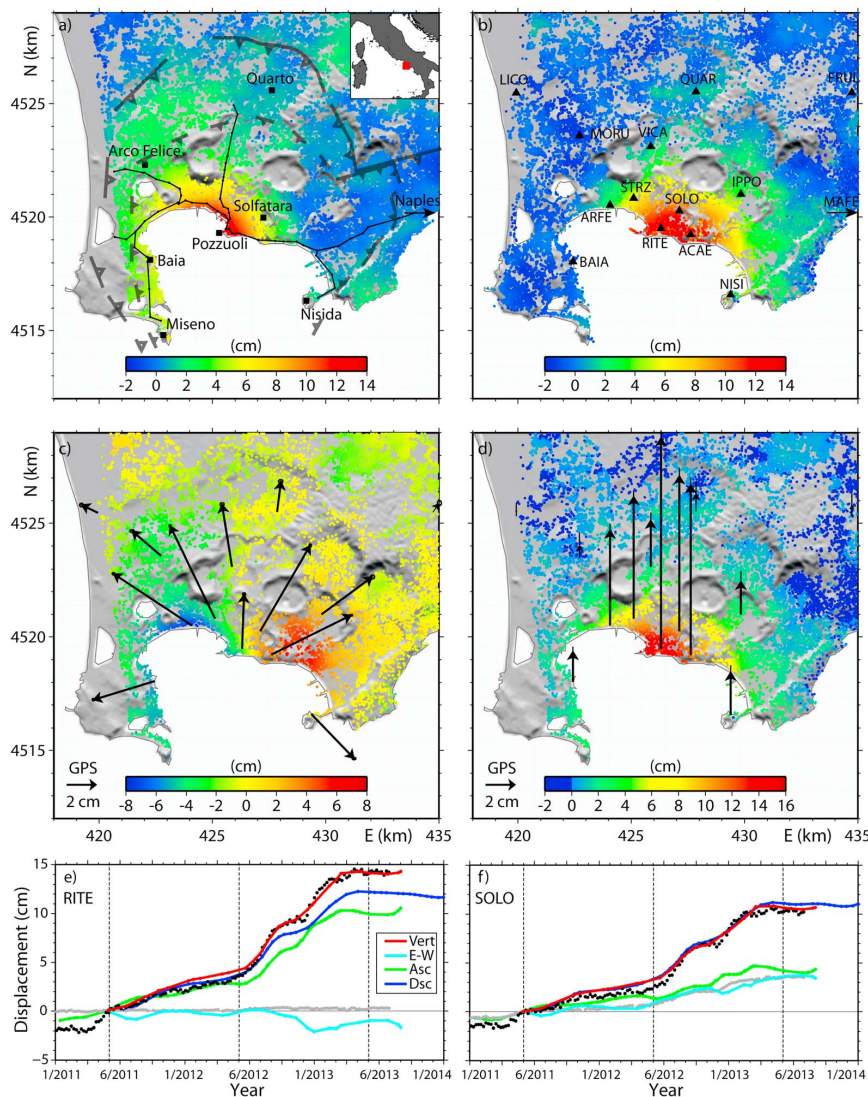


Figure 2.7 [2]: Line of sight cumulative displacements in (a) ascending and (b) descending orbits from CSK between 31 May 2011 and 5 May 2013. In Figure 1a, the outer/inner rims of the CF caldera are shown with open/full triangles, while the black lines are the 1980s leveling routes. In Figure 1b, the triangles are the GPS stations. (c) E-W and (d) vertical displacements computed in the common pixels of Figures 1a and 1b. Horizontal and vertical GPS components are reported in Figures 1c and 1d, respectively. UTM-WGS84 projection, zone 33 used in Figures 1a–1d. (e and f) Time series at the GPS stations RITE and SOLO (vertical, black dots and E-W, grey dots) and corresponding InSAR data

The resulting deformation field is characterized by a semicircular pattern centered in the Pozzuoli harbor (Figures 2.7a and 2.7b). In addition, in order to validate the results, GPS data from 14 stations of the NeVoCGPS network have been also employed [26]. The horizontal GPS vectors and the computed E-W InSAR data reveal a quite radial pattern centered in Pozzuoli (Fig. 2.7c). The computed vertical InSAR data measure 16 cm uplift in Pozzuoli and disclose a slightly subsiding far field belt undetected by GPS (Fig. 2.7d). The time series of RITE (in Pozzuoli) and SOLO (in Solfatara) show a good agreement between the vertical GPS and InSAR data (Figures 2.7e and 2.7f), with values up to 14–15 cm and 11 cm, respectively. Quantitative comparisons between InSAR and GPS mean velocities are reported in Tables 2.2.

STATION	LATITUDE	LONGITUDE	SAR (m/y)	GPS (m/y)
ACAE	40,8209	14,1417	$0.015 \pm 0.003$	$0.017 \pm 0.003$
ARFE	40,8323	14,0993	$0.036 \pm 0.003$	$0.032 \pm 0.004$
BAIA	40,8098	14,0802	$0.021 \pm 0.004$	$0.019 \pm 0.003$
FRUL	40,8779	14,2253	$-0.001 \pm 0.002$	$-0.001 \pm 0.002$
IPPO	40,8371	14,1679	$-0.004 \pm 0.002$	$-0.007 \pm 0.003$
MORU	40,8596	14,0830	$0.007 \pm 0.002$	$0.007 \pm 0.002$
NISI	40,7972	14,1630	$0.004 \pm 0.003$	$-0.001 \pm 0.002$
QUAR	40,8777	14,1437	//	//
RITE	40,8233	14,1262	$0.043 \pm 0.004$	$0.040 \pm 0.004$
SOLO	40,8303	14,1357	$0.018 \pm 0.003$	$0.014 \pm 0.002$
STRZ	40,8351	14,1117	$0.033 \pm 0.003$	$0.030 \pm 0.003$
VICA	40,8558	14,1205	$0.007 \pm 0.002$	$0.008 \pm 0.002$

Table 2.2 [2]: Comparison between ascending SAR and GPS displacement rate. The GPS measurements have been projected into the satellite Line of Sight (LOS) along ascending orbit. The GPS station QUAR has been used as reference point since it shows a quite stable behaviour in both datasets.

### 2.3.2 SOURCE INFERENCE

Since 90', the use of InSAR and GPS data allowed for the development of detailed source models at CF caldera.

A combined action of a penny-shaped crack at  $\sim 3.6$  km depth in a layered medium and a very shallow source below the Solfatara crater was found to suit two decades of deformation [29]. Furthermore, the tomography by Chiarabba and Moretti [30] evidenced a complex local structure at CF, characterized by a relatively high  $V_p/V_s$  anomaly in the caldera center at shallow depths, thus suggesting the presence of fluids. In addition, a sharp  $V_p/V_s$  decrease between 2 and 4 km depth indicates the absence of magmatic fluids (i.e., magma reservoirs) and the presence of rock volumes with overpressured gas. Active seismic experiments detected a melt layer  $\sim 1$  km thick at 7–8 km depth [31]. These studies at CF revealed a complex local structure that may play a role in the source parameters retrieval.

The collected geodetic data were modeled by means of the FE technique in order to account for the

elastic heterogeneities. The InSAR ascending and descending data sets were downsampled with a step of 220 m, obtaining 5530 data points. The associated uncertainty is 5 mm during 2012–2013 and 2011–2013, and 2 mm during 2011–2012.

The FE model was developed using the software MARC ([www.mscsoftware.com/it/product/marc](http://www.mscsoftware.com/it/product/marc)), while the 3-D elastic structure of the medium was directly computed from the tomography by Chiarabba and Moretti [30] (see Trasatti et al. [32] for details). The potential source is a cubic element (400 m side) representing a moment tensor  $M_{ij} = V\sigma_{ij}$  where  $V$  is its volume and  $\sigma_{ij}$  the stress tensor applied over its faces. The inversion technique consists in a direct search in the parameters space followed by a Bayesian analysis providing the Posterior Probability Density (PPD) functions [33][34].

The moment tensor is expressed in terms of principal moments  $M_1$  ( $M_1 \geq M_2 \geq M_3$ ) and three angles ( $\delta, \phi, \psi$ ) describing their eigenvectors  $\mathbf{m}_1, \mathbf{m}_2, \mathbf{m}_3$ :  $\delta$  is the dip of  $\mathbf{m}_3$  with respect to the horizontal plane,  $\phi$  is the strike of  $\mathbf{m}_3$  (measured anticlockwise from east), and  $\psi$  yields its self-rotation, i.e., the rotation of the eigenvectors  $\mathbf{m}_1$  and  $\mathbf{m}_2$  around  $\mathbf{m}_3$  (Fig. 2.8).

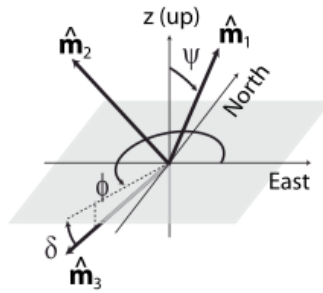


Fig. 2.8 [2]: Moment Tensor

All the preliminary tests showed a similar horizontal source position, at  $426.2 \pm 0.2$  km east and  $4518.8 \pm 0.2$  km north (UTM-WGS84 projection, zone 33), slightly offshore Pozzuoli. These two parameters are kept constant in order to limit trade-offs.

The inversions provided a source depth of 5.1 km, except for the first phase, 5.5 km (Table 2.3). No trade-offs are shown by the 2-D PPD functions. As a comparison, we inverted data for the biennium in the homogeneous model (HOM), obtaining a shallower source (3.7 km depth) and a worse fit than the heterogeneous model.

Phase	Total Misfit	Depth <sup>a</sup> (km)	$M_1^{a,b}$ ( $10^{15}$ Nm)	$M_2^{a,b}$ ( $10^{15}$ Nm)	$M_3^{a,b}$ ( $10^{15}$ Nm)	$\delta^{a,c}$ (deg)	$\phi^{a,c}$ (deg)	$\psi^{a,c}$ (deg)
2011–2012	8.2	$5.5 \pm 0.2$	$18 \pm 2$	$9 \pm 2$	$7 \pm 2$	$3 \pm 3$	$160 \pm 15$	$0 \pm 5$
2012–2013	3.5	$5.1 \pm 0.2$	$37 \pm 3$	$5 \pm 3$	$-6 \pm 3$	$2 \pm 2$	$39 \pm 14$	$0 \pm 5$
2011–2013	4.5	$5.1 \pm 0.2$	$56 \pm 3$	$16 \pm 4$	$5 \pm 3$	$2 \pm 2$	$14 \pm 14$	$0 \pm 5$
2011–2013 HOM	5.3	$3.7 \pm 0.2$	$19 \pm 2$	$13 \pm 2$	$7 \pm 2$	$2 \pm 3$	$46 \pm 14$	$0 \pm 15$

<sup>a</sup>Standard deviations are estimated from the half width of the PPD distributions  
<sup>b</sup>Principal moments retrieved.  
<sup>c</sup>Angles describing the orientation of the principal eigenvectors

Table 2.3 [2]: Results of the Bayesian Inversion of the FE Model in the Different Phases

The moment tensor found in the first steep need to be interpreted. The red area in Figure 2.9 represents the admissible values of principal moments ratios  $M_2/M_1$  and  $M_3/M_1$  compatible with pressurized ellipsoidal sources. Another set of physically plausible sources are the mixed-mode dislocations accounting for opening and shear slip.

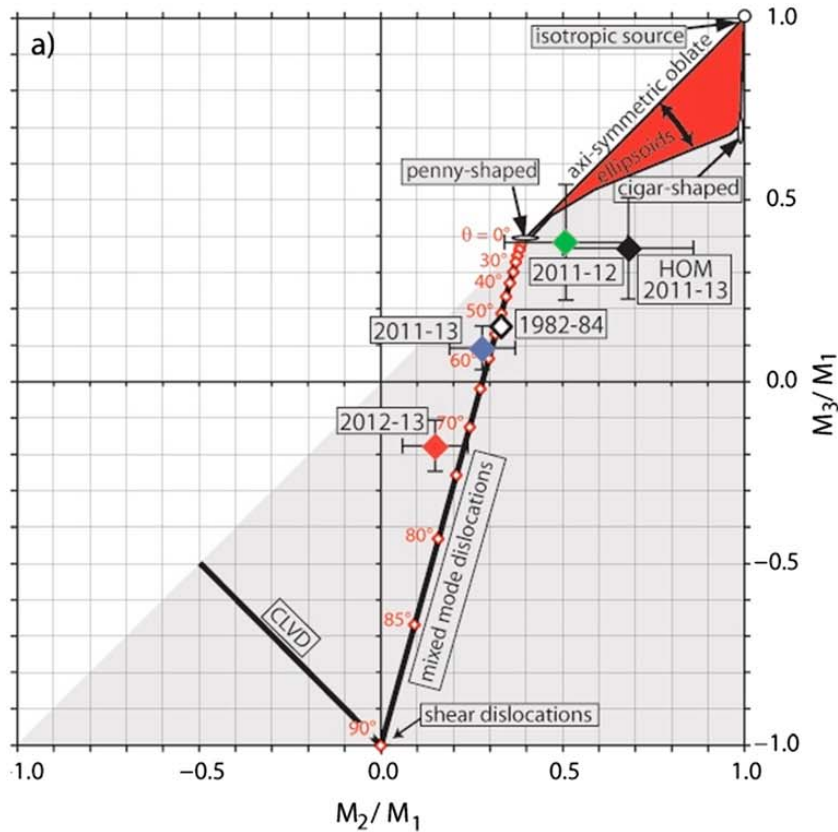


Figure 2.9 [2]: Domain of principal moments ratios and moment tensor interpretation ( $\nu = 0.28$ ). The diamonds are the mean model solutions. The 1982–1984 solution is from Trasatti et al. [2011]

The best fitting models lay, within errors, close to the mixed-mode dislocation line. Defining  $\theta$  as the angle between the normal to the dislocation plane and the slip vector, it was found that during 2011–2012 the crack is purely inflating ( $\theta \sim 0^\circ$ ), in 2012–2013 the shear component is relevant ( $\theta \sim 72^\circ$ ), while the biennium presents an averaged solution.

This indicates that the two phases of the unrest share the same source position but a different source mechanism: a pressurized crack undergoing to a shear dislocation whose intensity varies through time.

The 2011–2013 surface deformation pattern is fitted with residuals lower than 3 cm (Figure 2.10). The nonaxisymmetric source helps to reproduce the nonperfectly radial horizontal deformation pattern. The negative trend of the E-W InSAR residuals compensates with the negative trend of the GPS vertical residuals. Similar results are obtained for the second year of unrest.

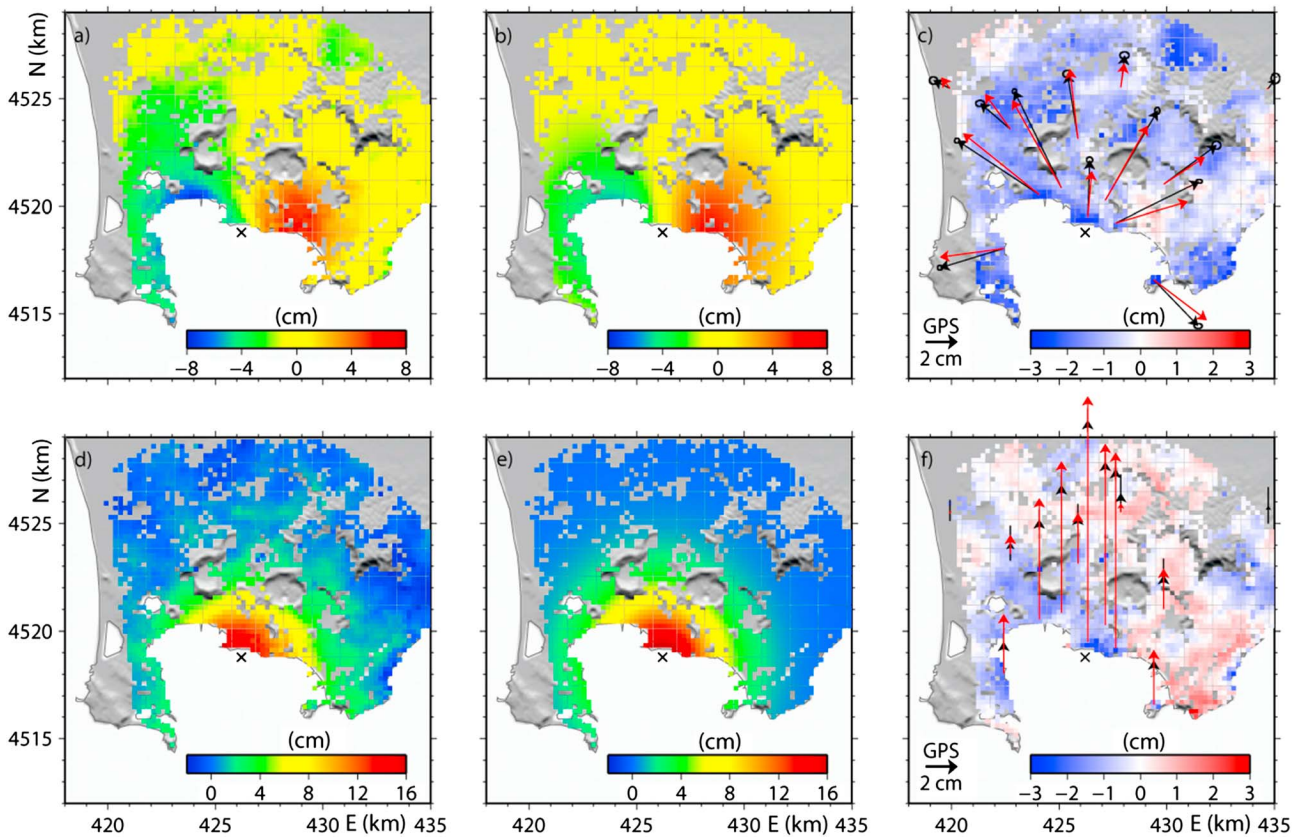


Figure 2.10 [2]: Comparison between observed ((a) E-W and (d) vertical) and computed ((b) E-W and (e) vertical) CSK data during 2011–2013. (c) E-W and (f) vertical displacement residuals. Observed (black) and computed (red) GPS are reported in Figure 4c, horizontal and Figure 4f, vertical components. The cross is the source center projection.

## 2.4 SUBSIDENCE IN THE CASSINO PLAIN

During the Second World War, Cassino was theatre of a long lasting battle and was completely destroyed. Since then the city has been rebuilt and the population has increased from about twenty to forty thousand people (Figure 2.11).

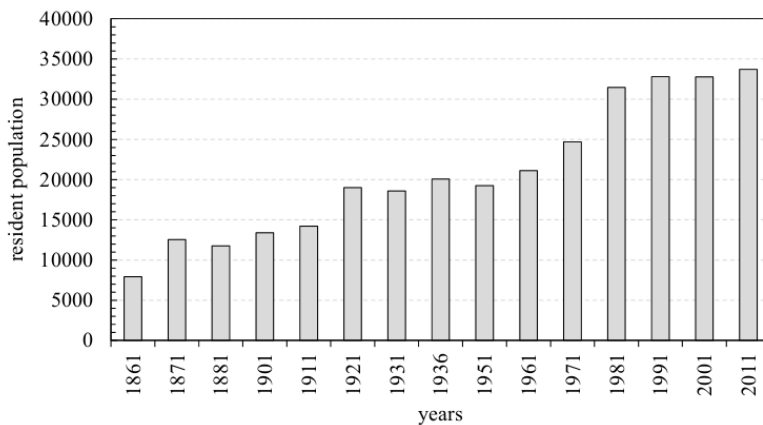


Figure 2.11 [3]: Demographic growth of the population residing in the town of Cassino.

Over this period, the urban area has considerably expanded in an alluvial plain at the foot of the Montecassino Abbey, in a peripheral sector of the central Apennines on the left side of the Latina Valley, among the Cairo Mt. (NW), Venafrò Mts. (NE) and Aurunci Mts. (S).

The area is represented by a Quaternary intermontane basin [35] bounded by Mesozoic-Cenozoic carbonatic reliefs. As well described in literature [36][37], stratigraphic succession points out the presence of dolostone and limestone with an age between Lias and lower Tortonian. Moving towards, sandstone with marls and gray clays interbedded represent the syn-orogenic sequence of the upper Tortonian foredeep [38]. Then, the deposition of sand and gravel banks (i.e., piggy-back deposits) scans the chain-progress system by diachronic stages, between lower Messinian and lower Pliocene [39][40]. Along the Latina Valley, thrust-tectonics and late Quaternary faults generated a passage from an epi-continental environment to a lacustrine one, aided by the obstruction role played by the Roccamonfina volcano. From middle Pleistocene to upper Pleistocene, lacustrine sandy silts and silty clays with rare volcanic levels characterize the lowland sectors of the Cassino area [41]. Generated by a mixing between mineral and shallow waters, travertine plateaus upwards close the lacustrine series.

Thus, alluvial deposits mark the passage towards current environmental conditions, characterized by the presence of coarse and fine-grained materials, mostly loose and/or normal consolidated. The localization and spatial distribution of the described units are shown in Figure 2.12.

The structural setting of the plain is characterized by extensional features, superposed on a fold and thrust geometry related to the contractional phases. The main element is the active fault Atina-San Pietro Infine [35][42-44], which shows tectonic evidences since the Lias age [45]. The NW-SE and NE-SW ones (Figure 2.12) are the prevailing fault with normal features and a horst and graben geometry. The Terme Varroniane and Borgo Mastronardi carbonatic outcrops (Figure 2.12) can be considered two horsts of the above-mentioned system. Nonetheless, additional buried horsts [35] have been detected under the quaternary deposits, portraying a complex trend of the bedrock (i.e., sandstone and limestone). On the other hand, the western boundary has a NNE-SSW trend with a complex geometry with the prevalence of contractional features. After a detailed geological analysis, it is supposed the presence of an anticline fold along the whole Montecassino-Cassino slope [35]. The analysis of the Quaternary thickness and the relationship between lacustrine deposits and the older units outline as the basin was most likely to be already established before the lacustrine event, in accordance with a horst and graben geometry. In fact, lacustrine deposits locally lay on the Mesozoic-Cenozoic limestone, upper Tortonian sandstone and piggy-back deposits, showing erosional events. However the sin-sedimentary action of the most tectonic elements (e.g., Atina-San Pietro fault), it is demonstrated by the huge variation of lacustrine thickness, ranging

from few meters to more than 140 m [19].

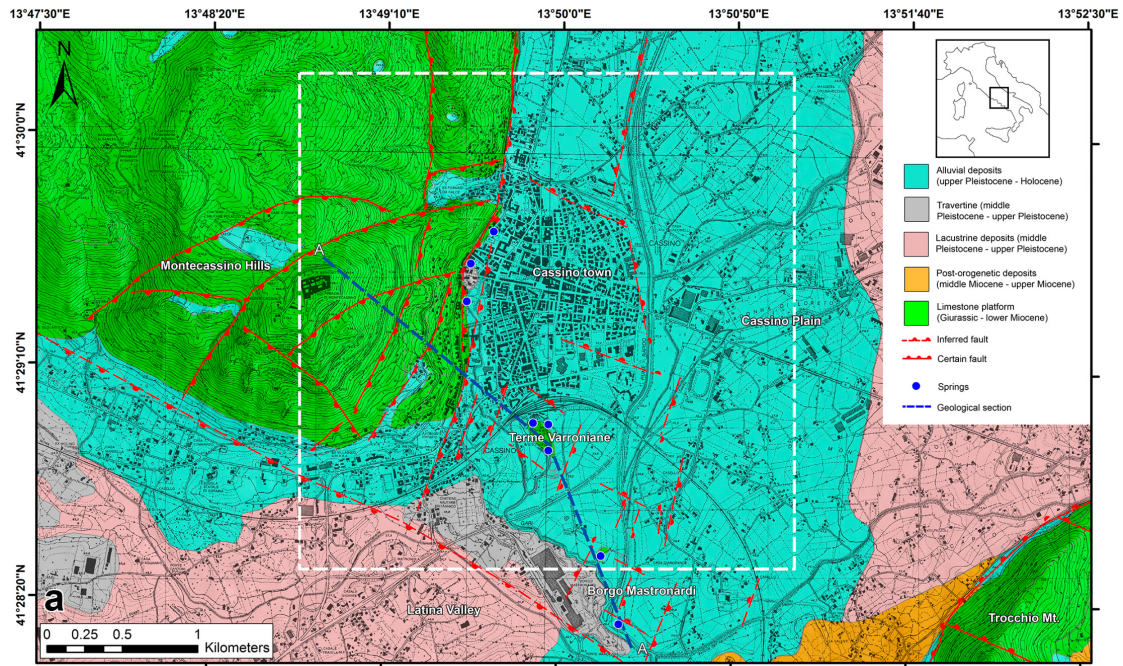


Figure 2.12 [3]: Geological map of the Cassino plain, the white box identifies the investigated area

From the geotechnical point of view, the deposits filling the basin are formed by lacustrine (fine grained) and fluvial (coarse grained) materials. The lacustrine fine-grained deposits appear as normalconsolidated, or slightly overconsolidated, with high values of the compressibility index. The fluvial coarse-grained soil consists of rounded particles, transported from the surrounding mountains by the rivers and deposited in the valley as debris fans. They appear as loose or slightly packed [46].

Finally, hydrogeological data are useful to support the geological model proposed. Gari springs (discharges of 13–15 m<sup>3</sup>/s) are scattered through the urban area of Cassino [47], by several springs and linear contributions along the Gari River. Highly permeable for karst, limestone represents the main hydrogeological reservoir, as well as sandstone, can be considered the regional aquiclude. Gari springs distribution and the discharge analysis ensures the continuity of the carbonatic structure and fit with the horst and graben model proposed before. In this context laterally fed by the main karst reservoir, the lacustrine and alluvial deposits represent a multi-stratified aquifer. Therefore, aquifers show a water level nearly coincident with the ground level.

#### 2.4.1 INSAR OBSERVATIONS

The InSAR data used for the long time analysis are provided by ERS 1-2 and Envisat satellite.

The ERS 1-2 dataset is composed of 45 SAR images acquired from April 1992 to September 2000 along descending orbit. The data processing was performed by the SBAS algorithm [48]

implemented in the ENVI SARscape software.

First, the images were been multi-looked by a factor of 4 in range and 20 in azimuth direction, respectively. Smoothed data with lower noise (speckle) level and a square pixel (spatial resolution of  $\sim 80 \times 80$  m) were obtained representing a good starting point for the interferometric SAR processing. The DInSAR processing has generated 124 interferograms, based on the following constraints: maximum spatial perpendicular baseline and maximum temporal baseline fixed to 400 m and 1500 days, respectively.

The topographic phase component was removed using the 90 m Digital Elevation Model (DEM) provided by the Shuttle Radar Topography Mission (SRTM).

The second dataset consists of 33 Envisat SAR images spanning from October 2004 to August 2010. They were also acquired along descending orbit with an incidence angle of  $23^\circ$  and an orbit inclination with respect to the geographic north equal to  $-167^\circ$ .

In this case the multi baseline approach [49] proposed in the framework of the IPTA technique [28] and implemented in GAMMA software packages was used. Envisat SAR data are characterized by a spatial resolution of about 20 m in range and 4 m in azimuth and ground coverage of about  $100 \times 100$  kilometers. All the images were preliminary cut around the Cassino plain and then multilook factors of 2 and 10 (in range and azimuth direction respectively) were applied in order to achieve a pixel size equal to  $40 \times 40$  m in both directions.

The maximum perpendicular spatial baseline was set to 400 m while the temporal baseline is between 1 and 350 days, with more than 90 interferograms. Although some of them were discarded due to large decorrelated and noisy areas (probably due to the large vegetated areas in Central Italy), or atmospheric residuals and unwrapping problems, a consistent number of interferograms were used for the study. Additionally, for Envisat data, SRTM DEM was used to remove the topographic phase. As stated above, fast ground changes hamper the possibility to study a specific area by means of DInSAR, being very sensitive to temporal decorrelation effects. In addition, in order to overcome or reduce this problem, the Goldstein filter [18] was applied, and high coherence and intensity thresholds (0.5 and 1.8, respectively) were used to select the points where estimating the displacement time series following the multi-baseline IPTA approach [49].

Such approach returned almost 5000 points like PS [50][51] clearly concentrated in the urbanized areas in the Cassino plain.

The results in terms of surface velocity rate and displacement time series were retrieved from both datasets. The Line-of-Sight (LOS) velocity rate shows a quite stable behavior in the southern part of the city (displacements close to zero), whereas it is possible to note a subsidence rate growing from the center of the plain to the northern side (Figure 2.13).

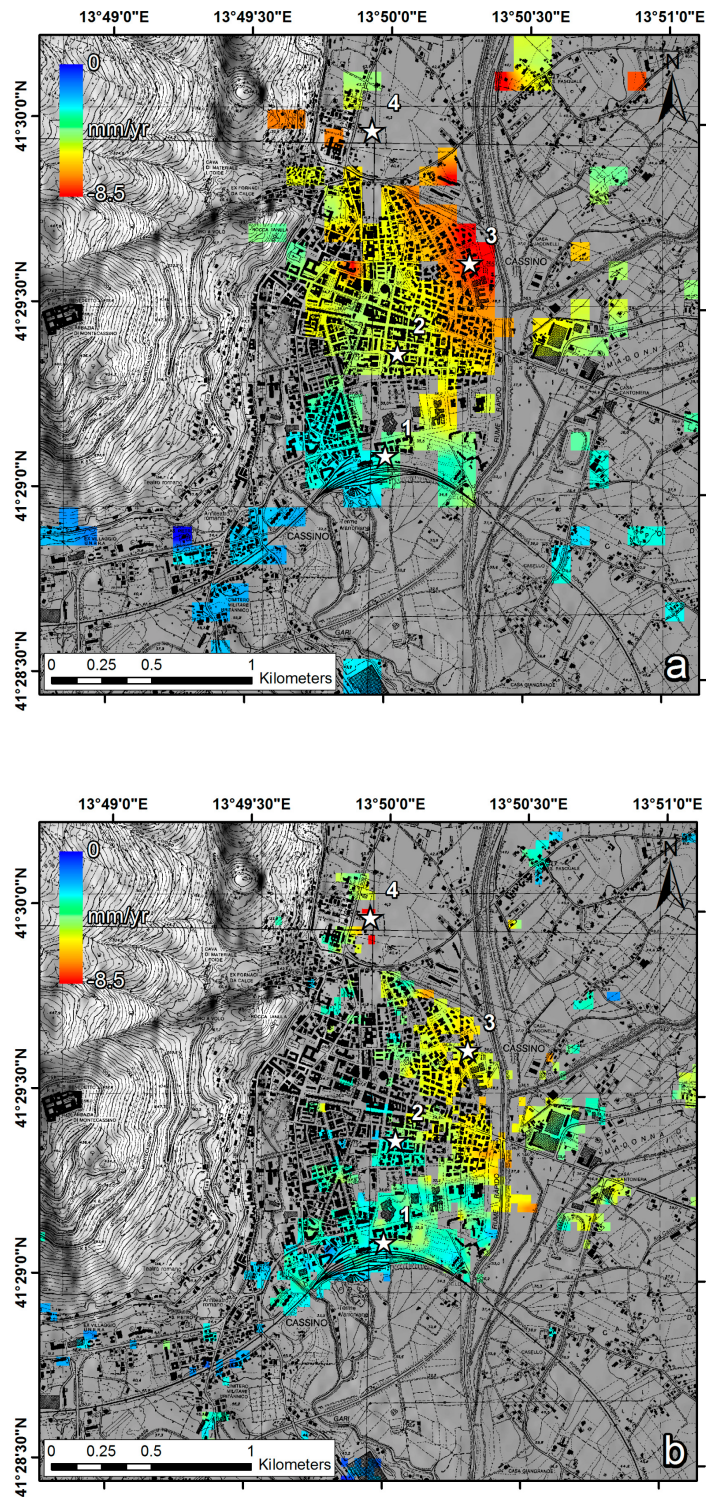


Figure 2.13 [3]: Plot of the 1992–2000 ERS 1-2 (up) and 2004–2010 Envisat (down) velocity maps. The white stars indicate the points whose time series are shown in Figure 2.14.

Despite the similar deformation pattern, the comparison of the 1992–2000 ERS 1-2 data series (Figure 3a) with the younger 2004–2010 Envisat data (Figure 3b) highlights that the subsidence rate slows down from about 5–6 mm/yr ( $\pm 1$  mm) to about 2.5 mm/yr ( $\pm 1$  mm) in the area where the

larger subsidence is detected (NE of the urban area). Similar trends are also observed in the other more stable areas.

This behavior is confirmed by the time series of cumulated LOS deformation for some target points, located in the southern (point 1), central (point 2) and northern (point 3) part of the investigated area (Figure 2.14).

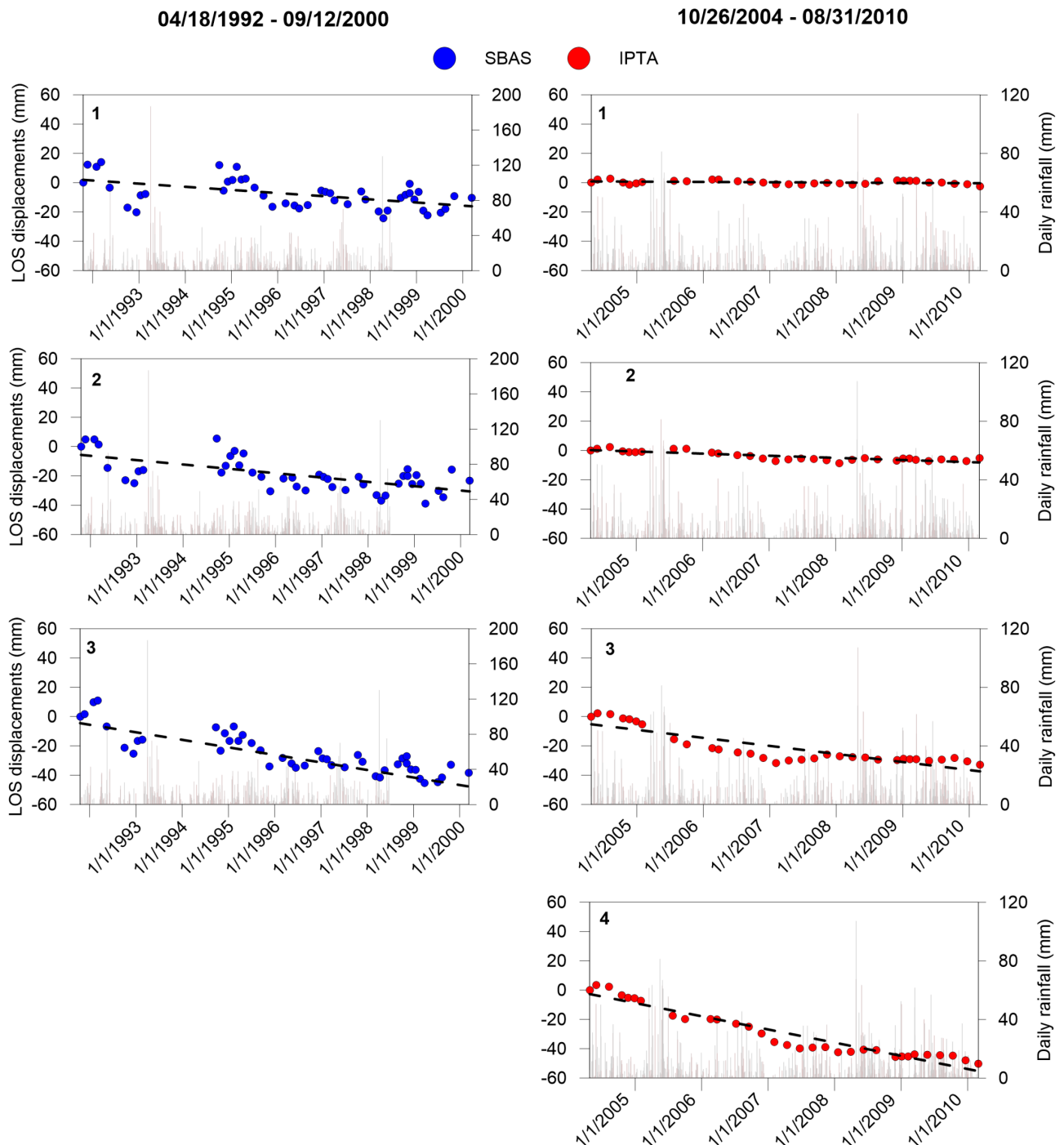


Figure 2.14 [3]: Time series relative to the targets identified in Figure 2.13, together with the daily rainfall registered in the Cassino municipality in the same observation period.

The ERS 1-2 (1992–2000) time series (Figure 2.14) show a seasonal deformation due to the oscillation of the groundwater table during the dry and rainy season, as observed by the comparison with rainfall data [52].

Instead, the Envisat time series (2004–2010) appear more smoothed since they were estimated using a weighting factor of 2 to reduce the slight oscillations around the linear trend. However, neglecting the seasonal effects it is possible to observe and compare a linear deformation trend for all points. The total subsidence increases moving from south (point 1) to north (point 3) of the plain. The point 1 appears stable in both datasets whereas the points 2 and 3 subside in a more accentuated way considering the ERS 1-2 data than Envisat data, clearly indicating a slowing down of the subsidence for the two investigated time span.

#### **2.4.2 THE JOINT EFFECT OF NATURAL AND ANTHROPOGENIC FACTORS**

The observed subsidence is strictly related to the presence of the soft soils constituting the alluvial valley of Cassino plain. The recent alluvial deposits are the most susceptible to settle because of the superimposition of different loads related to the urbanization such as man-made fills, infrastructures (e.g., road embankments, railways, aqueducts), buildings [53], and, finally, the lowering of water table level due to the overexploitation of the aquifer [54].

In the present case, the detected deformation cannot be ascribable to the lowering of the water table induced by groundwater exploitation. Indeed, most of the water wells are located to the south of the urban center, capturing water from the deep aquifer and the springs have not suffered flow reductions in the last 20 years. Furthermore, groundwater overexploitation generally produces higher values of subsidence rate, in the order of several centimeters per year [54][55].

Therefore, the urban development of Cassino in the last century has been taken into account in order to explain the observed phenomenon.

As observed in Figure 2.15, most of the buildings constituting the urban center have been built between the 1950s and 1990s, after the Second World War. Probably the greatest urban sprawl happened during the 1970s–1980s, according to the population growth (Figure 2.11), about 10–30 years before the observation periods of ERS 1-2 and Envisat data.

Generally, such external loads produce settlements, which can be considered as the combination of primary consolidation processes and secondary compression, in agreement with the consolidation theory [56]. The settlements ascribable to the primary consolidation process are largely greater than those ones due to the secondary compression, the last ones being strictly related to viscous behavior of very fine-grained soils and, especially, of organic soils. Generally the magnitude and the time needed to complete the primary consolidation process depends on the thickness and compressibility

of the loaded soils, on the hydraulic conductivity and on drainage condition and paths, being in some cases (i.e., thick layer of a very low permeability deposits involved in 1D consolidation process) very long such as some tens of years.

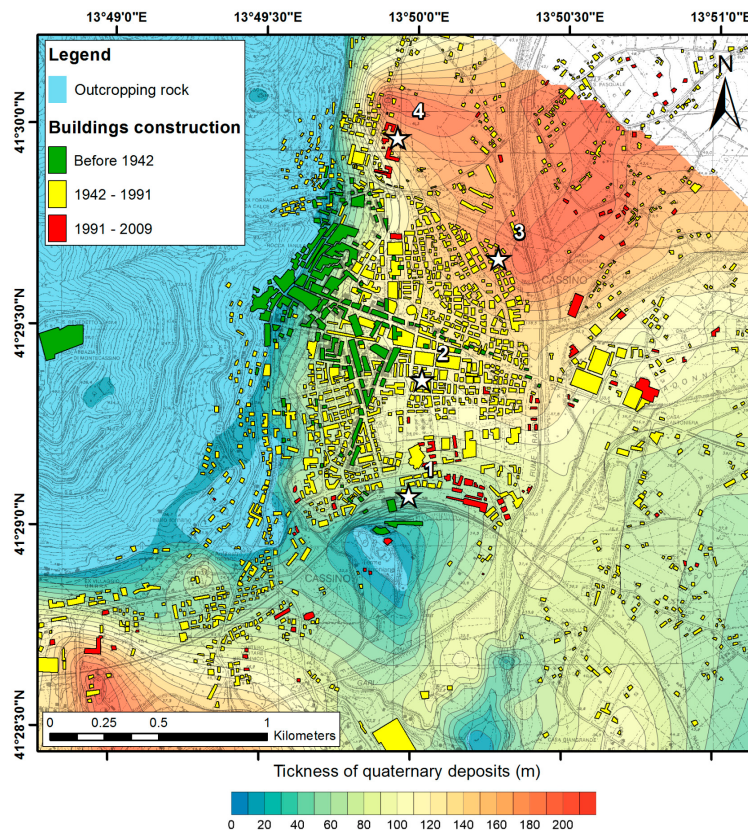


Figure 2.15 [3]: Contour map of the thickness of quaternary soft deposits filling the Cassino plain [19,38] together with the chronological development of the city.

According to the geotechnical characteristics of the soils [46], the relatively fast decreasing trend observed by the comparison of DInSAR time series referring to 1992–2000 and 2004–2010 (Figure 2.14) suggests that an exponentially decreasing subsidence affects the alluvial deposits mainly due to the urbanization and the construction of buildings.

Regarding the subsidence pattern observed in Figure 2.13, it is a clear consequence of the different thickness and lithology characterizing the soft alluvial deposits filling the Cassino basin. As a matter of fact, observing the contour map of the alluvial sediment thickness in Figure 2.15 [19,38], stable areas are located where the thickness of the alluvial deposits is smaller (point 1) as a direct consequence of the shorter time required to complete the consolidation process.

A further validation of the urbanization-induced subsidence is given by observing in the Envisat velocity map the occurrence of high rate of subsidence close to 9 mm/yr ( $\pm 1$  mm) north of the city center (point 4 in Figure 2.13), than to the smaller values (1–2 mm/yr  $\pm 1$  mm) detected in the

surrounding areas. The observed isolated case occurs on recent, four-storey residential buildings, constructed in the last 10–15 years, as it is easy to infer observing the 2000 and 2009 digital orthophoto in Figure 2.16a,b, where the buildings are present only in the 2009 image. Time series of the detected displacement in the area, i.e. point 4 in Figures 2.13 and 2.16, is shown in Figure 2.14 and reveal a total LOS displacement of about six centimeters in six years probably due to the ongoing consolidation process.

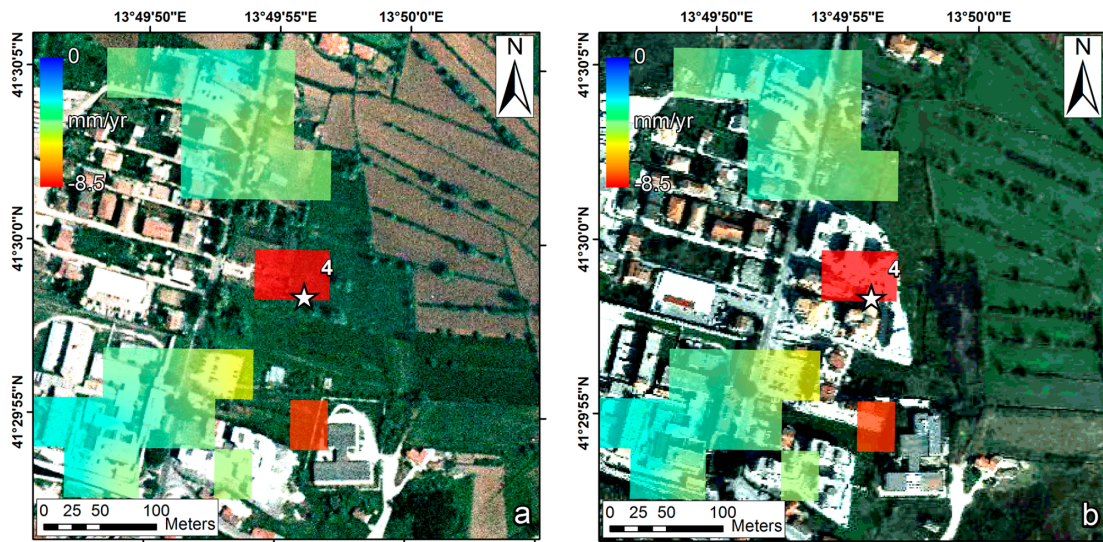


Figure 2.16 [3]: Envisat 2004–2010 velocity map superimposed to the 2000 (a) and 2009 (b) digital orthophoto

## REFERENCES

- [1] Stramondo, S.; Vannoli, P.; Cannelli, V.; Polcari, M.; Melini, D.; Samsonov, S.; Moro, M.; Bignami, C.; Saroli, M. X and C-band SAR surface displacement for the 2013 Lunigiana earthquake (Northern Italy): a breached relay ramp? *IEEE J. Sel. Top. Appl. Earth Obs. Remote Sens.* 2014, doi:10.1109/JSTARS.2014.2313640.
- [2] Trasatti E., Polcari M., Bonafede M., Stramondo S. (2015) - Geodetic constraints to the source mechanism of the 2011-2013 unrest at Campi Flegrei (Italy) caldera. *Geophysical Research Letters*, 42, doi: 10.1002/2015GL063621.
- [3] Polcari M., Albano M., Saroli M., Tolomei C., Lancia M., Moro M., Stramondo S. (2014) - Subsidence detected by multi-pass Differential SAR Interferometry in the Cassino plain (Central Italy): joint effect of geological and anthropogenic factors?. *Remote Sensing Journal*, vol. 6, 9676-9690; doi: 10.3390/rs6109676.
- [4] ISIDE Working Group. (2013). Italian Seismological Instrumental and Parametric Database [Online]. Available: <http://iside.rm.ingv.it>.
- [5] E. Guidoboni, G. Ferrari, D. Mariotti, A. Comastri, G. Tarabusi, and G. Valensise, CFTI4Med,

Catalogue of Strong Earthquakes in Italy (461 B.C.-1997) and Mediterranean Area (760 B.C.-1500). INGV-SGA, 2007, <http://storing.ingv.it/cfti4med/>.

[6] A. Rovida, R. Camassi, P. Gasperini, and M. Stucchi, Eds. CPTI11, the 2011 Version of the Parametric Catalogue of Italian Earthquakes. Milano, Bologna, 2011, <http://emidius.mi.ingv.it/CPTI>, doi: 10.6092/INGV.IT-CPTI11.

[7] A. Frepoli and A. Amato, “Contemporaneous extension and compression in the northern Apennines from earthquake fault-plane solutions,” *Geophys.J. Int.*, vol. 129, pp. 368–388, 1997.

[8] A. Tertulliani and A. Maramai, “Macroseismic evidences and site effects for the Lunigiana (Italy) 1995 earthquake,” *J. Seismol.*, vol. 2, pp. 209–222, 1998.

[9] B. Castello, G. Selvaggi, C. Chiarabba, and A. Amato, *CSI Catalogo della sismicità italiana 1981–2002, versione 1.1*. Roma: INGV-CNT, 2006, <http://csi.rm.ingv.it/>.

[10] P. Boncio, F. Brozzetti, and G. Lavecchia, “Architecture and seismotectonics of a regional low-angle normal fault zone in Central Italy”, *Tectonics*, vol. 19, pp. 1038–1055, 2000.

[11] A. Argnani, G. Barbacini, M. Bernini, F. Camurri, M. Ghielmi, G. Papani, F. Rizzini, S. Rogledi, and L. Torelli, “Gravity tectonics driven by Quaternary uplift in the Northern Apennines: insights from the La Spezia-Reggio Emilia geo-transect”, *Quatern. Int.*, vol. 101–102, pp. 13–26, 2003.

[12] R. Basili, G. Valensise, P. Vannoli, P. Burrato, U. Fracassi, S. Mariano, M. M. Tiberti, and E. Boschi, “The database of individual seismogenic sources (DISS), version 3: summarizing 20 years of research on Italy’s earthquake geology”, *Tectonophysics*, vol. 453, no. 1–4, pp. 20–43, 2008, doi: 10.1016/j.tecto.2007.04.014.

[13] DISS Working Group. (2010). Database of Individual Seismogenic Sources (DISS), Version 3.1.1: A Compilation of Potential Sources for Earthquakes Larger than M 5.5 in Italy and Surrounding Areas [Online]. Available: <http://diss.rm.ingv.it/diss/>, doi: 10.6092/INGV.IT-DISS3.1.1.

[14] M. Bernini and G. Papani, “La distensione della fossa tettonica della Lunigiana nord-occidentale,” *Boll. Soc. Geol. Ital.*, vol. 121, pp. 313–341, 2002.

[15] D. Di Naccio, P. Boncio, F. Brozzetti, F. J. Pazzaglia, and G. Lavecchia, “Morphotectonic analysis of the Lunigiana and Garfagnana grabens (northern Apennines, Italy): Implications for active normal faulting,” *Geomorphology*, vol. 201, pp. 293–311, 2013.

[16] F. Covello, F. Battazza, A. Coletta, E. Lopinto, C. Florentino, L. Pietranera, G. Valentini, and S. Zoffoli, “CSK an existing opportunity for observing the Earth,” *J. Geodynam.*, vol. 49, pp. 171–180, 2010.

[17] U. Wegmuller and C. Werner, “Gamma SAR processor and interferometry software”, *IEEE Geoscience and Remote Symposium, IGARSS, Florence, Italy*, 1997.

[18] R. Goldstein and C. Werner, “Radar interferogram filtering for geophysical applications,” *Geophys. Res. Lett.*, vol. 25, no. 21, pp. 4035–4038, 1998

- [19] M. Costantini, “A novel phase unwrapping method based on network programming,” *IEEE Trans. Geosci. Remote Sens.*, vol. 36, no. 3, pp. 813–821, 1998.
- [20] Y. Okada, “Internal deformation due to shear and tensile faults in a half space,” *Bull. Seismol. Soc. Am.*, vol. 82, pp. 1018–1040, 1992.
- [21] R. Hanssen, *Radar Interferometry: Data Interpretation and Error Analysis*. New York, NY, USA: Springer-Verlag, 2001.
- [22] S. Kirkpatrick, C. D. Gelatt, and M. P. Vecchi, “Optimization by simulated annealing,” *Science*, vol. 220, no. 4598, pp. 671–680, May 1983.
- [23] K. L. Feigl, “Estimating earthquake source parameters from geodetic measurements,” in *International Handbook of Earthquake and Engineering Seismology*, vol. 81A, 2002, pp. 607–620.
- [24] R. L. Gawthorpe and J. M. Hurst, “Transfer zones in extensional basins; their structural styles and influence in drainage development and stratigraphy,” *J. Geol. Soc.*, vol. 150, pp. 1137–1152, 1993.
- [25] Rosi, M., A. Sbrana, and C. Principe (1983), The Phlegraean Fields; structural evolution, volcanic history and eruptive mechanisms, *J. Volcanol. Geotherm. Res.*, 17, 273–288.
- [26] De Martino, P., U. Tammaro, and F. Obrizzo (2014), GPS time series at Campi Flegrei caldera (2000–2013), *Ann. Geophys.*, 57(2), S0213, doi:10.4401/ag-6431.
- [27] Chiodini, G., S. Caliro, P. De Martino, R. Avino, and F. Gherardi (2012), Early signals of new volcanic unrest at Campi Flegrei caldera? Insights from geochemical data and physical simulations, *Geology*, 40, 943–946, doi:10.1130/G33251.1.
- [28] Werner, C., U. Wegmüller, T. Strozzi, and A. Wiesmann (2003), Interferometric point target analysis for deformation mapping, *Geosci. Remote Sens. Symp.*, 7, 4362–4364, doi:10.1109/IGARSS.2003.1295516.
- [29] Amoruso, A., L. Crescentini, and I. Sabetta (2014a), Paired deformation sources of the Campi Flegrei caldera (Italy) required by recent (1980–2010) deformation history, *J. Geophys. Res. Solid Earth*, 119, 858–879, doi:10.1002/2013JB010392.
- [30] Chiarabba, C., and M. Moretti (2006), An insight into the unrest phenomena at the Campi Flegrei caldera from Vp and Vp/Vs tomography, *Terra Nova*, 18, 373–379, doi:10.1111/j.1365-3121.2006.00701.x.
- [31] Zollo, A., N. Maercklin, M. Vassallo, D. Dello Iacono, J. Virieux, and P. Gasparini (2008), Seismic reflections reveal a massive melt layer feeding Campi Flegrei caldera, *Geophys. Res. Lett.*, 35, L12306, doi:10.1029/2008GL034242.
- [32] Trasatti, E., M. Bonafede, C. Ferrari, C. Giunchi, and G. Berrino (2011), On deformation sources in volcanic areas: Modeling the Campi Flegrei (Italy) 1982–84 unrest, *Earth Plan. Sci. Lett.*, 306, 175–185, doi:10.1016/j.epsl.2011.03.033.

- [33] Sambridge, M. (1999a), Geophysical inversion with a neighbourhood algorithm—I. Searching a parameter space, *Geophys. J. Int.*, 138(2), 479–494.
- [34] Sambridge, M. (1999b), Geophysical inversion with a neighbourhood algorithm—II. Appraising the ensemble, *Geophys. J. Int.*, 138(3), 727–746.
- [35] Saroli, M.; Lancia, M.; Albano, M.; Modoni, G.; Moro, M.; Scarascia Mugnozza, G. New geological data on the Cassino intermontane basin, central Apennines, Italy. *Rend. Lincei* 2014, doi:10.1007/s12210-014-0338-5.
- [36] Accordi, B.; Angelucci, A.; Sirna, G. Note Illustrative Della Carta Geologica D'ITALIA alla Scala 1:100.000 Fogli 159 e 160 Frosinone e Cassino; Servizio Geologico Italiano: Roma, Italy, 1967.
- [37] Corda, L.; Brandano, M. Aphotic zone carbonate production on a Miocene ramp, Central Apennines, Italy. *Sediment. Geol.* 2003, 161, 55–70.
- [38] Cipollari, P.; Cosentino, D. Miocene unconformities in the Central Apennines: Geodynamic significance and sedimentary basin evolution. *Tectonophysics* 1995, 252, 375–389.
- [39] Centamore, E.; di Manna, P.; Rossi, D. Kinematic evolution of the Volsci Range: A new overview. *Boll. Soc. Geol. Ital.* 2007, 126, 159–172.
- [40] Pasquali, V.; Castorina, F.; Cipollari, P.; Cosentino, D.; Lo Mastro, S. I depositi tardo-orogenici della Valle Latina meridionale: Stratigrafia e implicazioni cinematiche per l'evoluzione dell'Appennino Centrale. *Boll. Soc. Geol. Ital.* 2007, 126, 101–118.
- [41] Devoto, G. Lacustrine Pleistocene in the lower Liri Valley. *Geol. Romana* 1965, 4, 291–368.
- [42] Bosi, V. Evidenze di attività Tettonica durante il Pleistocene Medio–Olocene nel Lazio sud-orientale ed aree attigue. *Pubbl. Ist. Naz. Geof. Roma* 1995, 564, 1–32.
- [43] Barchi, M.; Galadini, F.; Lavecchia, G.; Messina, P.; Michetti, A.M.; Peruzza, L.; Pizzi, A.; Tondi, E.; Vittori, E. Sintesi delle Conoscenze Sulle Faglie Attive in Italia Centrale; CNR Gruppo Nazionale Difesa Terremoti: Roma, Italy, 2000.
- [44] Roberts, P.G.; Michetti, A.M.; Cowie, P.; Morewood, N.C.; Papanikolaou, I. Fault slip-rate variations during crustal-scale strain localization, central Italy. *Geophys. Res. Lett.* 2002, doi:10.1029/2001GL013529.
- [45] Cavinato, G.P.; Sirna, M. Elementi di tettonica transpressiva lungo la linea di Atina (Lazio Meridionale). *Mem. Soc. Geol. Ital.* 1988, 41, 1179–1190.
- [46] Modoni, G.; Saroli, M.; Darini, G. Characterization at urban scale of the subsoil of Cassino. In *Proceedings of the XIV European Conference on Soil Mechanics and Geotechnical Engineering ECSMGE, Madrid, Spain, 24–27 September 2007*; pp. 1727–1732.
- [47] Boni, C.F.; Bono, P.; Capelli, G. Schema Idrogeologico dell'Italia Centrale. Carta Idrogeologica, C. Idrologica, C. dei Bilanci Idrogeologici, Scala 1:500000. *Mem. Ital. Geol. Soc. (Ital.)* 1986, 35, 991–1012.

- [48] Berardino, P.; Fornaro, G.; Lanari, R.; Sansosti, E. A new algorithm for surface deformation monitoring based on small baseline differential SAR interferograms. *IEEE Trans. Geosci. Remote Sens.* 2002, 40, 2375–2383.
- [49] Werner, C.; Strozzi, T.; Wegmuller, U. Deformation time-series of the lost-hills oil field using a multi-baseline interferometric SAR inversion algorithm with finite difference smoothing constraints. In *Proceedings of AGU Fall Meeting, San Francisco, CA, USA, 3–7 December 2012*.
- [50] Ferretti, A.; Prati, C.; Rocca, F. Nonlinear subsidence rate estimation using permanent scatterers in differential SAR interferometry. *IEEE Trans. Geosci. Remote Sens.* 2000, 38, 2202–2212.
- [51] Ferretti, A.; Prati, C.; Rocca, F. Permanent scatterers in SAR interferometry. *IEEE Trans. Geosci. Remote Sens.* 2001, 39, 8–20.15,16.
- [52] Ufficio Idrografico e Mareografico di Roma. Available online: <http://www.idrografico.roma.it/default.aspx> (accessed on 24 April 2014).
- [53] Stramondo, S.; Bozzano, F.; Marra, F.; Wegmuller, U.; Cinti, F.R.; Moro, M.; Saroli, M. Subsidence induced by urbanization in the city of Rome detected by advanced InSAR technique and geotechnical investigations. *Remote Sens. Environ.* 2008, 112, 3160–3172.11.
- [54] Stramondo, S.; Saroli, M.; Tolomei, C.; Moro, M.; Doumaz, F.; Pesci, A.; Loddo, F.; Baldi, P.; Boschi, E. Surface movements in Bologna (Po Plain—Italy) detected by multitemporal DinSAR. *Remote Sens. Environ.* 2007, 110, 304–316.
- [55] Chaussard, E.; Wdowinski, S.; Cabral-Cano, E.; Amelung, F. Land subsidence in central Mexico detected by ALOS InSAR time-series. *Remote Sens. Environ.* 2014, 140, 94–106.
- [56] Terzaghi, K.; Peck, R.B. *Soil Mechanics in Engineering Practice*; John Wiley & Sons: Hoboken, NJ, USA, 1967.37.

---

*\*Some parts and figures of this chapter are reprinted, with permission, from IEEE Journal of Selected Topics in Applied Earth Observations and Remote Sensing ([1]), Geophysical and Research Letters ([2]) and Remote Sensing Journal ([3])*

# **CHAPTER 3: 3D DISPLACEMENT FIELD RETRIEVED BY INTEGRATING SENTINEL-1 INSAR AND GPS DATA: THE 2014 SOUTH NAPA EARTHQUAKE [1]**

## **3.1 INTRODUCTION**

The possibility of merging data provided by different geodetic techniques to retrieve the three dimensional (3D) components of a surface displacement field is widely debated in literature [2-5] and is still one of the most exciting challenges for the scientific “geodetic and remote sensing” community. Today, InSAR and GPS are two of the most important sources of information concerning the Earth’s topography and surface deformation that can be synergistically combined with LiDAR and optical data [6].

Moreover, InSAR and GPS data are fully complementary and suitable to be integrated in order to estimate an accurate 3D displacement field, with millimeter precision and large spatial coverage.

Indeed, InSAR data allow covering areas of hundreds of square kilometers with a spatial resolution ranging from a few meters to  $> 20$  m depending on the satellite and the acquisition mode.

In particular, InSAR measures the range distance between the Earth’s surface and the sensor along the satellite Line-of-Sight (LOS). Since the satellites usually acquire data with an incidence angle spanning about  $20^\circ - 30^\circ$ , the measured LOS displacement is particularly sensitive to the vertical displacement. Therefore, due to the viewing geometry, InSAR can better constrain deformation fields mainly characterized by a vertical component as is the case of subsidence [7][8] or volcanos inflation/deflation [8-11].

On the other hand, a permanent GPS station provides the estimation of absolute and continuous 3D site coordinates. Then, the key contribution with respect to the InSAR data is the time-continuous information. The main drawback is the relatively low spatial density of the GPS networks. Typically, the distance between stations belonging to the same network ranges from a few to tens of kilometers according to the wavelength of the signal to be monitored. Therefore, the information provided by GPS needs oftentimes to be interpolated; this process might lead to errors proportional to the distance among stations so that the entire signal is missing if it falls completely between stations.

The present study proposes an InSAR-GPS data integration [12] using the Sentinel-1 SAR data acquired at the time of occurrence (August 24<sup>th</sup>, 2014) of the Mw 6.0 South Napa earthquake. The epicenter of this earthquake was located within the western sector of the West Napa Fault system, a strike-slip crustal structure between the Rodger’s Creek and Green Valley faults, with nearly pure

NNW attitude [13].

Sentinel-1A was launched on April 3<sup>rd</sup> 2014, from the European Spaceport in French Guiana, representing the first of a constellation of two satellites (Sentinel-1A and Sentinel-1B). It carries an advanced C-band polar-orbiting radar providing all-weather and day-and-night images of Earth's surface. The revisit time is significantly improved with respect to those of the ERS 1-2 and Envisat satellites (6-12 vs 35-70 days).

In addition, the more common acquisition mode is the Interferometric Wide swath (IW) implementing a new type of ScanSAR called Terrain Observation with Progressive Scan (TOPS), which allows significantly extending the ground coverage with a 250 km swath at about 5 m range by 20 m azimuth spatial resolution.

The system is also able to acquire data in Stripmap mode and in Extra Wide (EW) swath mode allowing to improve the pixel resolution or the areal coverage, according to the scale of the studied phenomenon and the details required by the specific application.

All these improvements make Sentinel-1 an innovative tool for the Earth's surface observation. Therefore, the integration with increasingly dense GPS networks will play a key role in the study of natural phenomena at different spatial and temporal scales (e.g., faults motion, volcanic inflation/deflation, landmass subsidence, etc.).

### 3.2 INSAR-GPS INTEGRATION: THEORY

The method used for integrating InSAR and GPS data was originally proposed by Samsonov et al. [2006], and is based on a Bayesian statistical approach searching for the optimal estimation of the three deformation rate components.

The InSAR deformation rate estimated along the satellite LOS can be expressed as follows:

$$V_{LOS}^i = [v_x^i, v_y^i, v_z^i] [-\cos(\alpha)\sin(\theta), \sin(\alpha)\sin(\theta), \cos(\theta)]^T \quad (3.1)$$

where  $V_{LOS}^i$  is the InSAR LOS deformation rate defined on a grid of N points,  $[v_x^i, v_y^i, v_z^i]$  are the east, north and vertical unknown components of the deformation rate, and  $\theta$  and  $\alpha$  are the incidence and the azimuth angle of the satellite, respectively.

The GPS velocities are:

$$V^i = [V_x^i, V_y^i, V_z^i] \quad (3.2)$$

Since the velocities from (3.2) can be estimated only at sparse locations corresponding to the

available GPS sites, it is necessary to adopt an interpolation approach. In particular, in order to merge InSAR and GPS data, the GPS velocities need to be interpolated and resampled onto the InSAR grid points. To do so, the Kriging interpolation method is applied [14], while the most probable deformation rate components are searched by using the Bayes inference theory.

The Bayes theory is widely used in decision-making problems allowing the estimation of an unknown parameter or a random variable by observing another random variable and knowing the joint probability density distribution.

In particular, let  $a$  be an unknown parameter to be estimated and  $b$  the  $N$  observations of the random variable  $B$ .

In the Bayes estimation, the best performance (optimal estimation) is obtained when the estimate  $\hat{a}$  of the unknown parameter  $a$  is such to minimize the Bayes risk.

The Bayes risk of  $\hat{a}$  can be expressed as follows [15]:

$$R(\hat{a}) = \int_{a \in A} C(a, \hat{a}) P(a/b) da \quad (3.3)$$

where  $A$  is the space of the parameters,  $P(a/b)$  is the *a posteriori* distribution and  $C(a, \hat{a})$  is a cost function defined as:

$$C(a, \hat{a}) = \begin{cases} 0 & \text{if } \|\hat{a} - a\| \leq \delta \\ 1 & \text{otherwise} \end{cases} \quad (3.4)$$

where  $\delta$  is any small constant.

Then, equation (3.3) becomes:

$$R(\hat{a}) = \int_{a \in A} P(a/b) da = 1 - \int_{a: \|\hat{a} - a\| \leq \delta} P(a/b) da \quad (3.5)$$

As  $\delta \rightarrow 0$  the Bayes risk of the estimate  $\hat{a}$  can be rewritten as:

$$R(\hat{a}) \simeq 1 - P(a/b) \quad (3.6)$$

Therefore, minimizing the Bayes risk is equivalent to maximizing the *a posteriori* distribution that can be calculated by exploiting the Bayes theorem:

$$P(a/b) = \frac{P(b/a)P(a)}{P(b)} \propto P(b/a) \quad (3.7)$$

where  $P(a/b)$  is the likelihood of the observation  $b$ ,  $P(a)$  is the *a priori* density distribution and  $P(b)$  is the density of  $b$  that can be ignored since  $b$  is given.

In addition, in many application fields such as the image analysis, the *a priori* density distribution,  $P(a)$  is not used, being related to the reliability of the model developed for the estimation. Then, it will be neglected in the subsequent computations.

With these assumptions, the  $\hat{a}$  value minimizing the risk is the same as maximizing the likelihood, thus leading to the Maximum Likelihood Estimation (MLE).

As explained in details by Li [15], the likelihood can be estimated according to the Hammersley-Clifford theorem stating that any conditional distribution, under some conditions, has a distribution which is represented by a Gibbs function:

$$P(b/a) = \frac{1}{\prod_{i=1}^N \sqrt{2\pi\sigma_i^2}} e^{-U(b/a)} \quad (3.8)$$

where  $U(b/a)$  is the likelihood energy, defined as:

$$U(b/a) = \frac{\sum_{i=1}^N (b_i/a_i)^2}{2\sigma_i^2} \quad (3.9)$$

Here, a Gaussian noise was assumed since it is a special member of the Gibbs distribution family.

Equation (3.8) states that the likelihood is proportional to the function  $e^{-U(b/a)}$ , then the MLE of  $a$ , i.e.  $\hat{a}$ , is obtained in equivalent manner by minimizing the likelihood energy function in (3.9).

Therefore, the *a posteriori* distribution (3.7) can be expressed in terms of energy functions as follows:

$$U(a/b) \propto U(b/a) = \frac{\sum_{i=1}^N (b_i - a_i)^2}{2\sigma_i^2} \quad (3.10)$$

Finally, by applying (3.10) to the case of the InSAR-GPS measurements is possible to retrieve the MLE estimate of the three optimized deformation rate components:

$$U(v_x, v_y, v_z / V_{LOS}, V_x, V_y, V_z) = \sum_{i=1}^N \frac{1}{(2\sigma_{sar}^i)^2} (V_{LOS}^i + v_x \cos(\alpha) \cos(\theta) - v_y \sin(\alpha) - v_z \cos(\theta))^2 + \frac{1}{(2\sigma_{x_{gps}}^i)^2} (V_x^i - v_x^i)^2 + \frac{1}{(2\sigma_{y_{gps}}^i)^2} (V_y^i - v_y^i)^2 + \frac{1}{(2\sigma_{z_{gps}}^i)^2} (V_z^i - v_z^i)^2 \quad (3.11)$$

where:

- $N$  is the number of points of the InSAR and interpolated-GPS grid images
- $v_x, v_y, v_z$  are the three unknown components of the deformation rate, i.e. the unknown parameters  $a_i$  in (3.10)
- $V_{LOS}, V_x, V_y, V_z$  are the observations from InSAR and GPS respectively, i.e., the known parameters  $b_i$  in (3.10)
- $\frac{1}{2\sigma_{sar}^2}, \frac{1}{2\sigma_{x_{gps}}^2}, \frac{1}{2\sigma_{y_{gps}}^2}, \frac{1}{2\sigma_{z_{gps}}^2}$  are the standard deviations of the InSAR and GPS measurements, respectively

Therefore, the three components of the deformation rate for each point of the image are found by minimizing equation (3.11).

### 3.3 GEODETIC DATA

#### 3.3.1 INSAR DATA

The SAR data provided by Sentinel-1 were acquired in Stripmap mode with an incidence angle of about  $23^\circ$  and a pixel resolution of about 4 m in both directions covering an area of about  $70 \times 180$  Km<sup>2</sup>. A single pair of SAR images was exploited in order to detect and measure the co-seismic displacement caused by the earthquake. The pre- and post-earthquake images were acquired on August 7<sup>th</sup> 2014 and on August 31<sup>st</sup> 2014, respectively. The resulting image pair, characterized by a perpendicular baseline of 2 meters, was processed using the GAMMA software [16].

In order to focus on the epicentral area, the data have been cut and multi-looked by a factor of 15 in both range and azimuth to obtain a  $60 \times 60$  meters pixel. The SRTM Digital Elevation Model (DEM) has been used to remove the topographic phase. Moreover, the Minimum Cost Flow (MCF) algorithm [17] has been applied for phase unwrapping following a phase filtering [18]. As portrayed in Figure 3.1, the resulting differential interferogram shows interferometric fringes allowing the detection of a significant surface displacement caused by the earthquake.

#### 3.3.2 GPS DATA

The analyzed GPS dataset, covering the period August 1<sup>st</sup> 2014 - September 2<sup>nd</sup> 2014, includes 27 stations belonging to the Bay Area Regional Deformation Network (BARDN) and 115 additional continuous stations whose data are available in the UNAVCO and in the Crustal Dynamics Data Information System (CDDIS) archives. The GNSS raw observations were processed by means of the GAMIT/GLOBK 10.5 software (<http://www-gpsg.mit.edu>), using precise IGS orbits

(International GNSS Service; <http://igs.cb.jpl.nasa.gov>) and the IERS Earth orientation parameters (International Earth Rotation Service; <http://www.iers.org>). All stations have been organized and processed into three sub-networks, each one including about 50 stations and sharing a few common sites to provide the necessary ties between them. The results of this processing step are daily estimates of loosely constrained station coordinates, along with the associated variance-covariance matrices.

In a successive step, these loosely constrained daily solutions were used as quasi observations in a Kalman filtering (GLOBK) in order to estimate a consistent set of daily coordinates (i.e. time series) for all the sites involved. The resulting time series were aligned to a North America fixed reference frame [19]. A simple visual inspection of the coordinates time series of the stations located close to the epicentral area allowed to detect a significant offset ascribed to the co-seismic deformation (Fig. 3.3).

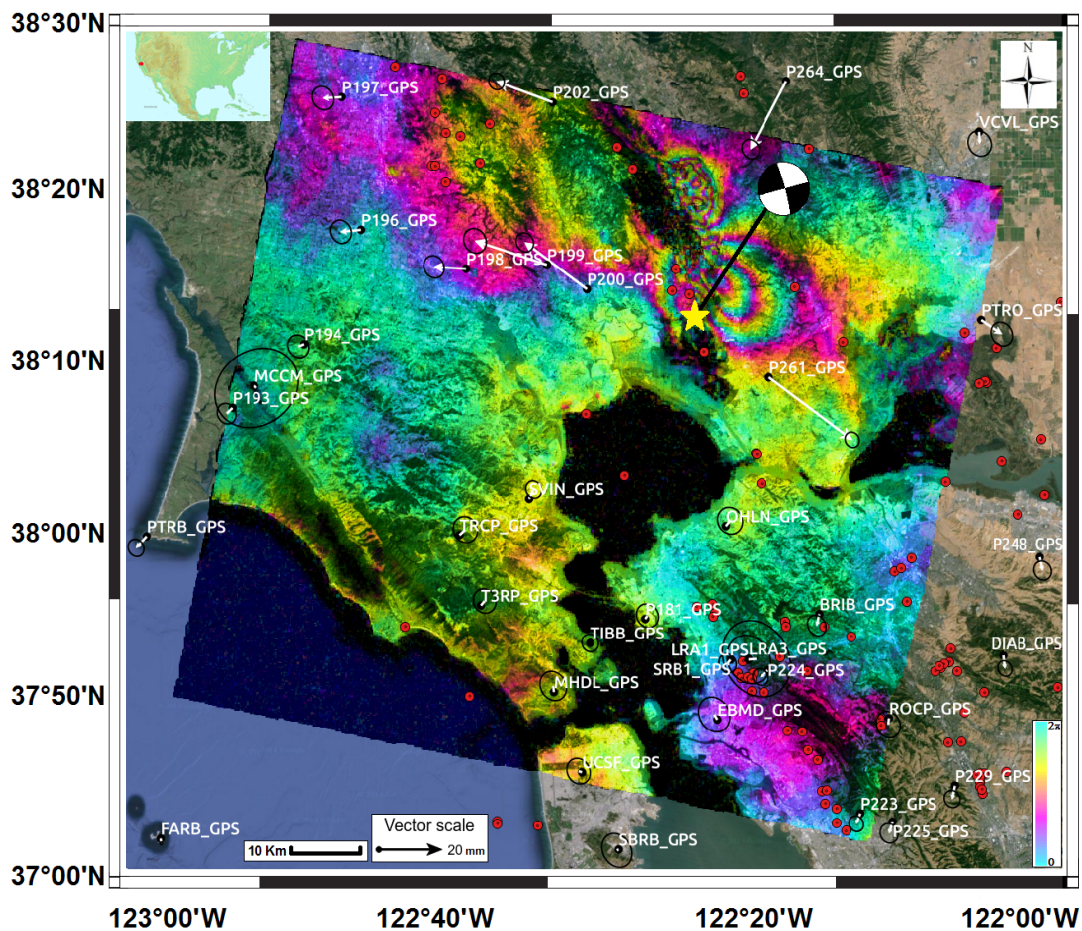
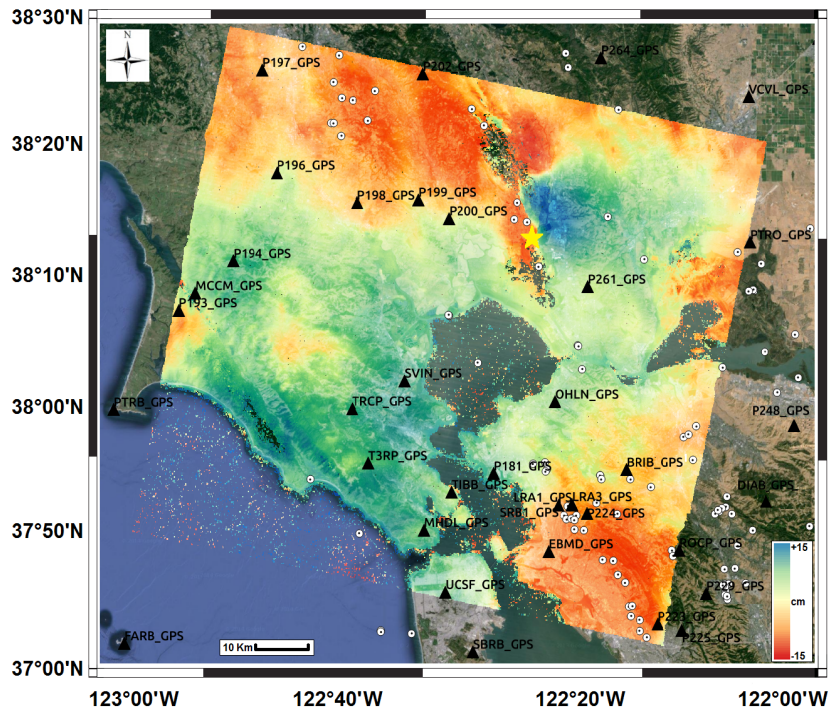


Figure 3.1 [1]: Wrapped interferogram showing co-seismic LOS displacement (each fringe corresponds to 2.8 cm). GPS sites with co-seismic displacement vectors are shown in white. GPS co-seismic displacement was estimated by differencing the average site positions over 2 days before and after the event. Yellow star indicate the Mw 6.0 epicenter location. Mw > 3.5 seismicity (red circles) and focal mechanism related to the Mw 6.0 earthquake are also reported (<http://earthquake.usgs.gov/earthquakes>).



(B)



(C)

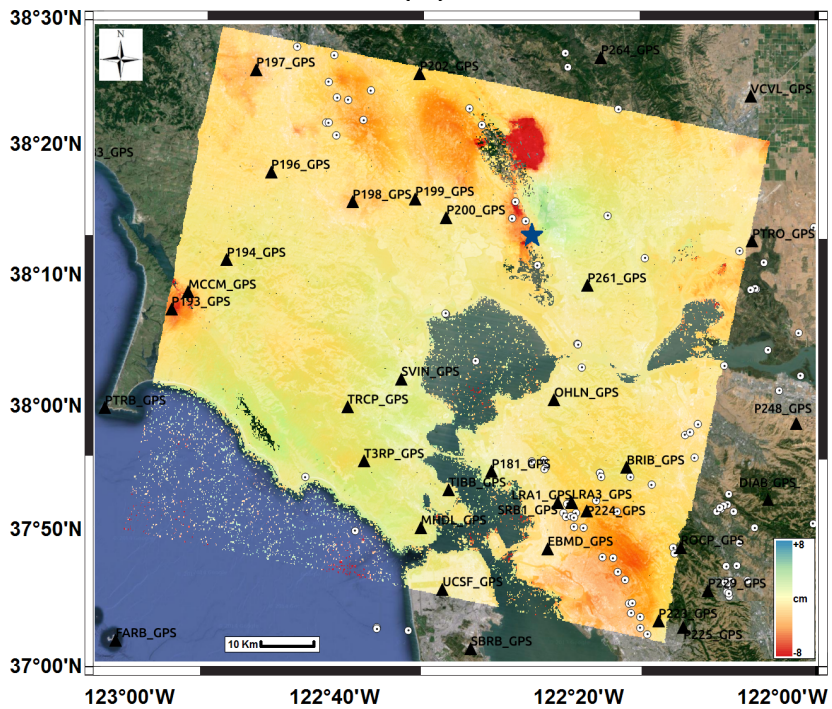


Fig. 3.2 [1]: 3D optimized components of surface displacement field caused by the earthquake. N-S component (A), E-W component (B) and U-D component (C). GPS sites are indicated with the black triangles. Star indicates the Mw 6.0 epicenter location. Mw>3.5 seismicity is also shown (<http://earthquake.usgs.gov/earthquakes>).

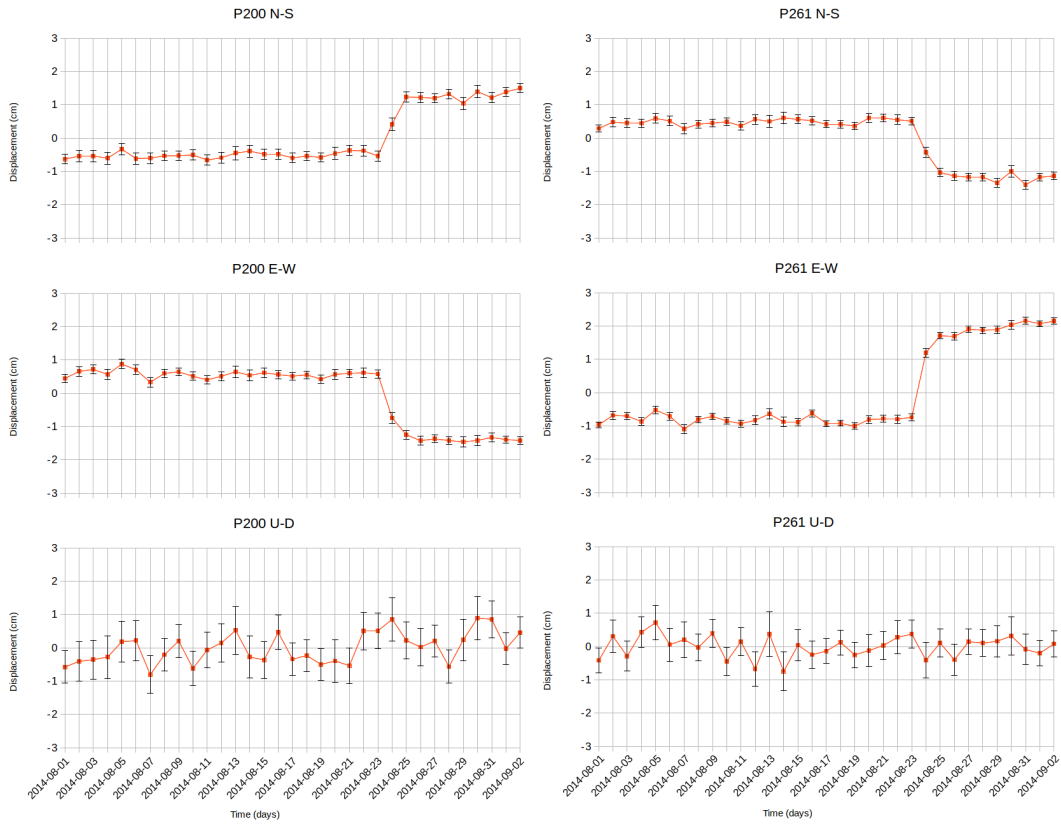


Fig.3.3 [1]: Time series of North-South (upper panel), East-West (central panel) and Up-Down (bottom panel) displacements of stations P200 (left side) and P261 (right side).

Particular care is required to explain the results at the NE side of the fault plane. Indeed, this area shows a minor S-ward motion E with respect to the SE side (Fig. 3.2-A), but it is also characterized by significant subsidence (Fig. 3.2-C). The lack of GPS stations results in a deformation mainly derived from the InSAR data that are not fully suitable in constraining the N-S component due to the orbital configuration. However, the deformation gradient is located close to the city of Napa, where field investigations by Hudnut et al., [20] revealed a strike rotation that might have led to the estimated pattern. Table 3.1 provides an evaluation of the performance of the adopted method. In particular, the standard deviation for a point close to the epicenter is shown. As expected, the north component does not show any major change since the InSAR data are less sensitive to the motion along that component. On the other hand, a significant improvement of the east and up components by the optimization step is clearly noticeable.

	$\sigma_{NS}$	$\sigma_{EW}$	$\sigma_{UD}$
<b>GPS</b>	<b>0.538</b>	<b>0.514</b>	<b>1.097</b>
<b>InSAR+GPS</b>	<b>0.531</b>	<b>0.427</b>	<b>0.596</b>

Table 3.1 [1]:  $\sigma$  (cm) of north, east and up components estimated before and after the optimization step for a point close the epicenter. Here GPS data are meant as the interpolated GPS data.

### 3.5 DISCUSSION AND CONCLUSIONS

In this work, the performance of the InSAR-GPS data integration technique, developed by Samsonov et al. (2006), has been assessed by using the Sentinel-1 InSAR data and the GPS observations of the BARDN and those of 115 additional stations to retrieve the 3D displacement map induced by the 2014 Napa Valley earthquake.

The co-seismic slip reached the surface, producing a 15 km-long rupture extending through vineyards, roads and even houses causing significant damages and about 200 injured [Hudnut et al., 2014].

The InSAR-GPS integration method works quite well revealing 3D components of the surface deformation field compatible with the fault geometry provided by the USGS reports ([http://earthquake.usgs.gov/earthquakes/eventpage/nc72282711#scientific\\_finitefault](http://earthquake.usgs.gov/earthquakes/eventpage/nc72282711#scientific_finitefault)).

However, there are also some drawbacks that will require further investigations. Although California has one of the most dense GPS networks in the world, the main limitation comes from the limited number of GPS stations in close proximity of the epicentral area, where the largest co-seismic surface deformation occurred. This is the reason why the deformation pattern seems to be strongly led by the shape of the LOS displacement field detected by InSAR, although the values of the three position components are also influenced by the GPS measurements. In order to better constrain the N-S component, future developments regarding the data integration processing chain will be focused on the exploitation of other remote sensing techniques such as the POT.

The POT technique [22], based on pixel cross-correlation estimation, can measure displacements along the satellite azimuth direction, i.e. approximately N-S movements when considering quasi-polar orbits. Although it provides significant information for large deformation fields, however, the accuracy is not comparable with that of the InSAR and GPS measurements. The interpolation of the GPS displacements leads to errors affecting the quality of the estimates. Other interpolation techniques such as the Inverse Distance Weighting (IDW) will be explored in future developments by taking into account the spatial discontinuity due to the fault system.

Finally, as revealed by several studies [13][23][24], the earthquake epicenter is located 1.7 Km westward of the known West Napa Fault system, and it mostly ruptured unmapped portions of this fault system. Therefore, to fully address all of the observed features, as well as to provide new insights about the slipping fault, additional investigations are required regarding, for example, the inversion of the optimized 3D co-seismic deformation field and the spatial and temporal distribution of the seismicity associated to the main shock.

## REFERENCES

- [1] Polcari M., Palano M., Fernández J., Samsonov S.V., Stramondo S., Zerbini S. (2016) - *3D displacement field retrieved by integrating Sentinel-1 InSAR and GPS data: the 2014 South Napa earthquake*. European Journal of Remote Sensing, vol. 49, pp. 1-13, doi: 10.5721/EuJRS20164901
- [2] Gudmunsson S., Sigmundsson F. (2002) - *Three-dimensional surface motion maps estimated from combined interferometric synthetic aperture radar and GPS data*. Journal of Geophysical Research, vol. 107, no. B10, doi: 10.1029/2001JB000283.
- [3] Samsonov S., Tiampo K., Rundle J., Li Z. (2007) - *Application of DinSAR-GPS Optimization for Derivation of Fine-Scale Surface Motion Maps of Southern California*. IEEE Transactions on Geoscience and Remote Sensing, vol. 45, no. 2, doi: 10.1109/TGRS.2006.887166.
- [4] González P.J., Tiampo K., Camacho A., Fernández J. (2010) - *Shallow flank deformation at Cumbre Vieja volcano (Canary Islands): Implications on the stability of steep-sided volcano flanks at oceanic islands*. Earth and Planetary Science Letters, vol.297, 545-557, doi: 10.1016/j.epsl.2010.07.006.
- [5] Guglielmino F., Nunnari G., Puglisi G., Spata A. (2011) - *Simultaneous and Integrated Strain Tensor Estimation From Geodetic and Satellite Deformation Measurements to Obtain Three-Dimensional Displacement Maps*. IEEE Transactions on Geoscience and Remote Sensing, vol. 49, no.6, pp. 1815 – 1826, doi: 10.1109/TGRS.2010.2103078.
- [6] Joyce K.E., Samsonov S.V., Levick S.R., Engelbrecht J., Belliss S. (2014) - *Mapping and monitoring geological hazards using optical, LiDAR, and synthetic aperture RADAR image data*. Natural Hazards, vol. 73, Issue 2, pp 137-163, doi: 10.1007/s11069-014-1122-7.
- [7] Stramondo S., Bozzano F., Marra F., Wegmuller U., Cinti F.R., Moro M., Saroli M. (2008) - *Subsidence induced by urbanization in the city of Rome detected by advanced InSAR technique and geotechnical investigations*. Remote Sensing of Environment, vol. 112, 3160–3172, doi: [10.1016/j.rse.2008.03.008](https://doi.org/10.1016/j.rse.2008.03.008).
- [8] Polcari M., Albano M., Saroli M., Tolomei C., Lancia M., Moro M., Stramondo S. (2014) - *Subsidence detected by multi-pass Differential SAR Interferometry in the Cassino plain (Central Italy): joint effect of geological and anthropogenic factors?*, Remote Sensing Journal, vol. 6, 9676-9690; doi: 10.3390/rs6109676.
- [9] Palano M., Puglisi G., Gresta S. (2008) - *Ground deformation patterns at Mt. Etna from 1993 to 2000 from joint use of InSAR and GPS techniques*. Journal of Volcanology and Geothermal Research 169, 99-120. doi: 10.1016/j.jvolgeores.2007.08.014.
- [10] Fernández J., González, P.J., Camacho A.G., Prieto J.F., Bru G. (2015) - *Volcano geodetic research in the Canary Islands: A summary of results and perspectives*. Pure and applied geophysics, in press, doi: 10.1007/s00024-014-0916-6.
- [11] Trasatti E., Polcari M., Bonafede M., Stramondo S. (2015) - *Geodetic constraints to the source mechanism of the 2011-2013 unrest at Campi Flegrei (Italy) caldera*. Geophysical Research Letters, 42, doi: 10.1002/2015GL063621.

- [12] Samsonov S., Tiampo K. (2006) - *Analytical Optimization of a DInSAR and GPS Dataset for Derivation of Three-Dimensional Surface Motion*. IEEE Geoscience and Remote Sensing Letters, Vol. 3, no. 1, doi: 10.1109/LGRS.2005.858483.
- [13] Barnhart W.D., Murray J.R., Yun S.-H., Svarc J. L., Samsonov S. V., Fielding E. J., Brooks B. A., Milillo P. (2015) - *Geodetic Constraints on the 2014 M 6.0 South Napa Earthquake*. Seismological Research Letters, vol. 86, pp. 335-343, doi: 10.1785/0220140210.
- [14] Brooker P.I. (1991) - *A Geostatistical Primer*. World Scientific.
- [15] Li S. (2001) – *Markov random field modeling in image analysis*. Springer-Verlag.
- [16] Wegmuller U., Werner C. (1997) - *Gamma SAR processor and interferometry software*. In The 3rd ERS symposium on space at the service of our environment, Florence, Italy, 1997.
- [17] Costantini M. (1998) - *A novel phase unwrapping method based on network programming*. IEEE Transactions on Geoscience and Remote Sensing, vol. 36, no. 3, pp. 813-821, doi: 10.1109/36.673674.
- [18] Goldstein R., Werner C. (1998) - *Radar interferogram filtering for geophysical applications*. Geophysical Research Letters, vol. 25, no. 21, pp. 4035-4038, doi: 10.1029/1998GL900033.
- [19] Altamini Z., Metivier L., Collilieux X. (2012) - *ITRF2008 plate motion model*. Journal of Geophysical Research, vol. 117, Issue B7, doi: 10.1029/2011JB008930
- [20] Hudnut K.W. et al. (2014) – *Key recovery factors for the August 24, 2014, South Napa earthquake*. U.S. Geological Survey Open-File Report, 1249, p.51, doi: [10.3133/ofr20141249](https://doi.org/10.3133/ofr20141249).
- [21] Wei S., Barbot S., Graves R., Lienkaemper J., Wang T., Hudnut K., Fu Y., Helmberger D. (2015) - *The 2014 Mw 6.1 South Napa Earthquake: A Unilateral Rupture with Shallow Asperity and Rapid Afterslip*. Seismological Research Letters, vol. 86, nr. 2°, doi: [10.1785/0220140249](https://doi.org/10.1785/0220140249).
- [22] Strozzi T, Luckman A., Murray T., Wegmuller U., Werner C. (2002) – *Glacier motion estimation using SAR offset-tracking procedures*. IEEE Transactions on Geoscience and Remote Sensing, 40, 11, pp. 2384-2391, doi: 10.1109/TGRS.2002.805079.
- [23] Brocher T.M., Baltay A.S., Hardebeck J.L., Pollitz F.F., Murray J.R., Llenos A.L., Schwartz D.P., Blair J.L., Ponti D.J., Lienkaemper J.J., et al. - (2015). *The M 6.0 24 August 2014 South Napa Earthquake*. Seismological Research Letters, vol 86, no. 2A, doi: 10.1785/0220150004.
- [24] Ji C., Archuleta R., Twardzik C. (2015) – *Rupture history of 2014 Mw 6.0 South Napa earthquake inferred from near-fault strong motion data and its impact to the practice of ground strong motion prediction*. Geophysical Research Letters, vol.42, issue 7, doi: 10.1002/2015GL063335.

# **CHAPTER 4: AN ADVANCED ALGORITHM TO CONSTRAIN THE 3D SURFACE DISPLACEMENT MAPS BASED ON DATA INTEGRATION: THE CASE STUDY OF NAPA VALLEY EARTHQUAKE**

## **4.1 OVERVIEW ON THE DATA INTEGRATION**

The integration of different geodetic data to constrain the 3D components of a surface displacement field due to a natural or anthropic phenomenon is a topic widely debated in literature. In particular, previous works are mainly focused on the InSAR-GPS data integration [1-5] because of complementarity of these two techniques.

Indeed, as well known, InSAR estimates the range between the Earth's surface and the sensor along the satellite Line-of-Sight (LOS). Since the satellites usually acquire with an incidence angle spanning between about  $20^{\circ}$  -  $30^{\circ}$ , the LOS displacement is almost corresponding to the vertical displacement component. Therefore due to the viewing geometry, InSAR is able to better constrain deformation fields mostly characterized by a vertical displacement component as in the case of subsidence [6][7] or volcanos inflation/deflation [8-10].

On the other hand, a GPS station provides the precise estimation of absolute and continuous 3D site coordinates. In particular, the horizontal displacement is better constrained by a GPS network since bad estimates of the tropospheric delay produce large errors mainly on the vertical position.

Indeed, errors on the horizontal position will be averaged in some way if measurements are conducted on an entire day or more because of the satellite trajectory, that could not be the case for vertical position since signal is always coming from above.

Therefore, InSAR and GPS are techniques fully complementary and suitable to be merged in order to study several phenomena and estimate the relative 3D deformation produced on the Earth's surface.

However, in some cases the displacement field could not be well constrained by using only InSAR and GPS techniques. Indeed, sometimes the deformation field is mainly characterized by an horizontal displacement component as in the case of an earthquake with a strike-slip fault mechanism and the available GPS network is not dense enough. Typically, the distance between GPS stations belonging to the same network can span from few to tens of kilometers. Then, the information provided by GPS stations needs oftentimes to be interpolated. Unfortunately, this process might be the source of errors proportional to the distance among stations and sometimes the entire signal is missing if it completely falls between stations.

Therefore, in the study of some phenomena could be need the use of other geodetic techniques to better constrain the horizontal displacement especially considering the NS component.

Among them, the POT [11] and MAI [12] are able to estimate any movements along the satellite azimuth direction, i.e. approximatively NS movements when considering quasi-polar orbits.

However, the accuracy is not comparable with that of InSAR and GPS measurements, although it provides significant information for large deformation fields so that it can be useful to improve the present knowledge.

In the present work we slightly modify the method proposed by Samsonov et al, 2006 for the InSAR-GPS data integration. In particular, we developed a processing chain by including the results from POT and MAI in addition to the ones provided by InSAR and GPS but any other data sources in matrix form can also be easily added.

Moreover we change the GPS interpolation method in order to take into account for the possible spatial discontinuities due to a natural phenomenon such as an earthquake or a landslides.

The method was applied to the case study of the 2014 Mw 6.0 South Napa earthquake. The seismic event occurred on August 24th, 2014 southwest of the city of Napa, California, along the San Andreas Fault system and caused several damages producing a 15 Km-long rupture through vineyards, roads and even houses (Fig. 4.1).



Figure 4.1: Epicenter of the 2014 Napa Valley earthquake (upper left) and roads damaged by the seismic event

## 4.2 DATASET

The SAR data used to perform InSAR, POT and MAI analysis consists in a pair of images acquired along descending orbit by the recent Sentinel-1 satellite on August 7<sup>th</sup> and 31<sup>st</sup> respectively. They were acquired in Stripmap mode and represent two of the first acquisitions available from Sentinel-1, launched on April 2014 from Europe's Spaceport in French Guyana.

The image pair, characterized by a perpendicular baseline of 2 meters and a resolution of about 4x4 meters, was multi-looked by a factor of 15 in both range and azimuth obtaining a pixel size of about 60x60 meters and then processed with the GAMMA software [13].

To remove the topography in the InSAR and MAI analysis was used The Digital Elevation Model (DEM) provided by the SRTM mission.

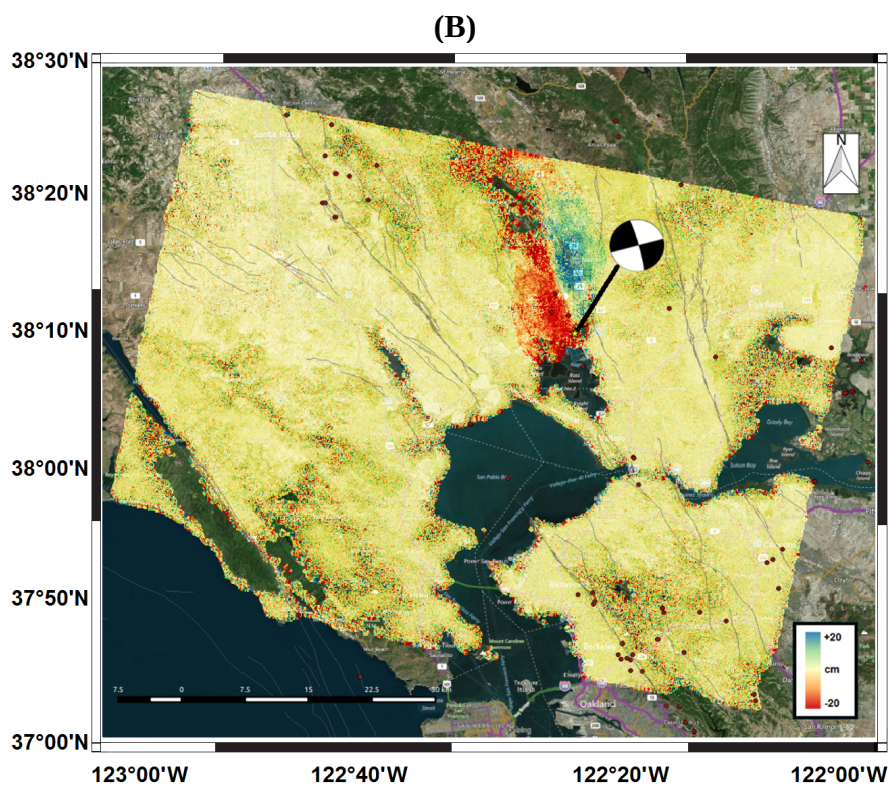
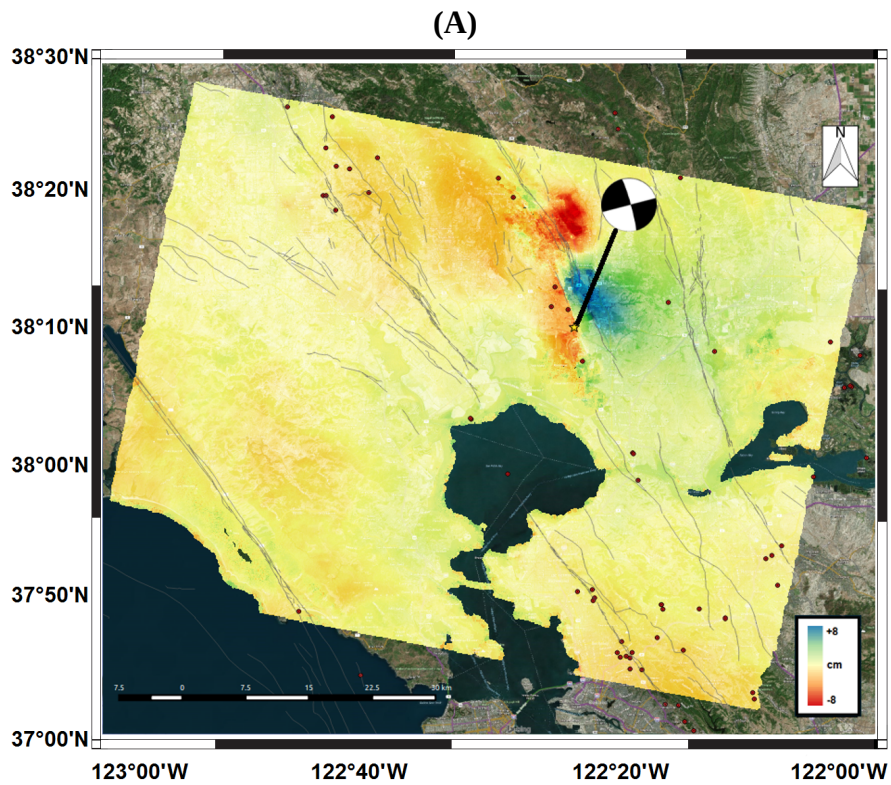
On the other hand, the analyzed GPS dataset, spanning from August 1st to September 2nd, includes 32 stations belonging to the Bay Area Regional Deformation Network (BARDN), 301 continuous stations available from the UNAVCO and the CDDIS archives, and 13 additional campaign stations from Barnhart et al, 2014 [14]. The GNSS raw observations were processed by means of the GAMIT/GLOBK 10.5 software (<http://www-gpsg.mit.edu>), using precise IGS orbits (International GNSS Service; <http://igsceb.jpl.nasa.gov>) and IERS Earth orientation parameters (International Earth Rotation Service; <http://www.iers.org>). All stations were organized and processed into three sub-networks, each one including about 50 stations and sharing a few common points to provide the necessary ties between them. The results of this processing step are daily estimates of loosely constrained station coordinates parameters, along with the associated variance-covariance matrices. In a successive step, these loosely constrained daily solutions were used as quasi observations in a Kalman filter (GLOBK) in order to estimate a consistent set of daily coordinates (i.e. time series) for all the sites involved.

The coseismic displacement was estimated by averaging the site position all over the 2 days before and after the event, and by applying minimal inner constraints (i.e., constraining translations, scale and rotations, to 0.5 mm).

In order to make comparable the different data a single reference have to be chosen. Indeed, the deformation provided by SAR data is related to a reference point (the "zero deformation") within the frame whereas the GPS measurements are referred to a global reference system such as WGS84, ED50, GRS80 or, as in the studied case, NAD83.

First, all the GPS measurements were projected along the satellite LOS to select the GPS station with the LOS deformation value closer to zero as SAR reference point. In this case, the TIBB\_GPS station (southern part of the frame) was chosen as SAR reference point showing a LOS displacement of  $\sim -0.8$  mm. Then, the GPS measurements of the other stations, i.e.  $D_x$ ,  $D_y$ ,  $D_z$ , were

scaled with respect to those ones of TIBB\_GPS station to have the same "zero deformation" for SAR and GPS. The available dataset used in the integration approach is shown in figure 4.2.





### 4.3 METHOD

The algorithm for integrating data implemented in this work is based on the method for the InSAR-GPS data integration developed by Samsonov et al., 2006 [2] and used in several case studies [15] [16]. This method exploits the Bayes theory to estimate the three deformation rate component of a surface displacement field. The theoretical aspect of the integration are widely described in Polcari et al., 2016 [5]. In particular, the data integration consists in constructing an energy function and search for its minimum:

$$U(b/a) = \sum_{i=1}^N \frac{(b_i - a_i)^2}{2\sigma_i^2} \quad (4.1)$$

The minimization of 4.1 allows to obtain the three deformation rate components of a displacement field.

In the case of InSAR-GPS data integration the interpolation of the GPS data onto the InSAR grid point is first needed and then the three deformation rate components are found by searching for the minimum of the following energy function:

$$U(v_{EW}, v_{NS}, v_{UP} / V_{LOS}, V_{EW}, V_{NS}, V_{UP}) = \sum_{i=1}^N \frac{1}{(2\sigma_{sar}^i)^2} (V_{LOS}^i + v_{EW} \cos(\alpha) \cos(\theta) - v_{NS} \sin(\alpha) - v_{UP} \cos(\theta))^2 + \frac{1}{(2\sigma_{EW_{gps}}^i)^2} (V_{EW}^i - v_{EW})^2 + \frac{1}{(2\sigma_{NS_{gps}}^i)^2} (V_{NS}^i - v_{NS})^2 + \frac{1}{(2\sigma_{UP_{gps}}^i)^2} (V_{UP}^i - v_{UP})^2 \quad (4.2)$$

In the present work, the method was slightly modified and tested in the study of the 2014 Napa valley earthquake.

In particular, the data from MAI and POT techniques were added in the integration processing chain in order to better constrain the NS displacement component. Indeed, both technique are able to estimate the displacement along the satellite azimuth direction. Since the satellites usually follow quasi-polar orbits, (the angle between the orbit and the geographic north is very low) the azimuth displacement can be approximated to the NS displacement. In addition, as highlighted by the data, the deformation field induced by the earthquake shows a strong different behavior along the west and the east side of the rupture. Therefore, with respect to the original method by Samsonov et al., 2006, the GPS data interpolation was led adding some boundaries to take into account for the spatial discontinuity. Lastly, the displacement components instead of the deformation rate ones were

searched to take into account for the sudden surface displacement induced by the earthquake.

Then, in details, the following datasets are available from the four techniques:

$$\bullet \quad D_{GPS} = [D_{EW-GPS}, D_{NS-GPS}, D_{UP-GPS}] = D_{EW-GPS} + D_{NS-GPS} + D_{UP-GPS} \quad (4.3)$$

$$\bullet \quad D_{InSAR} = [d_{EW}, d_{NS}, d_{UP}] [-\cos\alpha \sin\theta, \sin\alpha \sin\theta, \cos\theta]^T = -d_{EW} \cos\alpha \sin\theta + d_{NS} \sin\alpha \sin\theta + d_{UP} \cos\theta \quad (4.4)$$

$$\bullet \quad D_{MAI} = [d_{EW}, d_{NS}, d_{UP}] [\sin\alpha, \cos\alpha, 0]^T = d_{EW} \sin\alpha + d_{NS} \cos\alpha \quad (4.5)$$

$$\bullet \quad D_{POT} = [d_{EW}, d_{NS}, d_{UP}] [\sin\alpha, \cos\alpha, 0]^T = d_{EW} \sin\alpha + d_{NS} \cos\alpha \quad (4.6)$$

For sake of simplicity, the NS component by InSAR data is neglected since the NS component of the vector pointing from the ground toward the satellite is close to zero.

In order to retrieve the displacement field components,  $d_{EW}, d_{NS}, d_{UP}$ , the minimum of the following energy function needs to be found:

$$\begin{aligned} U(d_{EW}, d_{NS}, d_{UP} / D_{InSAR}, D_{MAI}, D_{POT}, D_{EW-GPS}, D_{NS-GPS}, D_{UP-GPS}) = & \sum_{i=1}^N \frac{1}{2\sigma_{InSAR_i}^2} [D_{InSAR_i} - (-d_{EW_i} \cos\alpha \sin\theta + d_{UP_i} \cos\theta)]^2 \\ & + \frac{1}{2\sigma_{MAI_i}^2} [D_{MAI_i} - (d_{EW_i} \sin\alpha + d_{NS_i} \cos\alpha)]^2 \\ & + \frac{1}{2\sigma_{POT_i}^2} [D_{POT_i} - (d_{EW_i} \sin\alpha + d_{NS_i} \cos\alpha)]^2 \\ & + \frac{1}{2\sigma_{GPS_{EW_i}}^2} [D_{EW-GPS_i} - d_{EW_i}]^2 + \frac{1}{2\sigma_{GPS_{NS_i}}^2} [D_{NS-GPS_i} - d_{NS_i}]^2 + \frac{1}{2\sigma_{GPS_{UP_i}}^2} [D_{UP-GPS_i} - d_{UP_i}]^2 \end{aligned} \quad (4.7)$$

Where:

- $\sigma_{MAI}$ ,  $\sigma_{POT}$ ,  $\sigma_{InSAR}$ ,  $\sigma_{GPS}$  are the standard deviations of the data
- $N$  is the number of grid points
- $\alpha$  and  $\theta$  are the azimuth and the incidence angle of the satellite

Equation 4.7 consists in six non-negative terms for each index  $i$ , i.e. for each point of the image.

Therefore, the stationary points (points of maximum, minimum or flexed) of the energy function in 4.7 can be found by setting to zero the first partial derivatives:

$$\begin{cases} \frac{\partial U}{\partial d_{EW_i}} = 0 \\ \frac{\partial U}{\partial d_{NS_i}} = 0 \quad \forall i \\ \frac{\partial U}{\partial d_{UP_i}} = 0 \end{cases} \quad (4.8)$$

This set of the three equations with three unknowns has to be solved for each grid point, i.e. for each index  $i$ . In order to find the minimum of the  $U(d_{EW}, d_{NS}, d_{UP})$  is needed studying the determinant of the Hessian matrix:

$$H_U(d_{EW}, d_{NS}, d_{UP}) = \begin{vmatrix} \frac{\partial^2 U}{\partial d_{EW}^2} & \frac{\partial^2 U}{\partial d_{EW} \partial d_{NS}} & \frac{\partial^2 U}{\partial d_{EW} \partial d_{UP}} \\ \frac{\partial^2 U}{\partial d_{NS} \partial d_{EW}} & \frac{\partial^2 U}{\partial d_{NS}^2} & \frac{\partial^2 U}{\partial d_{NS} \partial d_{UP}} \\ \frac{\partial^2 U}{\partial d_{UP} \partial d_{EW}} & \frac{\partial^2 U}{\partial d_{UP} \partial d_{NS}} & \frac{\partial^2 U}{\partial d_{UP}^2} \end{vmatrix} \forall i \quad (4.9)$$

When  $H_U(d_{EW}, d_{NS}, d_{UP})$  has both determinant and minors greater than zero the found point is a minimum of the function  $U(d_{EW}, d_{NS}, d_{UP})$ .

It can be shown that the set of three equations in 4.7 is always solvable and returns a single minimum point for each index  $i$  thus being a global minimum of  $U(d_{EW}, d_{NS}, d_{UP})$ .

#### 4.3.1 PROGRAMMING SIDE

The algorithm of data integration was implemented in Interactive Data Language (IDL) and it can be easily run on several platforms such as Linux, Windows and Macintosh. Both input and exported output data are in GeoTIFF format in order to be compatible and usable with any Geographic Information System (GIS) application.

First, all the data were converted into the same unit of measurements according to the size of the studied phenomenon: in the case of Napa Valley earthquake, have been chosen the meters.

In addition, also the measured displacement fields have to be uniformed to a single standard. In particular, specific care is required in considering both MAI and POT results since is considered positive the displacement moving in the same direction of the satellite flight.

Therefore, along descending orbit the NS displacement component retrieved by these two techniques is reversed compared to the conventional standard (positive when the displacement is northward). Accordingly, the MAI and POT measured displacements have to be multiplied by -1 to correct this inconsistency.

Once all data are consistent to each other is possible to solve the system of equations 4.8 by using some support variables because of the complexity due to the huge number of variables involved.

The time required to extract the 3D displacement component clearly depends on the number of

points of the grid. Here, the data-matrix involved were formed by 1169 rows and 1816 columns thus returning in more than 2 millions of points to be analyzed. In this case, the algorithm took less than 10 minutes to produce the output data. Considering, for example, that for a pixel posting of about 40m a multi-looked SAR frame has a size of  $\sim 2500$  rows by 2500 columns for ERS and Envisat data,  $\sim 1000$  rows by 1200 columns for Cosmo-SkyMed data and  $\sim 6250$  rows by 2500 columns for Sentinel-1 data in IW mode, is evident how the computational burden of the algorithm is not so high. In addition it can be also easily adapted in order to take into account for other source of data such as leveling data or optical data to be added in 4.7. The block diagram of the method is pointed out in figure 4.3. For more details, the entire Computer Code is shown in Appendix A.

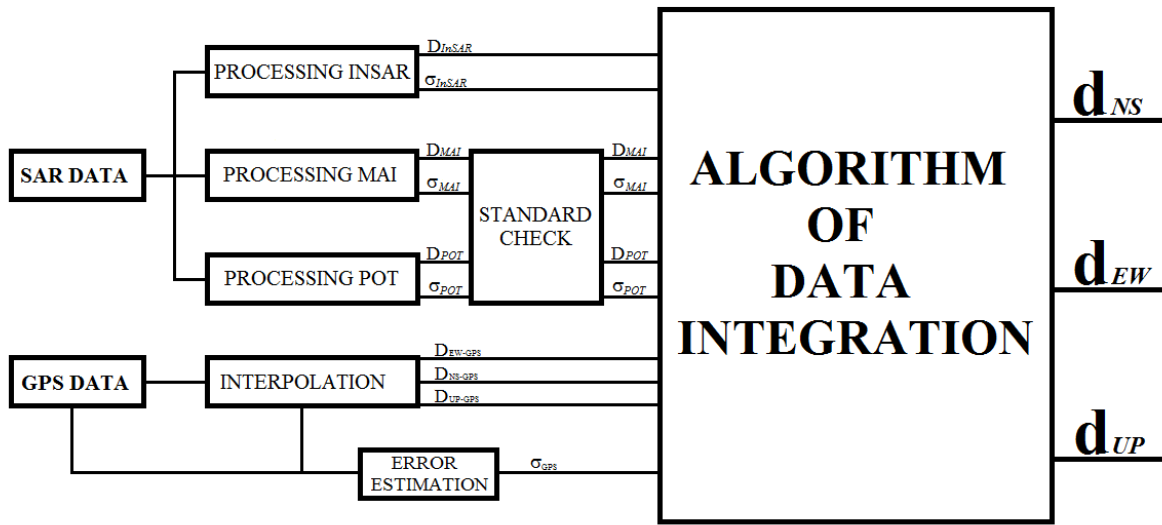


Figure 4.3: Block diagram of the implemented method

#### 4.4 ERRORS

Let us focus on the standard deviations used as weighting factors for the integration step in 4.7.

For InSAR data, no orbital errors has been considered because of the small spatial baseline ( $\sim 2$ m) and the precise orbit informations provided by Sentinel-1 mission. Moreover, the high coherence of the area (see Appendix B) and the short temporal baseline between the two acquisitions (24 days) allow neglecting also any atmospheric artifacts without loss of generality. Then, the standard deviation of the displacement measured by InSAR data can be expressed as follows [17]:

$$\sigma_{InSAR} = \frac{\lambda}{4\pi} \frac{1}{\sqrt{2M}} \frac{\sqrt{1-\gamma^2}}{\gamma} \quad (4.10)$$

Conversely, MAI and POT standard deviations were estimated according to previous works in

literature. Jung et al., 2014 [18] proposed the following value for the accuracy retrieved by the MAI approach:

$$\sigma_{MAI} = \frac{l}{4\pi n} \sigma_{\varphi} \approx \frac{l}{4\pi n} \frac{1}{\sqrt{M}} \frac{\sqrt{1-\gamma^2}}{\gamma} \quad (4.11)$$

Instead, the accuracy of POT was estimated by De Zan et al., 2103 [19]:

$$\sigma_{POT} \approx \frac{l}{2} \sqrt{\frac{3}{10M} \frac{\sqrt{2+5\gamma^2-7\gamma^2}}{\pi\gamma^2}} \quad (4.12)$$

where:

- $\lambda$  = Wavelength
- $M$  = Number of Looks
- $\gamma$  = Coherence
- $l$  = Antezza azimuth lenght
- $n$  = Normalized squint

As stated previously,  $M=225$  because of 15 looks both in range and azimuth direction.

In addition, C-Band Sentinel-1 satellite has a wavelength of about 5.5 cm whereas the antenna lenght in the azimuth direction is 12.3 m.

The normalized squint,  $n$ , calibrates the shihf of the squint angle with respect to the original value one (zero-doppler) to estimate the backward and forward beams in MAI approach and it was fixed to 0.5.

On the other hand, particular care is required in the estimation of the GPS error being due to both interpolation and measurement errors. However the measurement errors are only known at sparse location corresponding to the GPS sites and it can not be interpolated not depending on the distance between stations or on the geophysical characteristics of the phenomenon. Therefore, it was treated as the mean of the all instrumental errors and added to the interpolation error for each grid point in such a way:

$$\sigma_{GPS} = \sigma_{interp} + \frac{1}{L} \sum_{k=1}^L \sigma_{meas_k} \quad (4.13)$$

where  $L$  is the number of GPS stations into the SAR grid image.

Regarding the errors of the displacement components obtained by the integration algorithm,

$d_{EW}, d_{NS}, d_{UP}$ , they can be estimated according to [20]. Let us consider a function on  $n$  variables,

$y=f(x_1, x_2, \dots, x_n)$  and let be  $\sigma_i$  the standard deviation of the  $i$ -th variable. If the  $n$  variables are

uncorrelated, the standard deviation of  $y$  can be calculated as follows:

$$\sigma_y = \sqrt{\sum_{i=1}^n \left(\frac{\partial f}{\partial x_i}\right)^2 \sigma_{x_i}^2} \quad (4.14)$$

where  $\frac{\partial f}{\partial x_i}$  is the partial derivative of  $f$  with respect to the  $i$ -th variable.

Therefore, by applying to the case of  $d_{EW}, d_{NS}, d_{UP}$ , considering the energy function,  $U$ , to be minimized, we have:

$$\begin{aligned} d_{EW} &= U(D_{InSAR}, D_{MAI}, D_{POT}, D_{EW-GPS}, D_{NS-GPS}, D_{UP-GPS}) \\ d_{NS} &= U(D_{InSAR}, D_{MAI}, D_{POT}, D_{EW-GPS}, D_{NS-GPS}, D_{UP-GPS}) \\ d_{UP} &= U(D_{InSAR}, D_{MAI}, D_{POT}, D_{EW-GPS}, D_{NS-GPS}, D_{UP-GPS}) \end{aligned} \quad (4.15)$$

Since the condition of incorrelation between the variables is clearly satisfied, is possible to retrieve the errors of the estimated displacement component in such a way:

$$\begin{aligned} \sigma_{EW} &= \sqrt{\left(\frac{\partial U}{\partial D_{InSAR}}\right)^2 \sigma_{InSAR}^2 + \left(\frac{\partial U}{\partial D_{MAI}}\right)^2 \sigma_{MAI}^2 + \left(\frac{\partial U}{\partial D_{POT}}\right)^2 \sigma_{POT}^2} \\ &\quad + \sqrt{\left(\frac{\partial U}{\partial D_{EW-GPS}}\right)^2 \sigma_{GPS_{EW}}^2 + \left(\frac{\partial U}{\partial D_{NS-GPS}}\right)^2 \sigma_{GPS_{NS}}^2 + \left(\frac{\partial U}{\partial D_{UP-GPS}}\right)^2 \sigma_{GPS_{UP}}^2} \\ \sigma_{NS} &= \sqrt{\left(\frac{\partial U}{\partial D_{InSAR}}\right)^2 \sigma_{InSAR}^2 + \left(\frac{\partial U}{\partial D_{MAI}}\right)^2 \sigma_{MAI}^2 + \left(\frac{\partial U}{\partial D_{POT}}\right)^2 \sigma_{POT}^2} \\ &\quad + \sqrt{\left(\frac{\partial U}{\partial D_{EW-GPS}}\right)^2 \sigma_{GPS_{EW}}^2 + \left(\frac{\partial U}{\partial D_{NS-GPS}}\right)^2 \sigma_{GPS_{NS}}^2 + \left(\frac{\partial U}{\partial D_{UP-GPS}}\right)^2 \sigma_{GPS_{UP}}^2} \\ \sigma_{UP} &= \sqrt{\left(\frac{\partial U}{\partial D_{InSAR}}\right)^2 \sigma_{InSAR}^2 + \left(\frac{\partial U}{\partial D_{MAI}}\right)^2 \sigma_{MAI}^2 + \left(\frac{\partial U}{\partial D_{POT}}\right)^2 \sigma_{POT}^2} \\ &\quad + \sqrt{\left(\frac{\partial U}{\partial D_{EW-GPS}}\right)^2 \sigma_{GPS_{EW}}^2 + \left(\frac{\partial U}{\partial D_{NS-GPS}}\right)^2 \sigma_{GPS_{NS}}^2 + \left(\frac{\partial U}{\partial D_{UP-GPS}}\right)^2 \sigma_{GPS_{UP}}^2} \end{aligned} \quad (4.16)$$

## 4.5 GPS DATA INTERPOLATION

The GPS data interpolation is often a critical step that can significantly affect the results. The main error source is due to the distance among GPS stations. Indeed, a very dense GPS network is not so easy to be designed because of the considerable cost of a GPS receiver. Typically, the distance between stations belonging to the same network is of the order of the kilometers also considering the areas with the most dense GPS networks in the world such as California, Japan and New Zealand.

Therefore, with respect to our previous work [5], the measurements from 13 additional GPS campaign stations [14] were included in the interpolation. Some of them are located close to the epicentral area (Fig.4.2-D) thus allowing to better constrain the surface deformation induced by the earthquake.

Moreover, the original method of Samsonov et al. [2] is based on the Kriging interpolation technique that needs choosing an appropriate theoretical semivariogram model for each displacement component.

In general, this choice can be wrong since it requires an *a priori* knowledge of the experimental data. In addition, the method was mainly used in constraining displacement fields induced by slow or uniform deformations whereas the one produced by an earthquake is often characterized by sudden variations and spatial discontinuities.

Then, a different interpolation technique was adopted in order to take into account for the spatial discontinuities due to the system fault and avoid possible errors related to the choice of the semivariogram. In particular, in this case the Inverse Distance Weighting (IDW) interpolation technique was chosen since it is a local, robust and fast method and does not require any *a priori* knowledge of the data. Furthermore, it allows to easily lead the interpolation by introducing some barriers to simulate the presence of the faults responsible for an earthquake.

In Figure 4.4 is reported the comparison between the GPS data interpolated with the original method and the one implemented in this work. The improvement for the NS and the EW component is quite significant especially considering the transition zone. On the other hand, the UP component seems have problems in both methods showing an unphysical uplift in the first case and the so called “bull eyes” surrounding the GPS sites typical of the IDW technique in the second case.

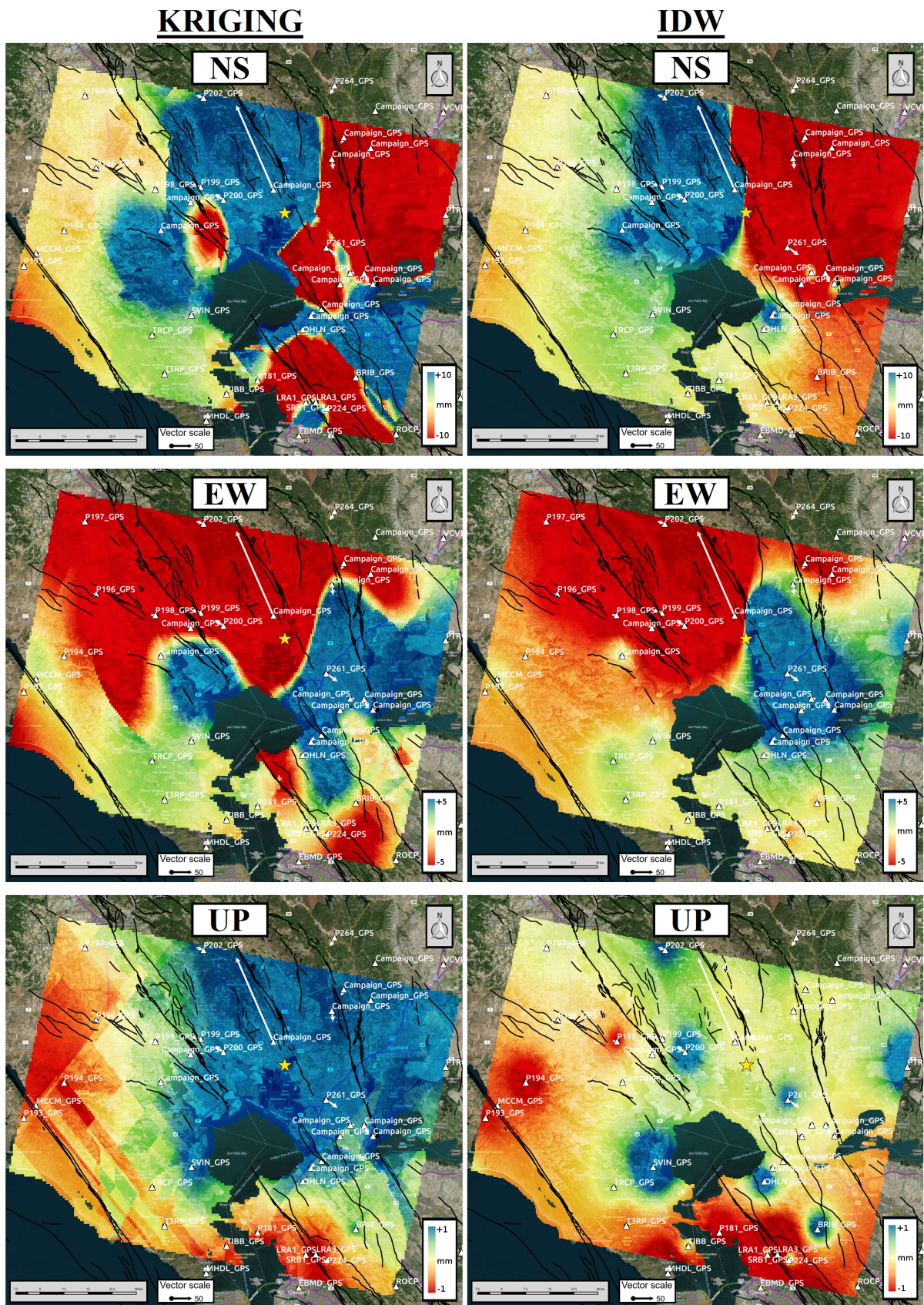
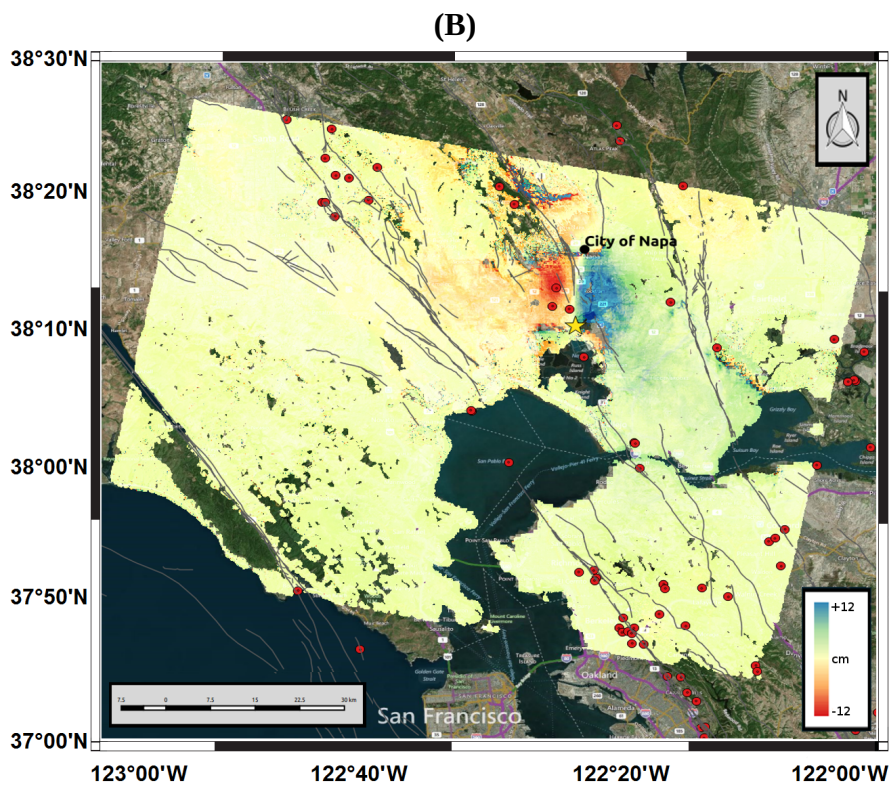
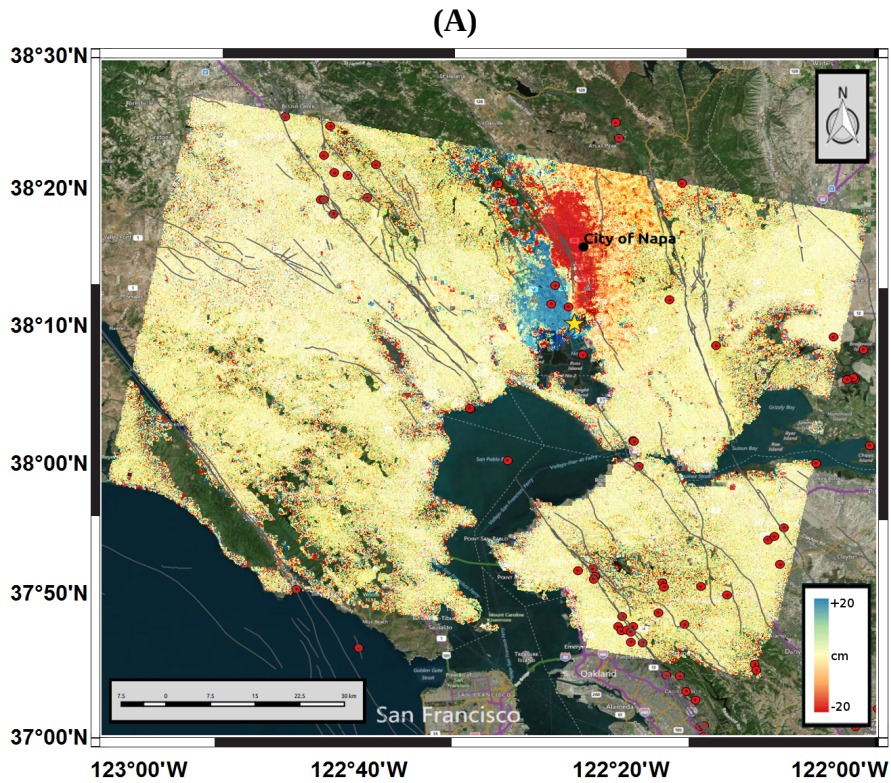


Figure 4.4: Interpolated GPS data. The left column represents the interpolation with the original kriging implemented in Samsonov et al., 2006 [REF] whereas in the right column is shown the interpolation used in this work. The yellow star refers to the earthquake epicenter. The GPS coseismic displacement is also reported by white arrows

## 4.6 RESULTS FOR THE NAPA EARTHQUAKE

The outcomes of the algorithm of data integration provided in terms of coseismic displacement components, i.e.  $d_{NS}$ ,  $d_{EW}$ ,  $d_{UP}$ , are shown in figure 4.5.



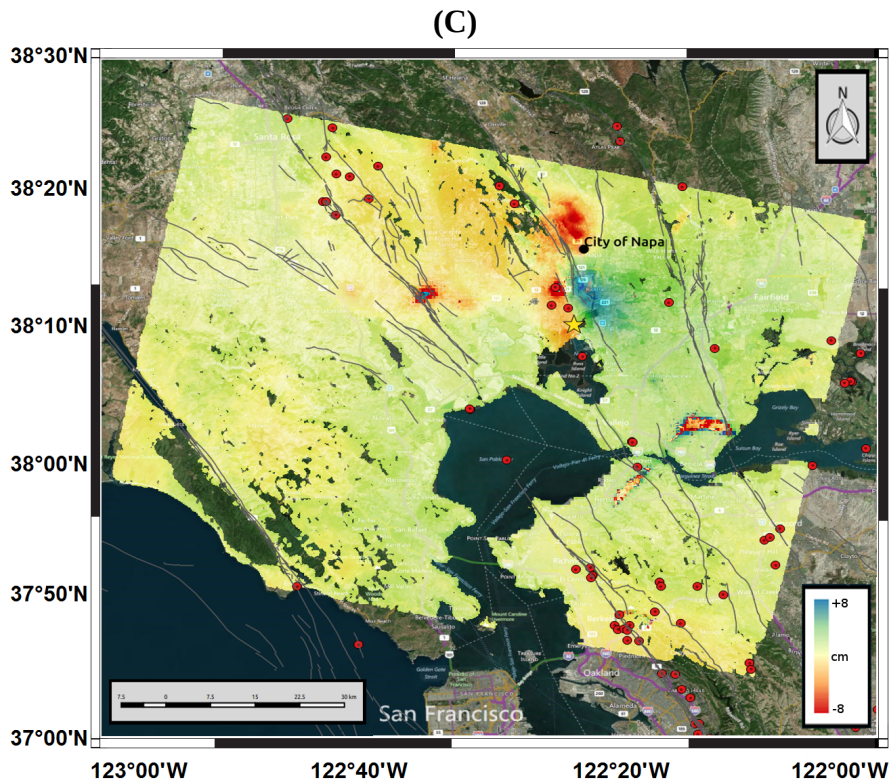


Figure 4.5: Coseismic displacement component obtained by the data integration algorithm. NS component (A), EW component (B) and UP component (C).  $M_w > 3.5$  seismicity (red circles) and the earthquake epicenter (yellow star) are also reported.

The experimental results show a displacement field characterized by a strong NS displacement component of about 15/20 cm along an approximately NW-SE plane.

This is in agreement with the typical strike-slip fault mechanism of the structures present in California such as the San Andreas Fault system and the West Napa Fault system. In particular, as shown in previous works [14][21-22], the epicenter of the Napa Valley earthquake is located ~1.7 Km westward of the known West Napa Fault and it ruptured along a right-lateral NW-SE trending fault plane, as clearly indicated by the estimated NS displacement component.

In addition, the coseismic displacement produced a remarkable EW deformation southern of the city of Napa, where an eastward component peaking at around 12 cm is observed.

On the other hand, the UP component is mainly located along the north-east side of the fault responsible for the earthquake, northern of the city of Napa. Here, the products of the data integration show a local subsidence with a maximum of 7-8 cm.

## 4.7 SOURCE MODELING

The obtained results were used as input to retrieve the source characteristics by performing a data inversion modeling. It was achieved by the inversion module implemented in the ENVI SARscape

software (<http://sarmap.ch/tutorials/ModelingTutorial1.pdf>). It uses the elastic dislocation source model for constraining the surface displacement induced by a uniform dislocation for a rectangular source in an elastic and homogeneous half-space [23]. The chosen inversion model is such to minimize a cost function based on the difference between observed and predicted geodetic data, i.e. the "best fit" solution. In particular, in the non-linear inversion, the source parameters are inferred from the geodetic data based on the Levenberg-Marquardt minimization algorithm [24] and the source is characterized by an uniform slip value. Once the fault geometry is found the linear inversion is used to constrain a realistic slip distribution of slip over the fault plane. Therefore, the coseismic displacement was modeled first via non-linear inversion in order to constrain the source parameters such as the position of the fault responsible for the earthquake, the strike etc. and then via linear inversion to retrieve the related slip distribution.

The input data were downsampled before starting the inversion. The area where the coseismic deformation occurs was downsampled setting the point density to about 500m in order to preserve the main features of the displacement field. On the other hand, the surrounding areas were downsampled with a density of  $\sim 2\text{Km}$ .

#### 4.7.1 SINGLE FAULT MODEL

Preliminary, the source model was designed by enforcing the solution of the inversion to work with an unique block thus simulating a single unruptured fault causing the earthquake. The search for the optimal solution was performed starting from the solution provided by the Global Centroid Moment Tensor (CMT) catalogue (Table 4.1). Therefore, the source parameters such as the fault length, width, depth etc. were searched in a range of values containing the CMT solution.

East (m)	559523.7
North (m)	4230443
Length (m)	14821
Width (m)	8880.6
Depth (m)	6356.7
Strike (deg)	338°
Dip (deg)	78°
Rake (deg)	-174°
Slip (m)	0.2648

Table 4.1: Source parameters from the CMT solution. The East and North are the central fault coordinates

In the first step of the inversion was performed the non-linear inversion by imposing uniform slip distribution and searching for the source geometry. In table 4.2 is reported the result.

East (m)	560721.3
North (m)	4234883.9
Lenght (m)	11839.2
Width (m)	5797
Depth (m)	2013.5
Strike (deg)	329°
Dip (deg)	69°
Rake (deg)	-193°
Slip (m)	0.81

Table 4.2: Source parameters obtained from the Non-Linear Inversion (Single Fault model). The East and North are the central fault coordinates

The source parameters retrieved by inverting the data obtained from the integration algorithm are consistent with an almost pure strike-slip fault mechanism (dip  $\sim 70^\circ$ ). Each displacement component was also modeled in order to assess the quality of the model. In figure 4.6 are shown the observed and modeled components and the relative residuals.

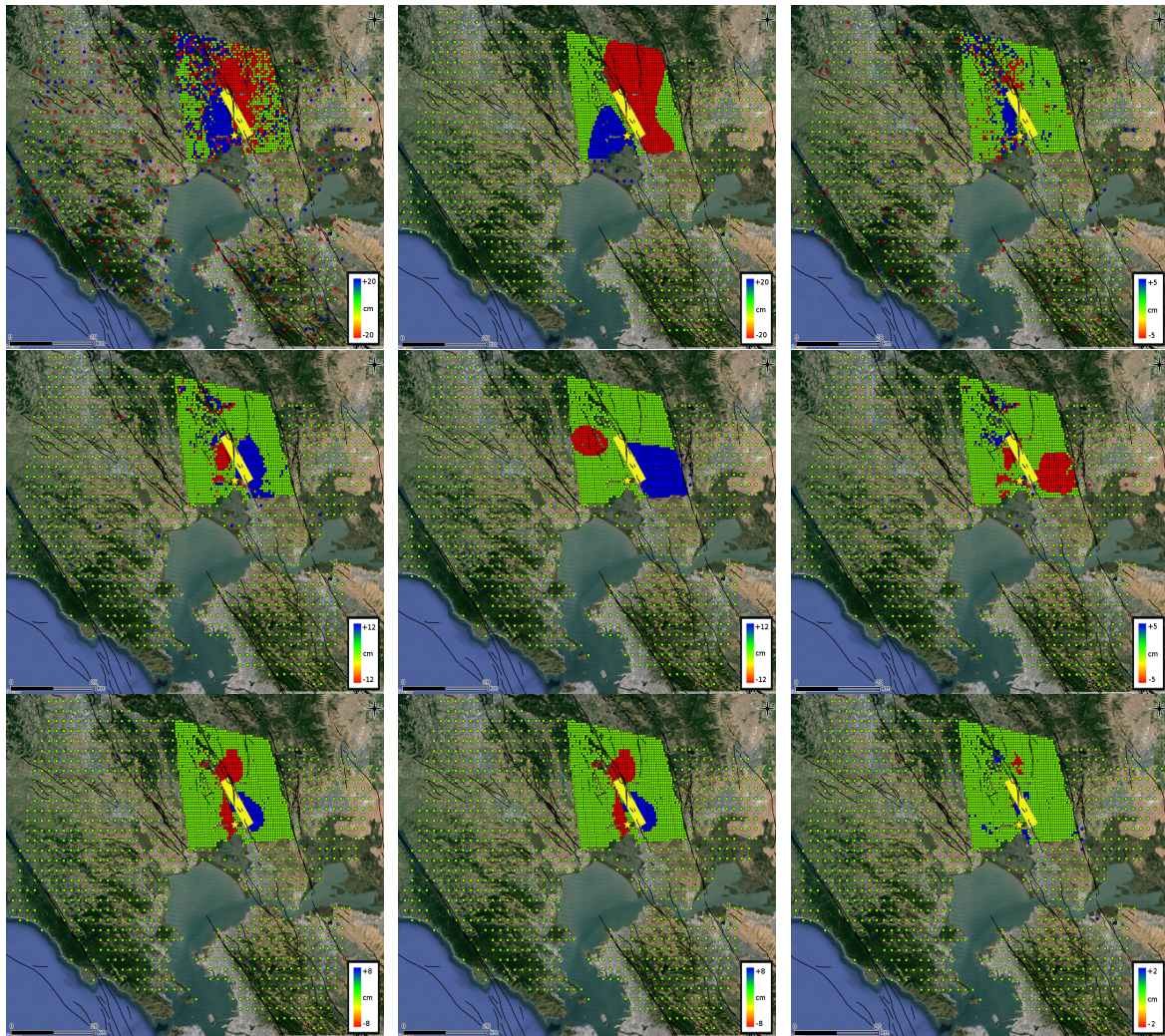


Figure 4.6: Single Fault modeling results. From left to right, observed, modeled and residuals for the NS (top), EW (middle) and the UP (down) components. The fault segment from the inversion is also reported (yellow rectangle)

As highlighted by the results, the source model performed with a single fault segment shows some critical issues. The UP component is well constrained by the model, with residuals less than 2 cm. Indeed, the estimation of this displacement component is mainly led by the InSAR data that are very accurate. On the other hand, the contributions of MAI, POT and GPS data weigh more in estimating the NS displacement component. Because of the lower accuracy of these data due to several reasons (geometry view, atmospheric artifacts, interpolation), the NS component is less well constrained by the model. In particular, the model underestimates the northward deformation occurred along the east side of the fault with residuals ranging between  $\sim 2$ -5 cm.

Finally, the main problems are related the EW component that shows high and widespread residuals ( $\sim 5$ cm) along both side of the fault. In this case, the model is not so able to reproduce the displacement especially considering the west side of the fault where it considers the westward deformation further north than the observed one.

#### 4.7.2 DOUBLE FAULT MODEL

As shown in previous section, the EW component peaks southern of the city of Napa and in particular it shows a strong eastward deformation. As explained in several works [22][26], the strike of the fault rotated of about  $15^\circ$ - $20^\circ$  counterclockwise few km far from the city of Napa and this rupture could be responsible for the detected EW displacement component. Therefore, to take into account for this strike variation, the coseismic displacement was modeled by using two segments of fault. Several tests were performed in order to obtain the best fit of the data varying some parameters. The best result was obtained by fixing the dip and the depth of both two segments to the values provided by the CMT solution, i.e.  $78^\circ$  and 6356.7 m respectively. Furthermore, the second segment of the fault, i.e. the southernmost one, was constrained to start at the end of the first one. In table 4.3 are shown the parameters of the two segments of fault retrieved via Non-Linear Inversion.

<b>Segment 1</b>		<b>Segment 2</b>	
East (m)	559003	East (m)	562872
North (m)	4235124	North (m)	4230074
Lenght (m)	11217	Lenght (m)	5243
Width (m)	8986	Width (m)	8246
Depth (m)	6356.7	Depth (m)	6356.7
Strike (deg)	$337^\circ$	Strike (deg)	$321^\circ$
Dip (deg)	$78^\circ$	Dip (deg)	$78^\circ$
Rake (deg)	$-173^\circ$	Rake (deg)	$-188^\circ$
Slip (m)	0.41	Slip (m)	0.36

Table 4.3: Parameters of the two fault's segment (Double Fault model). The East and North are the coordinates of the bottom left corner

Therefore, the second segment is characterized by a strike rotation of  $16^\circ$  with respect to the northernmost one ( $321^\circ$  vs  $337^\circ$ ) being consistent with the stronger EW deformation located along the south-east side of the fault. The results of the source modeling are shown in figure 4.7.

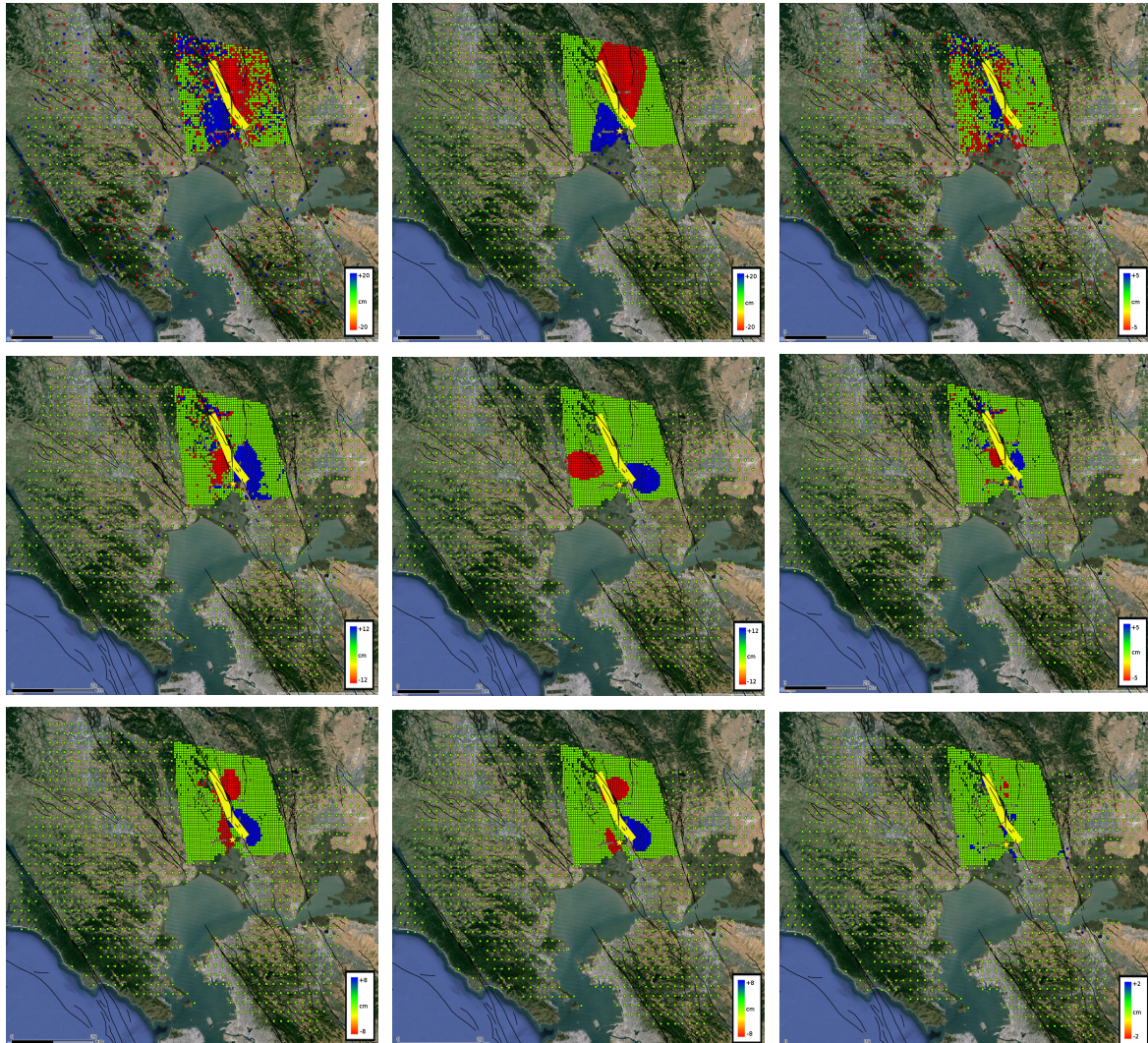


Figure 4.7: Double Fault modeling results. From left to right, observed, modeled and residuals for the NS (top), EW (middle) and the UP (down) components. The two fault's segment from the inversion are also reported (yellow rectangles)

The UP deformation component does not show significant changes with respect to the source modeling performed with a single fault segment. It is well constrained by the model and the residuals span in  $\pm 2$  cm. The NS component is quite accurately reproduced as well. The residuals are more less the same as in the case of the single fault model for the reasons explained previously. On the other hand, some improvements are registered for the EW component. The observed westward deformation on the west side of the fault is better constrained and also the opposite eastward deformation appears less diffused with respect to the single fault model. The residuals peak at around 5cm close the epicentral area highlighting a slight underestimate of the modeled EW component with respect to the observed one.

In order to retrieve the slip distribution the two segments of fault were first extended to let the slip vanish at their limits and then subdivided into patches of about 1 km. In particular, the northernmost segment was fixed to 12000 Km length by 10000 Km width and subdivided into 12 by 10 patches whereas the length and the width of the smallest one were set to 6000x10000 Km obtaining 6 by 10 patches.

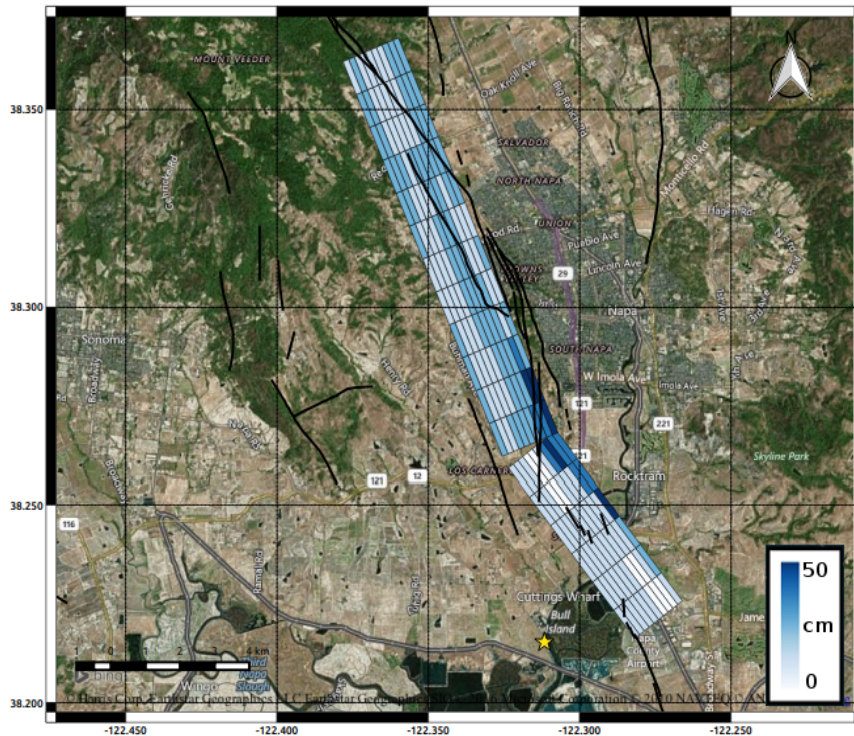


Figure 4.8: Slip distribution along the two segments of faults. The earthquake epicenter (yellow star) and the traces of the mapped faults (<http://earthquake.usgs.gov/hazards/qfaults/>) are also reported

As shown in figure 4.8, the earthquake mostly propagated some km northward from the epicenter and the maximum slip of about 44 cm was reached immediately south of the city of Napa. In particular, the slip peaks in proximity of the strike rotation proposed in this work maybe due to a fault rupture. The fault slip progressively decreases moving to the north and the south. However, as highlighted by Hudnut et al., 2014, offsets of ~10-20 cm caused several problems in the Browns Valley area, northwest of Napa, significantly damaging roads, pipelines and buildings.

These outcomes are consistent with the previous works showing the majority of slip of ~46 cm immediately adjacent to the city of Napa [14][25]. Furthermore, the strike rotation was also found by Wei et al., 2015 [26] and Ji et al., 2015 [22]. The results obtained in this work are more similar to the solution proposed by Wei et al., 2015. Indeed, he found two segments of fault westward dipping (strike of  $338^\circ$  and  $351^\circ$  respectively). On the other hand, Ji et al. proposed two segments eastward dipping (strike equal to  $159^\circ$  and  $179^\circ$ ).

## REFERENCES

- [1] Gudmunsson S., Sigmundsson F. (2002) - *Three-dimensional surface motion maps estimated from combined interferometric synthetic aperture radar and GPS data*. Journal of Geophysical Research, vol. 107, no. B10, doi: 10.1029/2001JB000283.
- [2] Samsonov S., Tiampo K. (2006) - *Analytical Optimization of a DInSAR and GPS Dataset for Derivation of Three-Dimensional Surface Motion*. IEEE Geoscience and Remote Sensing Letters, Vol. 3, no. 1, doi: 10.1109/LGRS.2005.858483.
- [3] González P.J., Tiampo K., Camacho A., Fernández J. (2010) - *Shallow flank deformation at Cumbre Vieja volcano (Canary Islands): Implications on the stability of steep-sided volcano flanks at oceanic islands*. Earth and Planetary Science Letters, vol.297, 545-557, doi: 10.1016/j.epsl.2010.07.006.
- [4] Guglielmino F., Nunnari G., Puglisi G., Spata A. (2011) - *Simultaneous and Integrated Strain Tensor Estimation From Geodetic and Satellite Deformation Measurements to Obtain Three-Dimensional Displacement Maps*. IEEE Transactions on Geoscience and Remote Sensing, vol. 49, no.6, pp. 1815 – 1826, doi: 10.1109/TGRS.2010.2103078.
- [5] Polcari M., Palano M., Fernández J., Samsonov S.V., Stramondo S., Zerbini S. (2016) - *3D displacement field retrieved by integrating Sentinel-1 InSAR and GPS data: the 2014 South Napa earthquake*. European Journal of Remote Sensing, vol. 49, pp. 1-13, doi: 10.5721/EuJRS20164901
- [6] Stramondo S., Bozzano F., Marra F., Wegmuller U., Cinti F.R., Moro M., Saroli M. (2008) - *Subsidence induced by urbanization in the city of Rome detected by advanced InSAR technique and geotechnical investigations*. Remote Sensing of Environment, vol. 112, 3160–3172, doi: 10.1016/j.rse.2008.03.008.
- [7] Polcari M., Albano M., Saroli M., Tolomei C., Lancia M., Moro M., Stramondo S. (2014) - *Subsidence detected by multi-pass Differential SAR Interferometry in the Cassino plain (Central Italy): joint effect of geological and anthropogenic factors?*, Remote Sensing Journal, vol. 6, 9676-9690; doi: 10.3390/rs6109676.
- [8] Palano M., Puglisi G., Gresta S. (2008) - *Ground deformation patterns at Mt. Etna from 1993 to 2000 from joint use of InSAR and GPS techniques*. Journal of Volcanology and Geothermal Research 169, 99-120. doi: 10.1016/j.jvolgeores.2007.08.014.
- [9] Fernández J., González, P.J., Camacho A.G., Prieto J.F., Bru G. (2015) - *Volcano geodetic research in the Canary Islands: A summary of results and perspectives*. Pure and applied geophysics, in press, doi: 10.1007/s00024-014-0916-6.
- [10] Trasatti E., Polcari M., Bonafede M., Stramondo S. (2015) - *Geodetic constraints to the source mechanism of the 2011-2013 unrest at Campi Flegrei (Italy) caldera*. Geophysical Research Letters, 42, doi: 10.1002/2015GL063621.
- [11] Joughin, I., (2002) - *Ice-sheet velocity mapping: a combined interferometric and speckle-tracking approach*. Annals of Glaciology, 34, 195–201.
- [12] Bechor, N.B.D. and Zebker, H.A. (2006) - *Measuring two-dimensional movements using a single InSAR pair*. Geophysical Research Letters, 33, L16311.

- [13] Wegmuller U., Werner C. (1997) - *Gamma SAR processor and interferometry software*. In The 3rd ERS symposium on space at the service of our environment, Florence, Italy, 1997.
- [14] Barnhart W.D., Murray J.R., Yun S.-H., Svarc J. L., Samsonov S. V., Fielding E. J., Brooks B. A., Milillo P. (2015) - *Geodetic Constraints on the 2014 M 6.0 South Napa Earthquake*. Seismological Research Letters, vol. 86, pp. 335-343, doi: [10.1785/0220140210](https://doi.org/10.1785/0220140210).
- [15] Samsonov S., Tiampo K., Rundle J., Li Z. (2007) - *Application of DinSAR-GPS Optimization for Derivation of Fine-Scale Surface Motion Maps of Southern California*. IEEE Transactions on Geoscience and Remote Sensing, vol. 45, no. 2, doi: [10.1109/TGRS.2006.887166](https://doi.org/10.1109/TGRS.2006.887166).
- [16] Samsonov S., Tiampo K., Rundle J. (2008) - *Application of DInSAR-GPS optimization for derivation of three-dimensional surface motion of the southern California region along the San Andreas fault*. Computer & Geoscience, 34, 5, 503–514.
- [17] Bamler R. and Hartl P. (1998) – *Synthetic Aperture Radar Interferometry*. Inverse Problems 14, R1–R54.
- [18] Jung H., Lee W., Zhang L. (2014) - *Theoretical Accuracy of Along-Track Displacement Measurements from Multiple-Aperture Interferometry (MAI)* . Sensors, 14, 17703-17724 doi:[10.3390/s140917703](https://doi.org/10.3390/s140917703)
- [19] De Zan F. (2013) - *Accuracy of Incoherent Speckle Tracking for Circular Gaussian Signals*. IEEE Geoscience and Remote Sensing Letters, 11, 1, 264-267, doi: [10.1109/LGRS.2013.2255259](https://doi.org/10.1109/LGRS.2013.2255259)
- [20] Taylor J. (1982) – An introduction to Error Analysis: The study of uncertainties in physical measurements. University Science Books, 1982.
- [21] Brocher T.M., Baltay A.S., Hardebeck J.L., Pollitz F.F., Murray J.R., Llenos A.L., Schwartz D.P., Blair J.L., Ponti D.J., Lienkaemper J.J., et al. - (2015). *The M 6.0 24 August 2014 South Napa Earthquake*. Seismological Research Letters, vol 86, no. 2A, doi: [10.1785/0220150004](https://doi.org/10.1785/0220150004).
- [22] Ji C., Archuleta R., Twardzik C. (2015) – *Rupture history of 2014  $M_w$  6.0 South Napa earthquake inferred from near-fault strong motion data and its impact to the practice of ground strong motion prediction*. Geophysical Research Letters, vol.42, issue 7, doi: [10.1002/2015GL063335](https://doi.org/10.1002/2015GL063335).
- [23] Okada, Y. (1985), Surface deformation due to shear and tensile faults in a half-space, Bull. Seismol. Soc. Am., 75, 1135–1154.
- [24] Marquardt, D. (1963), An algorithm for least-squares estimation of nonlinear parameters, SIAM J. Appl. Math., 11, 431 – 441, doi:[10.1137/0111030](https://doi.org/10.1137/0111030).
- [25] Hudnut K.W., Brocher T.M., Prentice C.S., Boatwright J., Brooks B.A., Aagaard B.T., Blair J.L., Fletcher J.B., Erdem J.E., Wicks C.W., Murray J.R., Pollitz F.F., Langbein J., Svarc J., Schwartz D.P., Ponti D.J., Hecker S., DeLong S., Rosa C., Jones B., Lamb R., Anne M. Rosinski A.M., McCrirk T.P., Dawson T.E., Seitz G., Rubin R.S., Glennie C., Hauser D., Ericksen T., Mardock D., Hoirup D.F., Bray J.D. (2014) - Key recovery factors for the August 24, 2014, South

Napa earthquake. U.S. Geological Survey Open-File Report, 1249, p.51, doi:  
<http://dx.doi.org/10.3133/ofr20141249>.

[26] Wei S., Barbot S., Graves R., Lienkaemper J., Wang T., Hudnut K., Fu Y., Helmberger D.

(2015) - The 2014 Mw 6.1 South Napa Earthquake: A Unilateral Rupture with Shallow Asperity and Rapid Afterslip. *Seismological Research Letters*, 86 (2): 344-354. doi:  
<http://dx.doi.org/10.1785/0220140249>.

## CHAPTER 5: GENERAL DISCUSSION

The aim of this work is to estimate the displacement maps induced by several phenomena characterizing the Earth's surface. In particular, geodetic satellite and in-situ data were exploited in order to accurately constrain the produced deformation. Indeed, remote sensing SAR data such as InSAR, MAI and POT are able to calculate the occurred deformation along the satellite LOS (InSAR) and azimuth (MAI and POT) whereas the GPS data provide measurements about the position, i.e. North, East and Up, of a GPS receiver.

### 5.1 DATA PROPERTIES

Whereas the investigated displacement field is mainly due to a vertical deformation, InSAR and Advanced InSAR (A-InSAR) data are able to perform the maps with high reliability. Indeed, the viewing geometry of a SAR sensor is usually such as to observe with an incidence angle quite low (less than  $30^\circ$ ) thus being more sensitive to vertical movements than to the horizontal ones. Therefore, deformation fields due to phenomena like volcano uplift, normal and reverse fault mechanism or urban subsidence, could be well constrained by using InSAR data only.

Conversely, MAI and POT are more suitable in the study of surface deformation with a strong NS component as in the case of strike-slip fault mechanism. Both techniques estimate the components of the observed deformation along the azimuth direction also known as the satellite Line-of-Flight. Since the satellites designed for the Earth's observation have quasi-polar orbit, the angle between the geographic north and the satellite Line-of-Flight is very small, of the order of  $10^\circ$ . Therefore, the component of a deformation field along the azimuth is approximately like the NS one.

At the present, the accuracy of MAI and POT data is lower than InSAR data being dependent on parameters like the antenna length or the pixel size. Furthermore, they can only be applied to pairs of SAR data thus allowing to constrain a single event and not to follow a temporal trend of a phenomenon.

On the other hand, the measurements provided by a GPS receiver are very precise especially concerning the horizontal components, i.e. the NS and the EW, however, they are punctual informations. For this reason, a GPS network is particularly efficient in monitoring slow regional trend generally characterized by spatially homogeneous deformations or small scale phenomena such as a landslide or a building deformation.

Therefore, depending on the characteristics of the studied phenomenon, the use of one, two or all these sources of data may be needed.

## **5.2 STRENGTHS OF THE DATA INTEGRATION ALGORITHM**

Although, as stated in the previous section, sometimes is possible neglecting one or two component of a deformation field, it is always due to all the 3D deformation components.

Then, in order to retrieve a full 3D knowledge of the studied phenomenon is convenient the exploitation of all the available data. In particular, the data integration algorithm developed in this work allows retrieving a single displacement value for each point (in terms of 3D deformation components), which can be easily used for performing the modeling of the source of deformation.

Obviously, according to the features of the deformation field the available data will play a different role in the integration algorithm and the pattern of deformation for each component will be mainly led by the techniques which better constrain them.

In this work, the available dataset consists in GPS and SAR data providing InSAR, MAI and POT maps but any other source of informations expressed in matrix form can be included in the algorithm by slightly changing the code accordingly. Furthermore, the algorithm is also efficient in terms of time of computation thus allowing the processing of large areas within a reasonable time. This is very important especially considering the huge images provided by Sentinel-1 in IW mode (~250 Km).

## **5.3 DRAWBACKS OF THE DATA INTEGRATION ALGORITHM**

The drawbacks of the algorithm are due to several factors. First, it is important to understand that the GPS data interpolation will always introduce a source of error although points far from the GPS sites, i.e. where the error is greater, have a lower weight in the data integration. This error can only be reduced by considering dense GPS networks.

The quality of the GPS data interpolation is also connected to another possible disadvantage of the method. Indeed, in general, the accuracy of the three deformation components obtained by the algorithm is not the same because of the different accuracy of the data involved in the integration. Usually, the accuracy of the vertical component is larger than the horizontal one since it is mainly due to the InSAR data which are characterized by accuracies of the order of mm. Concerning the horizontal component, the NS component is constrained by both POT and MAI data apart from the GPS measurement however the accuracy is lower. The main problem could be related to the estimation of the EW component. Indeed, all the data involved in the integration provide a contribution in calculating this component but the remote sensing data, i.e. InSAR, MAI and POT, are less sensitive to the EW movements. This is due to the antenna configuration and viewing geometry then it cannot be changed. Therefore, the more reliable data in constraining the EW component are the GPS ones. For this reason, if the GPS network is not dense enough, the accuracy

of the EW component could be much lower than the other two.

In addition, the accuracies provided in previous chapter are the results of the mathematical approach however not taking into account the involved parameters and the studied phenomenon. In order to properly assess the performance of the algorithm several already known or synthetic deformation fields should be studied varying the features. This the only way to evaluate the rms between the true and the estimated displacement map.

## **5.4 FUTURE PERSPECTIVES**

The new generation of satellites allows working at different scale of observation varying the aerial coverage and the pixel resolution. Because of the large wavelength (23.6 cm), the  $\sim 10$  m resolution L-band data of ALOS are able to penetrate thick layers of vegetation thus improving the coherence of the backscattered signal.

The high resolution satellite, i.e. Cosmo-SkyMed and TerraSAR-X, provide X-band data up to  $\sim 1 \times 1$  m resolution representing an area of about 40 km. They can then be used for monitoring small scale phenomena such as a building behavior, to evaluate the effect of an earthquake, or subsidence in urban scenarios.

On the other hand, the main acquisition mode implemented by Sentinel-1 is the Interferometric Wide (IW) swath mode, a new type of ScanSAR mode designed to cover the Earth with revisit time of about 12 days. It works with three sub-swaths having a swath width of about 250 km with a pixel resolution of  $5 \times 20$  m. Then, using data with short revisit time and covering large areas, even whole countries (Sentinel-1 mapped the whole Italy), is possible monitoring tectonic movements and larger scale phenomena.

In addition, some of these new satellites like Cosmo-SkyMed and Sentinel-1 have been designed with an incidence angle which can be changed according to the investigated area and the user requirements. For example, the incidence angle of Sentinel-1 operating in Stripmap mode spans from  $\sim 18^\circ$  to  $\sim 46^\circ$ . Instead, Cosmo-SkyMed is able to acquire data with an incidence angle ranging  $25^\circ$ - $50^\circ$ . Since in InSAR analysis, higher incidence angle means increased sensitivity in any EW surface movements, this flexibility allows to better exploit the technique adjusting the parameters of data acquisition to the studied phenomenon.

Therefore, all these capabilities can be used to improve the accuracy of the measurements in InSAR, MAI and POT analysis and deeply exploit the remote sensing observation of the Earth.

On the other hand, the main problem in the integration algorithm about the GPS data is related to the interpolation step. Obviously, denser or ad-hoc networks, by installing several campaign GPS,

should significantly improve the reliability of the interpolated GPS data. In addition, other methods of data integration without GPS data interpolation [1] could be tested.

Lastly, an interesting perspectives is the possibility to make the data integration algorithm accessible to anyone, included non-expert users. Indeed, in the last years some online platform were developed to support the exploitation of satellite Earth-Observations for geohazard applications and to provide services both to expert and non-expert users. For example, the new on-line Geohazards Exploitation Platform (GEP) by the ESA (<https://geohazards-tep.eo.esa.int/#!>) allows the user to access large collections of data hosted in the ESA clusters and perform a huge number of processing by well known tolls [2][3]. The inclusion of the data integration algorithm could be useful for helping the users to improve the knowledge of the Earth's surface and mitigate the risk.

## REFERENCES

[4] Guglielmino F., Nunnari G., Puglisi G., Spata A. (2011) - Simultaneous and Integrated Strain Tensor Estimation From Geodetic and Satellite Deformation Measurements to Obtain Three-Dimensional Displacement Maps. *IEEE Transactions on Geoscience and Remote Sensing*, vol. 49, no.6, pp. 1815 – 1826, doi: 10.1109/TGRS.2010.2103078.

[4] Ferretti, A.; Prati, C.; Rocca, F. Nonlinear subsidence rate estimation using permanent scatterers in differential SAR interferometry. *IEEE Trans. Geosci. Remote Sens.* 2000, 38, 2202–2212.

[6] Berardino, P.; Fornaro, G.; Lanari, R.; Sansosti, E. A new algorithm for surface deformation monitoring based on small baseline differential SAR interferograms. *IEEE Trans. Geosci. Remote Sens.* 2002, 40, 2375–2383.

## APPENDIX A

# COMPUTER CODE

**pro** 3D MAP

```
;IMPORT THE .TIF FILES IN IDL ENVIRONMENT
;
;COHERENCE
path1='/media/marco/marco1/NAPA/Cosismico/Napa_IDL_code/Tiff_pre/Napa_Coherence.tif'
img1_pos=[0]
ENVI_OPEN_FILE, path1, R_FID=fid_img_coer, /NO_REALIZE
ENVI_FILE_QUERY, fid_img_coer, dims=dims_img, ns=ns, nl=nl, xstart=xs, ystart=ys
mapinfo_1=ENVI_GET_MAP_INFO(fid=fid_img_coer, UNDEFINED=mapok)
Coherence=envi_get_data(fid=fid_img_coer, dims=dims_img, pos=[img1_pos])
ENVI_WRITE_ENVI_FILE, Coherence, bnames=['coerenza'],map_info=infomap_img1,
    /IN_MEMORY;
;SAVE, data_coerenza, FILENAME = 'C:\AAA_INGV_CNT\data\xxx.sav'
ENVI_WRITE_ENVI_FILE, Coherence, bnames=['coerenza'],map_info=mapinfo_1,
OUT_NAME='/media/marco/marco1/NAPA/Cosismico/Napa_IDL_code/CC.tif'

;GPS_NS
path2='/media/marco/marco1/NAPA/Cosismico/Napa_IDL_code/Tiff_pre/Napa_GPS_NS.tif'
img1_pos=[0]
ENVI_OPEN_FILE, path2, R_FID=fid_img_NS_gps, /NO_REALIZE
ENVI_FILE_QUERY, fid_img_NS_gps, dims=dims_img, ns=ns, nl=nl, xstart=xs, ystart=ys
mapinfo_2=ENVI_GET_MAP_INFO(fid=fid_img_NS_gps, UNDEFINED=mapok)
GPS_NS=envi_get_data(fid=fid_img_NS_gps, dims=dims_img, pos=[img1_pos])
ENVI_WRITE_ENVI_FILE, GPS_NS, bnames=['NS_gps'],map_info=infomap_img1, /IN_MEMORY;

path8='/media/marco/marco1/NAPA/Cosismico/Napa_IDL_code/Tiff_pre/Napa_GPS_Sigma_NS.tif'
img1_pos=[0]
ENVI_OPEN_FILE, path8, R_FID=fid_img_Sigma_NS_gps, /NO_REALIZE
ENVI_FILE_QUERY, fid_img_Sigma_NS_gps, dims=dims_img, ns=ns, nl=nl, xstart=xs,
    ystart=ys
mapinfo_8=ENVI_GET_MAP_INFO(fid=fid_img_Sigma_NS_gps, UNDEFINED=mapok)
GPS_Sigma_NS=envi_get_data(fid=fid_img_Sigma_NS_gps, dims=dims_img, pos=[img1_pos])
ENVI_WRITE_ENVI_FILE, GPS_Sigma_NS, bnames=['Sigma_NS_gps'],map_info=infomap_img1,
    /IN_MEMORY;

;GPS_EW
path3='/media/marco/marco1/NAPA/Cosismico/Napa_IDL_code/Tiff_pre/Napa_GPS_EW.tif'
img1_pos=[0]
ENVI_OPEN_FILE, path3, R_FID=fid_img_ew_gps, /NO_REALIZE
ENVI_FILE_QUERY, fid_img_ew_gps, dims=dims_img, ns=ns, nl=nl, xstart=xs, ystart=ys
mapinfo_3=ENVI_GET_MAP_INFO(fid=fid_img_ew_gps, UNDEFINED=mapok)
GPS_EW=envi_get_data(fid=fid_img_ew_gps, dims=dims_img, pos=[img1_pos])
ENVI_WRITE_ENVI_FILE, GPS_EW, bnames=['NS_gps'],map_info=infomap_img1, /IN_MEMORY;

path9='/media/marco/marco1/NAPA/Cosismico/Napa_IDL_code/Tiff_pre/Napa_GPS_Sigma_EW.tif'
img1_pos=[0]
ENVI_OPEN_FILE, path9, R_FID=fid_img_Sigma_EW_gps, /NO_REALIZE
ENVI_FILE_QUERY, fid_img_Sigma_EW_gps, dims=dims_img, ns=ns, nl=nl, xstart=xs, ystart=ys
mapinfo_9=ENVI_GET_MAP_INFO(fid=fid_img_Sigma_EW_gps, UNDEFINED=mapok)
GPS_Sigma_EW=envi_get_data(fid=fid_img_Sigma_EW_gps, dims=dims_img, pos=[img1_pos])
```

```

ENVI_WRITE_ENVI_FILE, GPS_Sigma_EW, bnames=['Sigma_EW_gps'], map_info=infomap_img1,
/IN_MEMORY;

;GPS_UP
path4='/media/marco/marco1/NAPA/Cosismico/Napa_IDL_code/Tiff_pre/Napa_GPS_UP.tif'
img1_pos=[0]
ENVI_OPEN_FILE, path4, R_FID=fid_img_UP_gps, /NO_REALIZE
ENVI_FILE_QUERY, fid_img_UP_gps, dims=dims_img, ns=ns, nl=nl, xstart=xs, ystart=ys
mapinfo_4=ENVI_GET_MAP_INFO(fid=fid_img_UP_gps, UNDEFINED=mapok)
GPS_UP=envi_get_data(fid=fid_img_UP_gps, dims=dims_img, pos=[img1_pos])
ENVI_WRITE_ENVI_FILE, GPS_UP, bnames=['UP_gps'], map_info=infomap_img1, /IN_MEMORY;

path10='/media/marco/marco1/NAPA/Cosismico/Napa_IDL_code/Tiff_pre/Napa_GPS_Sigma_UP.
.tif'
img1_pos=[0]
ENVI_OPEN_FILE, path10, R_FID=fid_img_Sigma_UP_gps, /NO_REALIZE
ENVI_FILE_QUERY, fid_img_Sigma_UP_gps, dims=dims_img, ns=ns, nl=nl, xstart=xs,
ystart=ys
mapinfo_10=ENVI_GET_MAP_INFO(fid=fid_img_Sigma_UP_gps, UNDEFINED=mapok)
GPS_Sigma_UP=envi_get_data(fid=fid_img_Sigma_UP_gps, dims=dims_img, pos=[img1_pos])
ENVI_WRITE_ENVI_FILE, GPS_Sigma_UP, bnames=['Sigma_UP_gps'], map_info=infomap_img1,
/IN_MEMORY;

;InSAR
path5='/media/marco/marco1/NAPA/Cosismico/Napa_IDL_code/Tiff_pre/Napa_InSAR.tif'
img1_pos=[0]
ENVI_OPEN_FILE, path5, R_FID=fid_img_insar, /NO_REALIZE
ENVI_FILE_QUERY, fid_img_insar, dims=dims_img, ns=ns, nl=nl, xstart=xs, ystart=ys
mapinfo_5=ENVI_GET_MAP_INFO(fid=fid_img_insar, UNDEFINED=mapok)
D_InSAR_LOS=envi_get_data(fid=fid_img_insar, dims=dims_img, pos=[img1_pos])
ENVI_WRITE_ENVI_FILE, D_InSAR_LOS, bnames=['InSAR'], map_info=infomap_img1,
/IN_MEMORY;
;SAVE, data_coerenza, FILENAME = 'C:\AAA_INGV_CNT\data\xxx.sav'

;MAI
path6='/media/marco/marco1/NAPA/Cosismico/Napa_IDL_code/Tiff_pre/Napa_MAI.tif'
img1_pos=[0]
ENVI_OPEN_FILE, path6, R_FID=fid_img_mai1, /NO_REALIZE
ENVI_FILE_QUERY, fid_img_mai1, dims=dims_img, ns=ns, nl=nl, xstart=xs, ystart=ys
mapinfo_6=ENVI_GET_MAP_INFO(fid=fid_img_mai1, UNDEFINED=mapok)
MAI_AZ=envi_get_data(fid=fid_img_mai1, dims=dims_img, pos=[img1_pos])
ENVI_WRITE_ENVI_FILE, MAI_AZ, bnames=['MAI_AZ'], map_info=infomap_img1, /IN_MEMORY;
;SAVE, data_coerenza, FILENAME = 'C:\AAA_INGV_CNT\data\xxx.sav'

;POT
path7='/media/marco/marco1/NAPA/Cosismico/Napa_IDL_code/Tiff_pre/NAPA_POT.tif'
img1_pos=[0]
ENVI_OPEN_FILE, path7, R_FID=fid_img_pot1, /NO_REALIZE
ENVI_FILE_QUERY, fid_img_pot1, dims=dims_img, ns=ns, nl=nl, xstart=xs, ystart=ys
mapinfo_7=ENVI_GET_MAP_INFO(fid=fid_img_pot1, UNDEFINED=mapok)
POT_AZ=envi_get_data(fid=fid_img_pot1, dims=dims_img, pos=[img1_pos])
ENVI_WRITE_ENVI_FILE, POT_AZ, bnames=['POT_AZ'], map_info=infomap_img1, /IN_MEMORY;
;SAVE, data_coerenza, FILENAME = 'C:\AAA_INGV_CNT\data\xxx.sav'

;REDEFINING NAN
for i=0, 1815 do begin
for j=0, 1168 do begin
if (D_InSAR_LOS(i,j) EQ 0.) then begin
print, 'Reina'
D_InSAR_LOS(i,j)=!VALUES.F_NAN
endif else begin
D_InSAR_LOS(i,j)=D_InSAR_LOS(i,j)

```

```

        print, 'Hysaj'
    endelse
endfor
endifor

for i=0, 1815 do begin
    for j=0, 1168 do begin
        if (MAI_AZ(i,j) EQ 0.) then begin
            print, 'Albiol'
            MAI_AZ(i,j)=!VALUES.F_NAN
        endif else begin
            MAI_AZ(i,j)=MAI_AZ(i,j)
            print, 'Koulibaly'
        endelse
    endfor
endfor

for i=0, 1815 do begin
    for j=0, 1168 do begin
        if (POT_AZ(i,j) EQ 0.) then begin
            print, 'Ghoulam'
            POT_AZ(i,j)=!VALUES.F_NAN
        endif else begin
            POT_AZ(i,j)=POT_AZ(i,j)
            print, 'Allan'
        endelse
    endfor
endfor

for i=0, 1815 do begin
    for j=0, 1168 do begin
        if (GPS_NS(i,j) LT -1e+15) then begin
            print, 'Jorginho'
            GPS_NS(i,j)=!values.f_nan
        endif else begin
            GPS_NS(i,j)=GPS_NS(i,j)
            print, 'Hamsik'
        endelse
    endfor
endfor

for i=0, 1815 do begin
    for j=0, 1168 do begin
        if (GPS_UP(i,j) LT -1e+15) then begin
            print, 'Callejon'
            GPS_UP(i,j)=!values.f_nan
        endif else begin
            GPS_UP(i,j)=GPS_UP(i,j)
            print, 'Higuain'
        endelse
    endfor
endfor

for i=0, 1815 do begin
    for j=0, 1168 do begin
        if (GPS_EW(i,j) LT -1e+15) then begin
            print, 'Insigne'
            GPS_EW(i,j)=!values.f_nan
        endif else begin

```

```

        GPS_EW(i,j)=GPS_EW(i,j)
        print, 'Gabbiadini'
    endwhile
endfor
endifor
endifor

```

```

for i=0, 1815 do begin
    for j=0, 1168 do begin
        if (GPS_Sigma_NS(i,j) LT -1e+15) then begin
            print, 'Mertens'
            GPS_Sigma_NS(i,j)!=values.f_nan
        endif else begin
            GPS_Sigma_NS(i,j)=GPS_Sigma_NS(i,j)
            print, 'Lopez'
        endwhile
    endfor
endfor
endifor

```

```

for i=0, 1815 do begin
    for j=0, 1168 do begin
        if (GPS_Sigma_EW(i,j) LT -1e+15) then begin
            print, 'Chiriches'
            GPS_Sigma_EW(i,j)!=values.f_nan
        endif else begin
            GPS_Sigma_EW(i,j)=GPS_Sigma_EW(i,j)
            print, 'Valdifiori'
        endwhile
    endfor
endfor
endifor

```

```

for i=0, 1815 do begin
    for j=0, 1168 do begin
        if (GPS_Sigma_UP(i,j) LT -1e+15) then begin
            print, 'Strinic'
            GPS_Sigma_UP(i,j)!=values.f_nan
        endif else begin
            GPS_Sigma_UP(i,j)=GPS_Sigma_UP(i,j)
            print, 'Maggio'
        endwhile
    endfor
endfor
endifor

```

```

;SET MAI AND POT OUTPUTS AS -1*MEASURED DISPLACEMENT SINCE ALONG DESCENDING ORBIT
THE MOVEMENT IS CONSIDERED POSITIVE SOUTHWARD (I.E. IN THE SAME DIRECTION OF THE
SATELLITE FLIGHT)

```

```

D_MAI_AZ=-1*MAI_AZ
D_POT_AZ=-1*POT_AZ

```

```

;SET SIGMA_GPS AS SIGMA_INTERPOLATION + MEAN SIGMA MEASURED AND THEN CONVERT IN
METERS

```

```

Sigma_GPS_NS=((GPS_Sigma_NS+1.3351807229)/1000)
Sigma_GPS_EW=((GPS_Sigma_EW+1.180753012)/1000)
Sigma_GPS_UP=((GPS_Sigma_UP+4.2909717868)/1000)

```

```

;CONVERT IN METERS THE DISPLACEMENT MEASURED BY GPS

```

```

D_GPS_NS=GPS_NS/1000
D_GPS_EW=GPS_EW/1000
D_GPS_UP=GPS_UP/1000

```

```

;SATELLITE AND PROCESSING PARAMETERS
cos_alpha=-0.97334353835
sen_alpha=-0.22935203583
cos_teta=0.91922057496
sen_teta=0.39374298033

NL=225 ;Numero di Looks
n=0.5 ;Normalized Squint
l=12.3 ;Antenna azimuth lenght
lambda=0.05550415767 ;wavelenght

;INITIALIZE THE MATRICES
Sigma_MAI=fltarr(1816,1169)
Sigma_POT=fltarr(1816,1169)
Sigma_InSAR=fltarr(1816,1169)

d_EW=fltarr(1816,1169)
d_NS=fltarr(1816,1169)
d_UP=fltarr(1816,1169)

A=fltarr(1816,1169)
B=fltarr(1816,1169)
C=fltarr(1816,1169)
D=fltarr(1816,1169)
E=fltarr(1816,1169)
F=fltarr(1816,1169)
G=fltarr(1816,1169)
H=fltarr(1816,1169)
P=fltarr(1816,1169)
M=fltarr(1816,1169)
;prova=make_array(1816,1169, value=!Values.F_NAN )

;ESTIMATION OF THE 3D OPTIMIZED DISPLACEMENT COMPONENTS

;SIGMA
for i=0, 1815 do begin
  for j=0, 1168 do begin
    Sigma_MAI(i,j)=((1/(4.*!pi*n))*(1./sqrt(NL)))*(sqrt(1.-
    Coherence(i,j))^2/Coherence(i,j)))
    Sigma_POT(i,j)=((1/2.)*(sqrt(3./10.*NL)))*(sqrt(2.+(5.*(Coherence(i,j)^2))-
    (7.*(Coherence(i,j)^4)))/!pi*(Coherence(i,j)^2)))
    Sigma_InSAR(i,j)=(((lambda/(4.*!pi))*(1./sqrt(2.*NL)))*(sqrt(1.-
    (Coherence(i,j))^2/Coherence(i,j))))

;SUPPORT VARIABLES
A(i,j)=(((1./Sigma_InSAR(i,j)^2)*cos_alpha^2*cos_teta^2)+((1./
(Sigma_MAI(i,j))^2)*sen_alpha^2)+
((1./Sigma_POT(i,j)^2)*sen_alpha^2)+(1./Sigma_GPS_EW(i,j)^2))
B(i,j)=(1./Sigma_InSAR(i,j)^2*cos_alpha*cos_teta*sen_teta)
C(i,j)=((1./Sigma_MAI(i,j)^2)*cos_alpha*sen_alpha+
((1./Sigma_POT(i,j)^2)*cos_alpha*sen_alpha))
D(i,j)=(((1./Sigma_InSAR(i,j)^2)*D_InSAR_LOS(i,j)*cos_alpha*sen_teta)+
((1./Sigma_MAI(i,j)^2)*MAI_AZ(i,j)*sen_alpha)+
((1./Sigma_POT(i,j)^2)*POT_AZ(i,j)*sen_alpha)+
((1./Sigma_GPS_EW(i,j)^2)*D_GPS_EW(i,j)))
E(i,j)=(((1./Sigma_MAI(i,j)^2)*cos_alpha^2)+
((1./Sigma_POT(i,j)^2)*cos_alpha^2)+(1./Sigma_GPS_NS(i,j)^2))
F(i,j)=(((1./Sigma_MAI(i,j)^2)*sen_alpha*cos_alpha)-
((1./Sigma_POT(i,j)^2)*sen_alpha*cos_alpha))
G(i,j)=(((1./Sigma_MAI(i,j)^2)*MAI_AZ(i,j)*cos_alpha)+
((1./Sigma_POT(i,j)^2)*POT_AZ(i,j)*cos_alpha)+
((1./Sigma_GPS_NS(i,j)^2)*D_GPS_NS(i,j)))

```

```

H(i,j)=(((1./Sigma_InSAR(i,j)^2)*cos_teta^2)+(1./Sigma_GPS_UP(i,j)^2))
P(i,j)=((1./Sigma_InSAR(i,j)^2)*cos_alpha*sen_teta*cos_teta)
M(i,j)=(((1./Sigma_InSAR(i,j)^2)*D_InSAR_LOS(i,j)*cos_teta)+
((1./Sigma_GPS_UP(i,j)^2)*D_GPS_UP(i,j)))

;3D COMPONENTS
d_EW(i,j)=(((B(i,j)/A(i,j))*(M(i,j)/H(i,j)))-((C(i,j)/A(i,j))*(G(i,j)/E(i,j))))
+(D(i,j)/A(i,j)))/(1+((B(i,j)/A(i,j))*(P(i,j)/H(i,j))))+
((C(i,j)/A(i,j))*(F(i,j)/E(i,j))))
d_NS(i,j)=((F(i,j)/E(i,j))*d_EW(i,j))+G(i,j)/E(i,j)
d_UP(i,j)=(((P(i,j))/H(i,j))*d_EW(i,j))+M(i,j)/H(i,j))

endfor
endfor

;RIDEFINING NAN IN SIGMA MAPS
for i=0, 1815 do begin
for j=0, 1168 do begin
if (Sigma_MAI(i,j) LT -1e+15) then begin
print, 'Un'
Sigma_MAI(i,j)=!values.f_nan
endif else begin
Sigma_MAI(i,j)=Sigma_MAI(i,j)
print, 'giorno'
endelse
endfor
endfor

for i=0, 1815 do begin
for j=0, 1168 do begin
if (Sigma_MAI(i,j) GT 1e+15) then begin
print, 'all'
Sigma_MAI(i,j)=!values.f_nan
endif else begin
Sigma_MAI(i,j)=Sigma_MAI(i,j)
print, 'improvviso'
endelse
endfor
endfor

for i=0, 1815 do begin
for j=0, 1168 do begin
if (Sigma_InSAR(i,j) LT -1e+15) then begin
print, 'mi'
Sigma_InSAR(i,j)=!values.f_nan
endif else begin
Sigma_InSAR(i,j)=Sigma_InSAR(i,j)
print, 'innamorai'
endelse
endfor
endfor

for i=0, 1815 do begin
for j=0, 1168 do begin
if (Sigma_InSAR(i,j) GT 1e+15) then begin
print, 'di'
Sigma_InSAR(i,j)=!values.f_nan
endif else begin
Sigma_InSAR(i,j)=Sigma_InSAR(i,j)
print, 'te'
endelse
endfor
endfor
endfor

```

```

for i=0, 1815 do begin
  for j=0, 1168 do begin
    if (Sigma_POT(i,j) LT -1e+15) then begin
      print, 'Alè'
      Sigma_POT(i,j)=!values.f_nan
    endif else begin
      Sigma_POT(i,j)=Sigma_POT(i,j)
      print, 'Alè'
    endelse
  endfor
endfor

for i=0, 1815 do begin
  for j=0, 1168 do begin
    if (Sigma_POT(i,j) GT 1e+15) then begin
      print, 'Alè'
      Sigma_POT(i,j)=!values.f_nan
    endif else begin
      Sigma_POT(i,j)=Sigma_POT(i,j)
      print, 'Alè'
    endelse
  endfor
endfor

;H=(Sigma_POT+Sigma_GPS_NS)/2
;F=(Sigma_MAI+Sigma_GPS_EW+Sigma_InSAR+Sigma_POT)/3.5

;EXPORT TO .TIF FORMAT
ENVI_WRITE_ENVI_FILE, Sigma_GPS_EW, BNames=['PROVA'],MAP_INFO=MAPINFO_1,
OUT_NAME='/media/marco/marco1/NAPA/Cosismico/Napa_IDL_code/Output/SIGMA_GPS_EW.tif'

ENVI_WRITE_ENVI_FILE, Sigma_GPS_UP, BNames=['PROVA'],MAP_INFO=MAPINFO_1,
OUT_NAME='/media/marco/marco1/NAPA/Cosismico/Napa_IDL_code/Output/SIGMA_GPS_UP.tif'

ENVI_WRITE_ENVI_FILE, Sigma_GPS_NS, bnames=['prova'],map_info=mapinfo_1,
OUT_NAME='/media/marco/marco1/NAPA/Cosismico/Napa_IDL_code/Output/SIGMA_GPS_NS.tif'

ENVI_WRITE_ENVI_FILE, D_MAI_AZ, bnames=['prova'],map_info=mapinfo_1,
OUT_NAME='/media/marco/marco1/NAPA/Cosismico/Napa_IDL_code/Output/MAI_AZ.tif'

ENVI_WRITE_ENVI_FILE, D_InSAR_LOS, bnames=['prova'],map_info=mapinfo_1,
OUT_NAME='/media/marco/marco1/NAPA/Cosismico/Napa_IDL_code/Output/InSAR_LOS.tif'

ENVI_WRITE_ENVI_FILE, D_POT_AZ, bnames=['prova'],map_info=mapinfo_1,
OUT_NAME='/media/marco/marco1/NAPA/Cosismico/Napa_IDL_code/Output/POT_AZ.tif'

ENVI_WRITE_ENVI_FILE, Sigma_MAI, bnames=['prova'],map_info=mapinfo_1,
OUT_NAME='/media/marco/marco1/NAPA/Cosismico/Napa_IDL_code/Output/SIGMA_MAI.tif'

ENVI_WRITE_ENVI_FILE, Sigma_InSAR, bnames=['prova'],map_info=mapinfo_1,
OUT_NAME='/media/marco/marco1/NAPA/Cosismico/Napa_IDL_code/Output/SIGMA_InSAR.tif'

ENVI_WRITE_ENVI_FILE, Sigma_POT, bnames=['prova'],map_info=mapinfo_1,
OUT_NAME='/media/marco/marco1/NAPA/Cosismico/Napa_IDL_code/Output/SIGMA_POT.tif'

ENVI_WRITE_ENVI_FILE, H, bnames=['prova'],map_info=mapinfo_1,
OUT_NAME='/media/marco/marco1/NAPA/Cosismico/Napa_IDL_code/Output/SIGMA_NS.tif'

ENVI_WRITE_ENVI_FILE, F, bnames=['prova'],map_info=mapinfo_1,
OUT_NAME='/media/marco/marco1/NAPA/Cosismico/Napa_IDL_code/Output/SIGMA_EW.tif'

;EXPORT ALSO THE 3D OPTIMIZED COMPONENTS IN .TIF FORMAT
ENVI_WRITE_ENVI_FILE, d_EW, bnames=['d_EW'],map_info=mapinfo_1,
OUT_NAME='/media/marco/marco1/NAPA/Cosismico/Napa_IDL_code/Output/d_EW.tif'

```

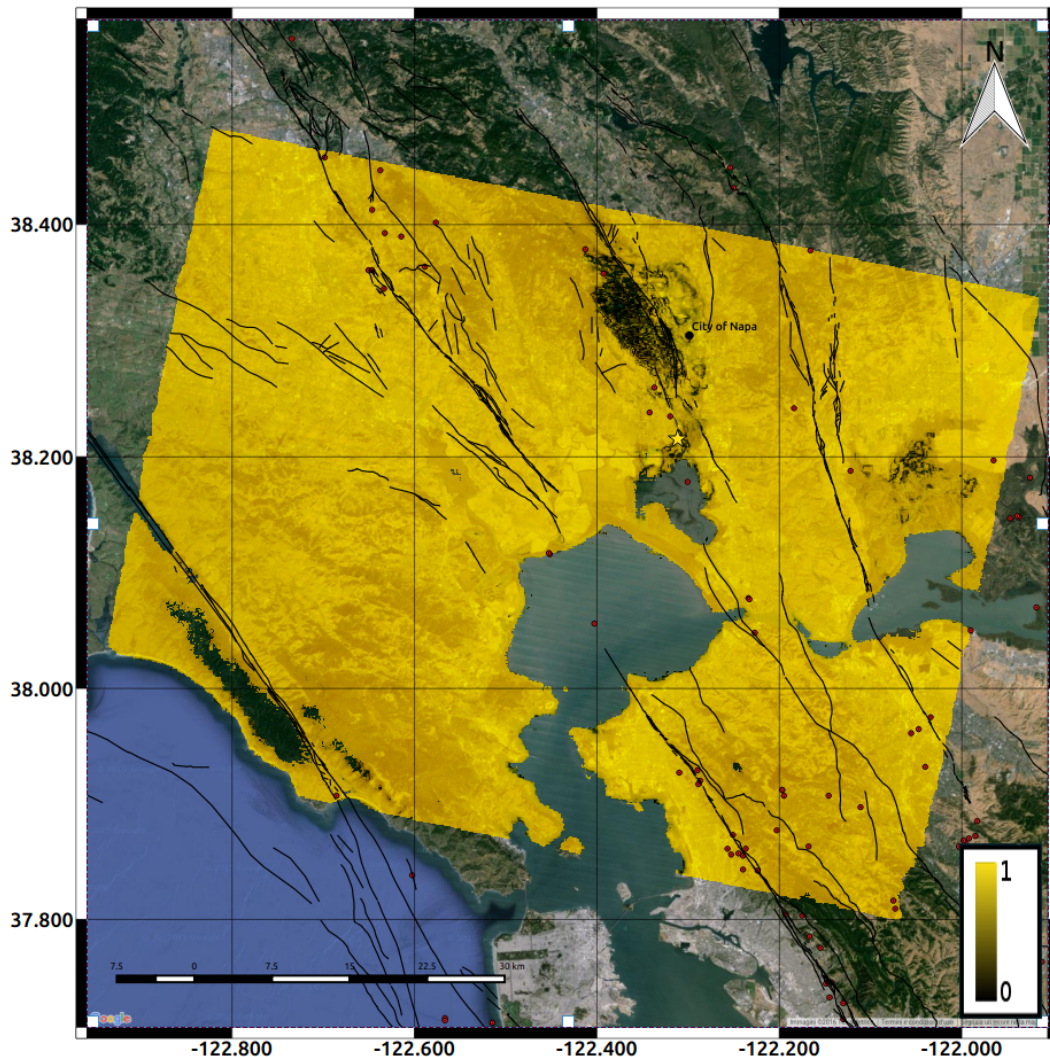
```
ENVI_WRITE_ENVI_FILE, d_NS, bnames=['d_NS'],map_info=mapinfo_1,  
OUT_NAME='/media/marco/marco1/NAPA/Cosismico/Napa_IDL_code/Output/d_NS.tif'
```

```
ENVI_WRITE_ENVI_FILE, d_UP, bnames=['d_UP'],map_info=mapinfo_1,  
OUT_NAME='/media/marco/marco1/NAPA/Cosismico/Napa_IDL_code/Output/d_UP.tif'
```

**stop**

**end**

## NAPA COHERENCE MAP



The coherence map of the area surrounding the city of Napa shows a very high coherence ranging from 0.8 and 1. This is mainly due to the short temporal interval between the two SAR acquisitions. In addition, in general, in the vegetated areas, the coherence is higher during the dry periods. This area is located in the central valley of California, bounded by the Sierra Nevada (east) and the coastal mountains (west), where the climatic conditions are very favorable. Indeed, during the summer season, the rains are extremely rare and the medium temperature is about 20°-22°. Then, the high coherence is explained since the time of occurrence of the earthquake and subsequently of the SAR images is the month of August.

The only area where the coherence is not so high is close the epicentral area, westward the city of Napa most likely because of the saturation effect induced by the strong deformation observed.

# COPYRIGHT RELEASES

## Geophysical Research Letters



MEMBER LOGIN    DONATE  
SEARCH PUBS    JOIN / RENEW  
Google™ Custom Search    **SEARCH**

- About
- Membership
- Leadership
- Publications
- Meetings
- Data Services
- Careers
- Honors
- Science Policy
- Education
- Newsroom

[Home](#) / [Author Resources](#) / [Usage Permissions](#)

### USAGE PERMISSIONS

AGU grants permission for individuals to use figures, tables, and short quotes from AGU journal and books for republication in academic works and to make single copies for personal use in research, study, or teaching provided full attribution is included. There is no need to request this permission from AGU.

This permission does not extend to public posting of the PDF or HTML created by AGU for publication. AGU journal content after 1996 is now freely available 24 months after publication; AGU encourages linking to this content directly. There is no charge or additional permissions needed for any of these uses, but the material must be cited appropriately.

For information on requesting permission for commercial reuse of AGU content, please click on the "permissions" link on any journal or book home page in the **Wiley Online Library**.

#### RIGHTS GRANTED TO AUTHORS

AGU's philosophy recognizes the need to ensure that authors have a say in how their works are used and the necessity to foster broad dissemination of scientific literature while protecting the viability of the publication system. The following nonexclusive rights are granted to AGU authors:

- All proprietary rights other than copyright (such as patent rights)
- The right to present the material orally
- The right to reproduce figures, tables, and extracts properly cited
- The right to make paper copies of all or part of the contribution for classroom use
- The right to deny subsequent commercial use of the contribution
- The right to place the contribution or its abstract on his/her personal Web site as described below.

#### Publications    Resources

- Journals
- Books
- Eos
- Journal Editors
- Submit a Paper
- Author Resources
- Reviewer Resources
- Usage Permissions
- Publications Statistics
- Kaula Award
- Publication Policies
- Editor Searches

#### PUBLICATIONS CONTACTS

##### Brooks Hanson

Director of Publications

##### Mary Warner

Assistant Director, Editorial Management

##### Jeanette Panning

Assistant Director, Publications Programs

##### Submission questions

##### Production questions

##### General questions

## IEEE Journal of Selected Topics in Applied Earth Observations and Remote Sensing

From: **Jocelyn Chanussot** <jocelyn.chanussot@gipsa-lab.grenoble-inp.fr>

Date: 2016-01-12 18:19 GMT+01:00

Subject: Re: Permission of reprint

To: Marco Polcari <marco.polcari@ingv.it>

Dear Marco,

sure, no problem, this is a common practise.

please simply clearly add the reference of the paper each time you are using a published material.

best of luck with the completion of your PhD,

jocelyn chanussot

---

Jocelyn Chanussot  
Professor, Signal and Image Processing  
Editor-in-Chief IEEE Journal of Selected Topics in Applied Earth Observations  
and Remote Sensing (<http://www.grss-ieee.org/publications/jstars/>)

Visit my homepage !  
<http://jocelyn-chanussot.net>

ENSE3 - <http://ense3.grenoble-inp.fr/>  
Grenoble Institute of Technology (<http://www.grenoble-inp.fr/>)  
Grenoble Images sPeech Signals and Automatics Lab (GIPSA-Lab <http://www.gipsa-lab.inpg.fr/>)

E-mail: [jocelyn.chanussot@gipsa-lab.grenoble-inp.fr](mailto:jocelyn.chanussot@gipsa-lab.grenoble-inp.fr)

Surface mail:  
GIPSA-Lab, DIS / ENSE3, site Ampere  
Domaine universitaire  
11 rue des Mathematiques  
BP 46 - 38402 Saint Martin d Heres cedex

phone (office) : [+33 \(0\) 4 76 82 62 73](tel:+330476826273)  
phone (mobile): [+33 \(0\) 6 62 73 84 44](tel:+330662738444)  
Fax (office): [+33 \(0\) 4 76 82 63 84](tel:+330476826384)

## Remote Sensing Journal

From: **Elvis Wang** <elvis.wang@mdpi.com>  
Date: 2016-01-13 10:00 GMT+01:00  
Subject: Re: Fwd: Permission of reprint  
To: marco.polcari@ingv.it  
Cc: Prasad S Thenkabail <thenkabail@gmail.com>, Remote Sensing Editorial Office <remotesensing@mdpi.com>

Dear Mr. Polcari,

Thank you for your email. As it is published in open access format, you are copyright holder and therefore free to reuse it, with proper acknowledgment of the source. If you need further assistance, please feel free to let us know.

Wish you a successful defense!

Kind regards,  
Elvis Wang  
Managing Editor  
Infrastructures (<http://www.mdpi.com/journal/i>)  
Land (<http://www.mdpi.com/journal/l>)  
Remote Sensing (<http://www.mdpi.com/journal/r>)

Follow /Remote Sensing/ at  
LinkedIn: <https://ch.linkedin.com/in/rem>  
Twitter: <https://twitter.com/RemoteSens>

Follow /Land/ at  
LinkedIn: <https://ch.linkedin.com/in/lan>  
Twitter: [https://twitter.com/Land\\_MDPI](https://twitter.com/Land_MDPI)

/Remote Sensing/ Impact Factor (2014), 3.180.

--

Mr. Elvis Wang  
MDPI Branch Office, Beijing  
Room 2207, Jincheng Center  
No. 21 Cuijingbeili  
Tongzhou District, Beijing, China  
E-Mail: [elvis.wang@mdpi.com](mailto:elvis.wang@mdpi.com)  
Tel./Fax: [+86 10 8152 1170](tel:+861081521170)

MDPI AG  
Klybeckstrasse 64, CH-4057 Basel, Switzerland  
Tel. [+41 61 683 77 34](tel:+41616837734); Fax [+41 61 302 89 18](tel:+41613028918)  
<http://www.mdpi.com/>

## European Journal of Remote Sensing

From: **Davide Travaglini** <aitjournal.editorialoffice@gmail.com>  
Date: 2016-03-25 9:22 GMT+01:00  
Subject: R: Permission of reprint  
To: Marco Polcari <marco.polcari@ingv.it>

Gentile Dott. Marco Polcari,

con la presente si acconsente all'utilizzo del testo e delle figure del seguente articolo pubblicato sulla rivista European Journal of Remote Sensing per la sua tesi di dottorato:

Title: 3D displacement field retrieved by integrating Sentinel-1 InSAR and GPS data: the 2014 South Napa earthquak

Authors: Marco Polcari, Mimmo Palano, José Fernández, Sergey V. Samsonov, Salvatore Stramondo and Susanna Zerbini

Cordiali saluti,

Davide Travaglini

---

Managing Editor  
EuJRS - European Journal of Remote Sensing  
Phone. [+39 055 2755656](tel:+390552755656)  
Fax [+39 055 319179](tel:+39055319179)  
E-mail [aitjournal.editorialoffice@](mailto:aitjournal.editorialoffice@)  
Web <http://www.aitjournal.com>

# ACKNOWLEDGMENTS

Thanks to prof. Salvatore Stramondo for believing in me and giving me the opportunity to work in a stimulating work environment.

Thanks to prof.ssa Susanna Zerbini for the important comments to my work.

Thanks to prof. José Fernandez for hosting me at IGEO in Madrid and giving me the opportunity to investigate new topics.

Thanks to Mimmo Palano and Sergey Samsonov for their patience and the useful suggestions.

Thanks to my research group at INGV, Antonio, Christian, Marco M., Matteo, Vito for their support day by day.

Thanks to Francesca, my wonderful colleague, since a trip is less complicated if you do it laughing.

Thanks to Andreas and Marianne for the good times together. I hope it was just the beginning!

Simply thanks to my wonderful parents and my sister, because it is thanks to them that I am as I am.

Special thanks to Luigi and Daniela, long live the newlyweds!. My living proof that love exists!

Thanks to the friends of a life, in alphabetical order: Andrea C., Andrea P., Fulvio, Gabriele, Gianpaolo, Michele, Paolo, Pietro, Sabrina, Simona, Valentina, Vincenzo, Vittorio. Despite the years pass and the lives take different paths there are things that remain the same forever!

Thanks to Sarri, Higuain e Koulibaly for the wonderful sundays together. With the hope of not being satisfied!

I don't want to forget anyone so thanks to all the people I met in Rome in these beautiful three years.

A final special thanks to all the people who have been or are important in my life but do not know it!